Grain Boundary Field Projection Method and Atomic Lattice Interferometer for Nanometrology

By

Chien-Kai Wang

B. Sc., National Taiwan University, 2003

M. Sc., National Taiwan University, 2005

M. Sc., Brown University, 2011

Thesis

Submitted in partial fulfillment of the requirements for the Degree of

Doctor of Philosophy in the School of Engineering at Brown University

PROVIDENCE, RHODE ISLAND

MAY 2014

This dissertation by Chien-Kai Wang is accepted in its present form

by the School of Engineering as satisfying the

dissertation requirements for the degree of Doctor of Philosophy

Date _____ _____

Kyung-Suk Kim, Advisor

Recommended to the Graduate Council

Date _____ _____

Huajian Gao, Reader

Date _____ _____

Sharvan Kumar, Reader

Approved by the Graduate Council

Date _____ _____

Peter M. Weber, Dean of the Graduate School

Curriculum Vitae

Chien-Kai Wang was born on November 19, 1980, in Taipei, Taiwan. He attended National Taiwan University, where he received his B. Sc. and M. Sc. degrees in Civil Engineering in June, 2003 and 2005 respectively. Later he entered the Solid Mechanics program at Brown University in September, 2008. He was awarded the M. Sc. degree in Applied Mathematics in May, 2011.

Publications

Jang, B.K., Kim, J.-H., Lee, H.-J., Kim, K.-S. & Wang, C.-K. System and Method for Measuring Distribution of Deformation using Atomic Force. United States Patent (submitted).

Wang, C.-K. & Kim, K.-S. (2014). Nonlinear Field Projection Method in Nanoscale Structures and Materials. U. S. National Congress on Theoretical and Applied Mechanics.

Kim, K.-S., Wang, C.-K., Cha, M.-H. & Chew, H.B. (2012). Continuum Description of Atomistics for Nanomechanics of Grain Boundary Embrittlement in FCC Metals. American Physical Society March meeting.

Wang, C.-K., Chew, H.B. & Kim, K.-S. (2011). Nanometer Scale Mechanical Behavior of Grain Boundaries. Mater. Res. Soc. Symp. Proc., 1297, 1-9.

Acknowledgments

First of all, I gratefully appreciate my advisor, Professor Kyung-Suk Kim, for his thorough supports on research of my thesis. Professor Kim's research spirit deeply influences me. During the research journey, Professor Kim always encourages me to enjoy the processes of chasing truth in science. The most invaluable point is that I learned Professor Kim's attitude of doing research in completely unexplored territories and way of handling unexpected research difficulties. In such research life, I transformed myself from being conservative to focusing on pursuing research results and then realizing the underlying meanings without fear. I have deep gratitude for dissertation committee, Professor Sharvan Kumar and Professor Huajian Gao for reading my thesis and making a number of helpful suggestions and comments for my research. These insights encouraged me to make several improvements in my thesis. In my thesis, a huge part of my research work was in collaboration with research scientists at Korea Institute of Machinery & Materials (KIMM). I wish to thank Dr. Jae-Hyun Kim and Bongkyun Jang for their kindly helps and discussions. I also wish to acknowledge the generous funding supports from KIMM and the Material Research Science & Engineering Center (MRSEC) at Brown University.

In addition to research, I have many thanks to all the Professors of School of Engineering and Division of Applied Mathematics for providing such comprehensive courses, making me honorable to do graduate studies in Solid Mechanics Program at

Brown. I would like to thank the former and current members of Nano and Micromechanics Laboratory. Professor Shuman Xia and Professor Qunyang Li encouraged me not to be afraid of expressing opinions. Professor Huck Beng Chew offered me many useful suggestions on technique development. I appreciate Dr. Sang-Pil Kim, Dr. Jin-Woo Yi, Professor Hyun-Gyu Kim and Professor Sangjin Ryu for their kindly suggestions. I deeply express my thanks to Dr. Mazen Diab, Dr. Moon-Hyun Cha and Jahn Torres for their encouragement and warm supports in the daily life at lab. I also thank my peer students, Xin Yi, Teng Zhang, Anton Tokranov, Ravi Kumar, Jay Sheth, Maria Stournara, Cheng Zhang, Yu Liu and Ruike Zhao for their assistance. Moreover, I would like to thank my friends in Brown Taiwanese Graduate Student Association for the precious friendship and making my life at Brown warm and pleasant.

I am taking this special opportunity to appreciate my families for their thoughtful supports and concerns. Finally, I sincerely express my gratitude to the most important person for me - my wife, Dr. Hsiao-Mei Wu for her accompanying, great help and considerate caring in every aspect all the time.

Table of Contents

List of Figures

Chapter 1. Introduction

1.1 Background and overview of nanocrystalline material strength

The aim of this thesis is to investigate why grain boundary strength and separation mechanisms are important for understanding high strength and certain ductility of nanocrystalline materials. Typically, conventional crystalline materials display increased strength with decreased grain sizes. Such material strengthening by decreasing their grain sizes has been well known as the Hall-Petch strengthening (Hall, 1951; Petch, 1953). This Hall-Petch relationship is usually explained that grain boundary acts as impedance of dislocation movement, and therefore yield strength is increased for materials with high volume fraction of grain boundaries. However, for materials with grain sizes less than 100 nanometers, the raised material strength could not be predicted through extrapolations of the Hall-Petch relationship (Weertman *et al*., 1999).

To explore why the Hall-Petch relationship breaks down for the ultra-fined granular materials, several studies have been made in the past decades. An experimental study on strength of granular materials with grain sizes of 8 to 16 nanometers was carried out with material hardness tests (Chokshi *et al*., 1989). The study reported that the material hardness decreased with decreased grain sizes for the ultra-fined grained copper and palladium at ambient temperature. Computer simulation for deformation in

crystalline copper of grain sizes between few nanometers to ten nanometers also showed this softening mechanism with decreased grain sizes and so called as a reverse Hall-Petch effect (Schiøtz *et al.*, 1998). In this material simulation, an enormous amount of minute sliding or atomic rearrangement events were observed only near grain boundaries, resulting in most of plastic deformation. On the contrary, dislocation activities within such small grains caused only a slight portion of the plastic deformation. Moreover, deformation evolution in nano-grained nickel with grain size of 30 nanometers in average was also experimentally observed, and the accompanied mechanisms including fundamental modes of dislocation source formation and grain failure were systematically analyzed based on the observations (Kumar *et al.*, 2003[a]; Kumar *et al.*, 2003[b]). The analysis showed that most of the deformation activities were dislocation emissions at grain boundaries along with intra-granular slips resulting in non-uniform grain-boundary sliding in the early stage of deformation. Such grain boundary sliding then produced voids at grain boundaries and triple junctions. Consequently, these voids acted as seeds for generating void-coalescence fracture processes.

One may further examine how fracture energies of grain boundaries relate to strength of materials. Beltz and Rice showed that the fracture toughness of materials is dominated by competition between cleavage decohesion and dislocation emission (Beltz & Rice, 1991). When the energy release rate for emission of a single dislocation on a particular slip plane from a crack tip is less than the energy release rate for cleavage, a dislocation moves away from the crack tip and then blunts the crack tip to be shielded from cleavage (Li & Kim, 2009; Cheng *et al.*, 2010).

Therefore, there is fairly general agreement that strength of nanocrystalline materials depends on multiple cooperative separation processes (Rice & Wang, 1989; Van Swygenhoven *et al.*, 2002; Kumar *et al.*, 2003a; Kumar *et al.*, 2003b; Chen *et al.*, 2010; Cheng *et al.*, 2010). During the multiple cooperative separation processes, however, how grain boundary structures such as misorientations between adjacent grains and interfacial impurities play roles on the strength of nano-grained materials is still an unanswered question.

1.2 Cooperative failure processes of grain boundaries

Over the past few decades, experimental and computational studies have proposed insights of cooperative failure processes of grain boundaries in such ultra-fine granular materials of grain size about few tens of nanometers. Through transmission electron microscopy (TEM) imaging and molecular dynamics (MD) simulations, small number dislocation emissions were observed at a portion of grain boundaries during plastic deformation (Schiøtz *et al.*, 1998; Kumar *et al.*, 2003[a]). On the other hand, the other portion of grain boundaries separated to a certain level instead of emitting dislocation. Based on these two distinct kinds of grain boundary deformation, here we contribute a new model to elucidate failure mechanisms for nanocrystalline materials about high strength and certain ductility.

In this model depicted in Figure 1.1, grain boundaries fall into two groups: tough and weak boundaries. The “tough boundary” group is defined as the grain boundaries of particular misorientations or impurities intrinsically having dislocation emission, which

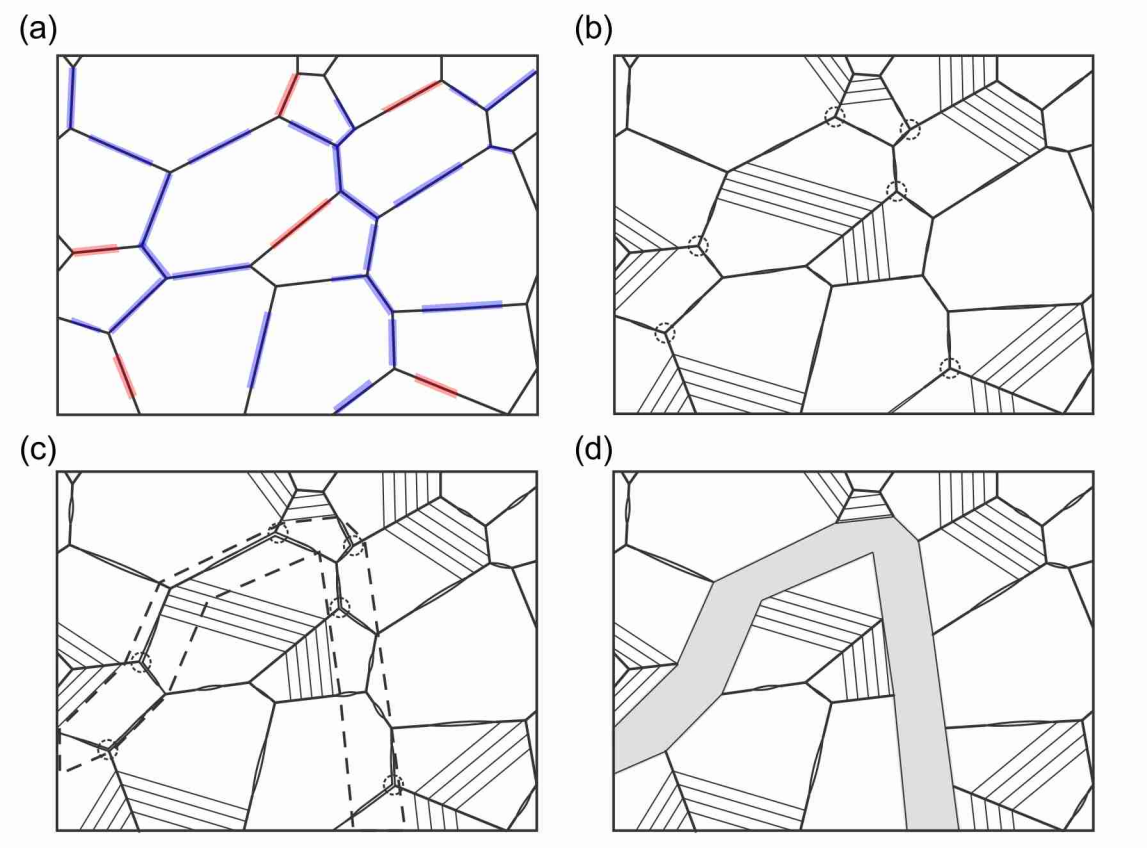

Figure 1.1 Failure mechanisms of nanocrystalline materials with ultra-fine grains. (a) Intrinsically weak (brittle, colored in blue) and strong (tough, colored in red) grain boundaries. (b) At early stages of loading, the intrinsically weak grain boundaries open elastically, while strong grain boundaries emit dislocations. (c) As loading increases, grain boundary incompatibilities between the strong and weak boundaries cause stress concentration at triple junctions of grain boundaries. (d) At a later stage of loading, void coalescence and loss of triaxiality develop in materials by forming nanowhiskers.

causes grain boundary separation hardening. The other group, "weak boundary," is defined as the ones basically separating, which leads to minor surface diffusion. At an early stage of deformation, weak grain boundaries elastically separate to certain tiny amount, while at tough boundaries small number of dislocation emits as a precursor of grain boundary rearrangement activities. Thus, grain boundary incompatibilities occur between these tough and weak boundaries and cause stress concentration at triple

junctions of the boundaries. With increased loading, such stress concentration makes voids nucleate at triple junctions and weak boundaries. Consequently, void coalescence and loss of triaxiality by forming nano whiskers develop in the materials. These whiskers act as special chains of width around 20 nanometers to form nano damage zones. Moreover, within the whisker chains, grain boundary sliding, surface diffusion and dislocation take place and therefore spread plasticity to provide such ultra-fine granular materials with certain ductility.

As discussed above, the tough boundary and weak boundary are the two key elements during the multiple cooperative separation processes. However, one remaining question is how grain boundary structures such as misorientations and interfacial impurities are quantitatively related to the tough and weak boundaries and further affect the strength and ductility of nano-grained materials. In recent years, nano-twinned structures have also been extensively investigated to see that the nano-twins activate dislocation-slips only at high stress state, but once slips start, they disperse slip activities effectively, relieving stress concentration at the triple junctions and delaying grain boundary separation (Lu, *et al.*, 2009). In turn, nano twinned materials are capable of providing both high strength and high ductility. However, there are no satisfactory models of predicting the high ductility of nano-twinned structures, while the strength has been well predicted by dislocation models based on MD-simulations (Li, *et al.*, 2010).

1.3 Approaches for capturing characteristics of grain boundary failures

To understand how grain boundary strength and separation mechanisms affect strength and ductility of nanocrystalline materials, it is necessary to formulate a constitutive law between macroscopic material strength and grain boundary structures such as misorientations and interfacial impurities. However, multiscale modeling of hierarchical and process-dependent material characteristics is challenging since no existing methodologies can handle this type of problems so far. In general, molecular dynamics simulation is commonly used for investigating physical properties of materials at molecular scales. But, full-scale molecular dynamics calculation for macroscopic problems is not amenable due to huge computation demands. On the other hand, continuum-based analyses including scale-dependent features, such as the discrete dislocation (DD) analysis (Van der Giessen & Needleman, 1995) and the finite element method (FEM) with user-defined cohesive zone laws between atomic planes (Gao & Bower, 2004), can be applied for multiscale modeling. Nevertheless, in DD, material parameters have to be tuned carefully to reflect plastic deformation of real materials. Besides, FEM which is based on conventional continuum plasticity theories cannot capture non-volume-preserving plastic deformation of materials.

Therefore, a new means of handling hierarchical and process-dependent material deformation is required. In this thesis, the interior and exterior field projection methods of grain boundaries are developed for computation and experiment respectively. It has to be noted that the field projection methods provide unique ways of representing grain boundary intrinsic traction-separation relationship in a view of continuum. Then, by

employing grain boundary cohesive features which are collected by field projection methods in FEM, deformation analyses of nanocrystalline materials at macroscopic scales can be achieved. Hence, the constitutive law between material strength and grain boundary structures at large scales can be constructed.

In addition to the grain boundary field projection methods, we introduce an invention of an experimental instrument – atomic force microscope (AFM) interferometry. The AFM interferometry is a novel technique for precise measurements of in-plane displacement distributions of solid surface atoms in sub-nanometer resolution. The high resolution measurement of localized atomic deformation provides essential information for interrogating interfacial characteristics between nanostructures. For the development of AFM interferometry, calibration experiments are carried out by measuring atomic lattices distortions across a mosaic boundary of highly oriented pyrolytic graphite.

This thesis is organized as follows. Chapter 2 addresses grain boundary embrittlement by studying the effects of impurities at grain boundaries and tilt angles between adjacent grains on grain boundary strength, with molecular statics simulations. In addition, this chapter includes the contents of the interior field projection method. Chapter 3 covers the exterior field projection method. Chapter 4 describes the experimental work of AFM interferometry, including principles, instrumentation, experimental procedures, signal processing and measurement results. At the end of thesis, Chapter 5 contains conclusions and future directions of the whole thesis.

Chapter 2. Interior Field Projection Method

2.1 Effects of dopants and tilt angles on mechanical behaviors of grain boundaries

Since Hampe addressed the metallurgies of copper in 1874 (Hampe, 1874), the bismuth or lead embrittlement of copper is a very well known problem. However, the underlying mechanisms of how minute concentrations of bismuth or lead in copper can cause the otherwise tough metal to fall apart at grain boundaries is still not well-established (Donald & Brown, 1979; Sutton & Vitek, 1982; Eckert *et al.*, 1987; Sigle *et al.*, 2002). Recently, several postulations based on modification of electronic structures and chemical bonds in the presence of impurities have been put forth to explain the dramatically reduced fracture toughness of the material. The first speculation was that the metal-impurity bonding draws charge from neighboring metal-metal bonds, thereby weakening the metal-metal bonds along the grain boundary (Messmer & Briant, 1982). The second theory suggested that the directional bonds formed between an impurity and the host metal across the grain boundary reduces the ease of atomic rearrangement required for grain boundary plasticity, as compared to the non-directional metallic bonds between grains in the absence of impurities (Haydock, 1981). The third hypothesis attributed embrittlement to a size effect, where the large impurity atoms weaken the

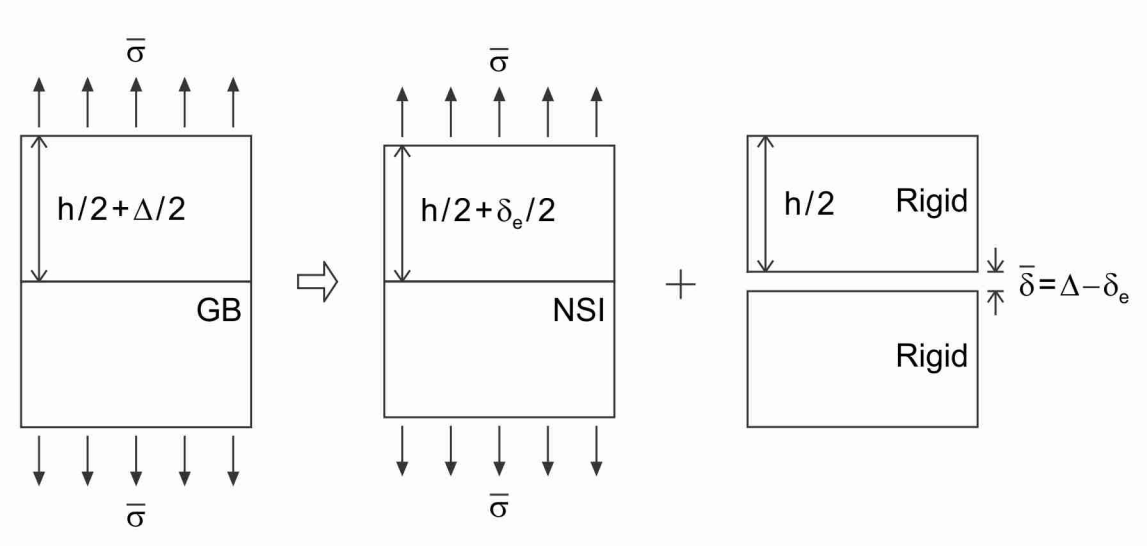

Figure 2.1 Schematic of the global traction-separation grain boundary characteristics. Decomposition of the applied displacement Δ in the uniaxial straining of a symmetric tilt grain boundary into the contributions from stretching of a bulk elastic body δ_e and an equivalent grain boundary separation $\bar{\delta}$.

interatomic bonding by pushing apart the host metal atoms at the grain boundary interface (Sutton & Vitek, 1982). While ab initio studies carried out to examine the material's electronic structural changes and the local density of states at the grain boundary in the presence of impurities (Goodwin *et al.*, 1988; Duscher *et al.*, 2004; Schweinfest *et al.*, 2004) have either supported or dispelled these arguments, a common ground on the mechanism behind grain boundary embrittlement has yet been reached.

To gain insights into the separation processes of grain boundaries, we study the mechanical response of both pure and Pb doped Cu symmetric tilt grain boundaries under uniaxial straining. The model problem consists of $55a \times 55a \times 2a$ simulation cell, where a is the lattice constant, with the grain boundary interface located in the $x_2 = 0$ plane. The energetics of the molecular interactions is governed by the EAM potential (Daw &

Baskes, 1984) in the classical molecular dynamics simulation package LAMMPS (Plimpton, 1995). The simulation cell uniformly stretches in the x_2 direction by $2a$ thick rigid grips at the ends with an incremental strain of $d\varepsilon_{22}^{A} = 5\times10^{-4}$, with periodic boundary conditions enforced in the x_1 and x_3 directions. After each strain increment, the rigid grips are held fixed, while the conjugate gradient method is used to minimize the energy of the system. The average uniaxial stress in the system $\bar{\sigma}$ is then calculated using the virial theorem (Clausius, 1870). Next, the global traction-separation laws are obtained by decomposing the applied stretch Δ into the contributions from the elastic stretching of the simulation cell with no separation interface (NSI) δ_e, and also an equivalent separation of the grain boundary interface $\bar{\delta} = \Delta - \delta_e$ (Figure 2.1) which is re-expressed as

$$\bar{\delta} = \left(\varepsilon_{22}^{A} - \frac{\bar{\sigma}}{E^*} \right) h, \tag{2.1}$$

where h is the simulation domain height, E^* the effective secant modulus of the crystal, and $\varepsilon_{22}^{A} = \Delta/h$ the global applied strain. The superscript A in $\varepsilon_{22}^{\mathrm{A}}$ is denoted by P for pure Cu or D for Pb doped Cu. Note that this $\bar{\sigma} - \bar{\delta}$ relationship is independent of h only in the absence of periodic dislocation emission from the grain boundary to the bulk crystal. Following dislocation emission into the bulk, the bulk material hardens substantially, and the ductility of the crystal is increased. The simulation domain height h sets the limit to the extent of hardening, and is representative of the grain size. The size-dependent grain boundary toughness can be approximately estimated as

$$\Gamma_{GB} \simeq \Gamma_e + \Gamma_p \cdot \frac{d}{d_0} \tag{2.2}$$

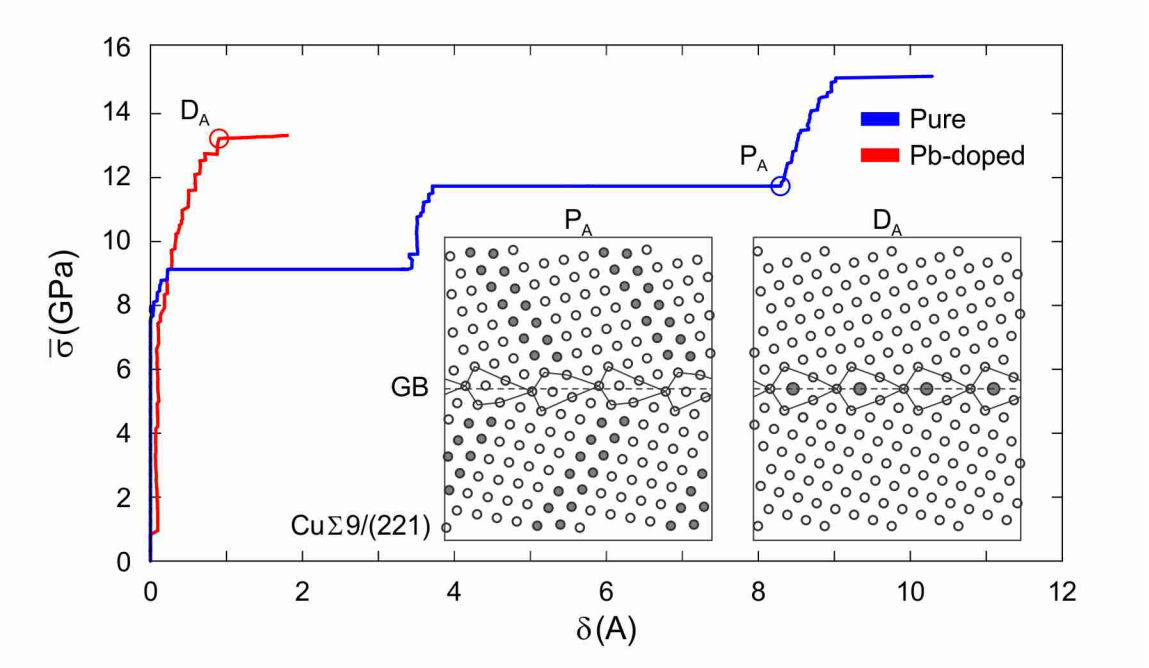

Figure 2.3 Average traction-separation relationship for pure and Pb doped Cu ∑9/(221) grain boundaries.

where d_0 is the grain size of current analysis domain, Γ_e the grain boundary toughness related to initial deformations of grain boundary layers including atomic rearrangement activities without dislocation emission, Γ_p the grain boundary toughness related to its plastic deformation dislocation emission from the grain boundaries corresponding to the grain size of d_0, and d the size of various grains to be interrogated. The Equation (2.2) indicates that overall grain boundary separation toughness depends on the grain size. The hardening work in post dislocation emission prior to subsequent dislocation emission also contributes to the grain boundary toughness. Moreover, the intergranular fracture of nanocrystalline materials typically is governed by stress-controlled loading rather than strain-controlled loading. In the cases with the presence of dislocation emission from the

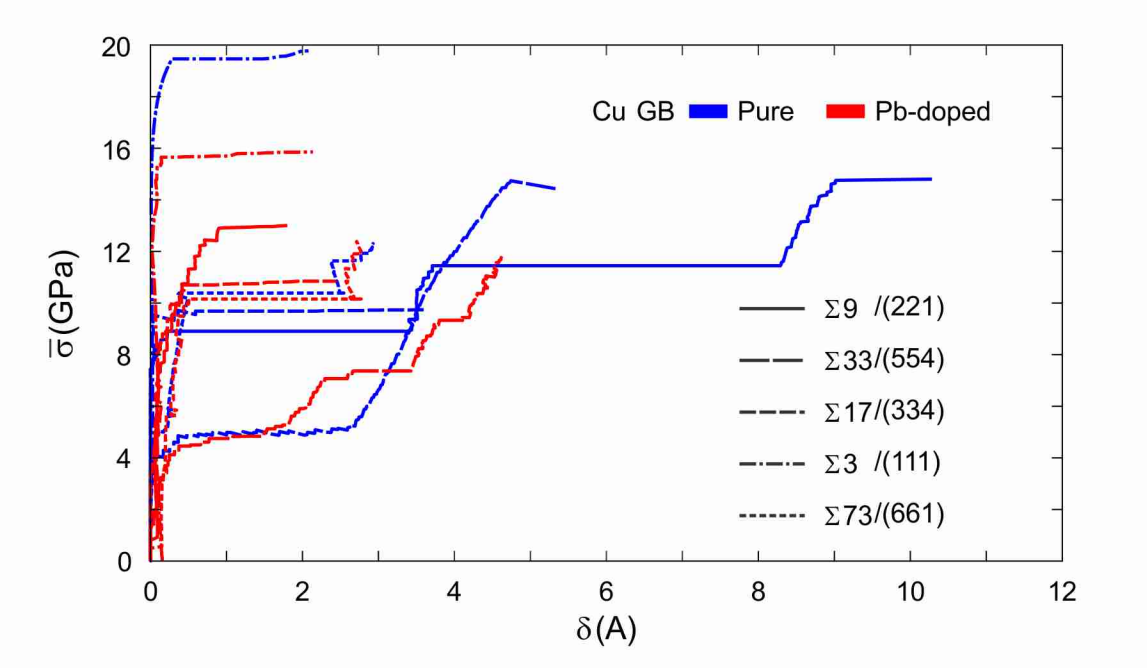

Figure 2.4 Comparison of the average traction-separations along the pure and Pb-doped Cu symmetric tilt grain boundaries with different tilt angles.

grain boundary, the separation process follows the constant loading paths with multiple dislocation emissions into the bulk respectively under stress-controlled loadings.

Figure 2.2 and Figure 2.3 show the average traction $\bar{\sigma}$ versus local separation $\bar{\delta}$ profiles for pure and Pb doped Cu $\sum 5/(310)$ and Cu $\sum 9/(221)$ symmetric tilt grain boundaries of h at 20 nm respectively. These tilt geometries are typical examples of inherently brittle ($\sum 5$) and ductile ($\sum 9$) grain boundary systems. For the $\sum 5$ grain boundary, we note that the presence of dopants stiffens the grain boundary, and lowers the toughness of the grain boundary by nearly two-fold (area enveloped by the $\bar{\sigma} - \bar{\delta}$ profile). While some atomic rearrangement at the grain boundary occurs from P_A to P_B for the pure Cu $\sum 5$ grain boundary, no observable atomic rearrangement is observed for Pb doped Cu. For both cases, however, dislocation emission from the grain boundary is

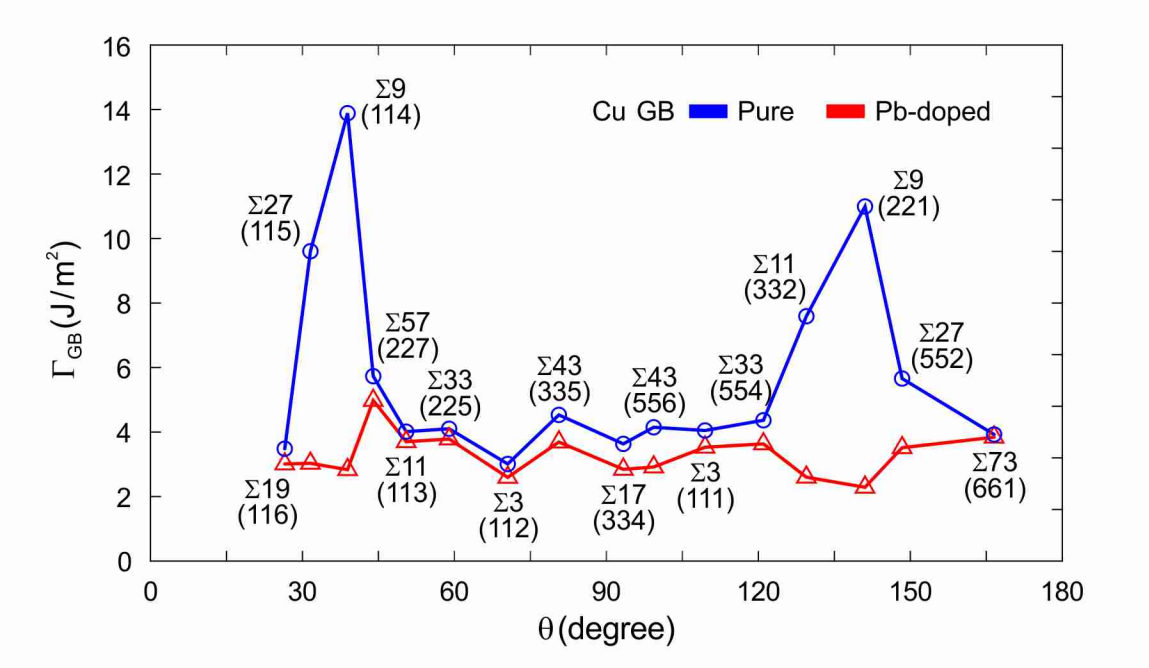

Figure 2.5 Comparison of the toughness of the pure and Pb-doped Cu symmetric tilt grain boundaries with different tilt angles.

not observed, confirming that this ∑5 grain boundary is brittle. For the ∑9 grain boundary, emission of partial dislocations at periodic sites is observed at P_A for the pure Cu grain boundary. Such periodic emission of dislocations from the grain boundary to the bulk has been also observed experimentally (Yin, 1998). On the contrary, the Pb dopants at the grain boundary depicted in gray color in the right inset of Figure 2.3 maintain the symmetric configuration and thus suppress the dislocation emission from the grain boundary at D_A, which is under the loading similar to the one at P_A. Therefore, for this doped case, toughening of the crystal can only occur up to the maximum stress level at point D_A, beyond which the grain boundary fails.

Dopant atoms larger than the host metal atoms often segregate to the grain

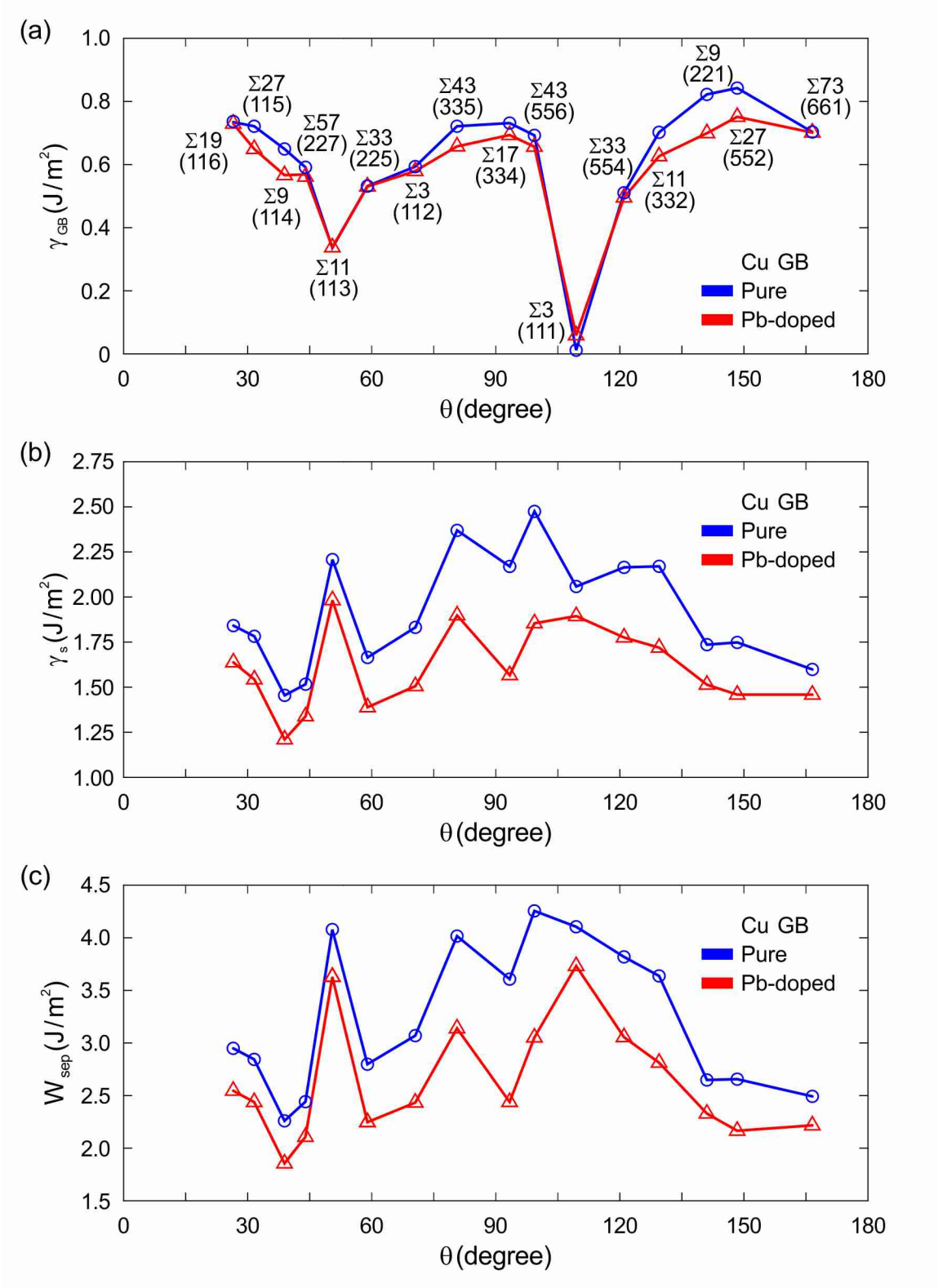

Figure 2.6 Comparison of the grain boundary energy (a), surface energy (b) and work of separation (c) of the symmetric bicrystals of pure and Pb doped Cu of different tilt angles.

boundaries, where they substitute the host metal atoms at periodic boundary sites with the largest space. These preferred sites correspond to the periodic maximum tensile traction sites, where the host metal bonds are highly strained. Molecular statics simulations based on the conjugate gradient method confirm that the minimum energy configuration consists of Pb dopant atoms which substitute pre-existing Cu atoms along the grain boundary at the high tensile stress site within each grain boundary period. Other than dopant atoms, we also need to consider the effects of misorientation in bicrystals on grain boundary embrittlement of Cu (Li & Zhang, 1995). In order to investigate the effect of misorientation between two adjacent grains on grain boundary strength, the uniaxial strain simulations are also implemented for both the pure Cu and Pb doped Cu grain boundaries of ∑9/(221), ∑33/(554), ∑17/(334), ∑3/(111) and ∑73/(661), which can be the representative symmetric tilt grain boundaries of tilt angles between 60 to 180 degrees. In Figure 2.4, by overall comparison of the pure and Pb doped Cu grain boundaries, it is clear that the Pb dopants on grain boundaries can make materials brittle effectively. It also must be noticed that the embrittlement levels are not the same in different grain boundary misorientations.

For the Cu ∑73/(661), ∑33/(554), ∑3/(111) and ∑17/(334) grain boundaries, which have very low or extreme high misorientations, the toughness changes due to the Pb dopants on grain boundaries are not obvious. The toughness of the pure and Pb-doped Cu symmetric tilt grain boundaries with different tilt angles is also presented in Figure 2.5. Furthermore, Figure 2.6(a) represents the grain boundary energies of pure Cu and Pb doped Cu grain boundaries with different misorientations. The Pb doped Cu grain boundary energies are all smaller than the pure grain boundaries with corresponding

misorientation. It is generally agreed that dopants can make materials brittle, or one puts it another way that the dopants can make interfaces between two grains essentially weak (Lozovoi *et al.*, 2006; Laporte & Mortensen, 2009). Moreover, Figure 2.6(b) and (c) present the surface energies and works of separation of pure Cu and Pb doped Cu grain boundaries with various bicrystal tilt angles. However, neither the works of separation nor the grain boundary energies of different orientation has strong relevance to the levels of grain boundary embrittlement due to dopants and various misorientations of symmetric tilt grain boundaries.

2.2 Combination of kinematics of discrete atomistics and continuum fields

The above simulations clearly show that the presence of dopants embrittles the grain boundary. However, to fully understand the nanomechanisms responsible for this embrittlement process, we need to quantitatively determine the local traction-separation distribution along the grain boundary. This task however is highly nontrivial due to the discreteness of the atomic system (Figure 2.7; Figure 2.8) which results in inconsistencies in the definition of stress (Choi & Kim, 2007; Wang *et al.*, 2011). In molecular dynamics, for example, the virial stress is widely used to interpret physical continuum properties. The open circles in Figure 2.9 show the interpolated virial stresses σ_{22} of atomic sites along a $\sum 5/(310)$ symmetric tilt grain boundary in Cu, connected by linear (Figure 2.10) and spline interpolations. Observe that neither the linear interpolation nor the spline interpolation of the conventional virial stress distributions satisfy the basic equilibrium

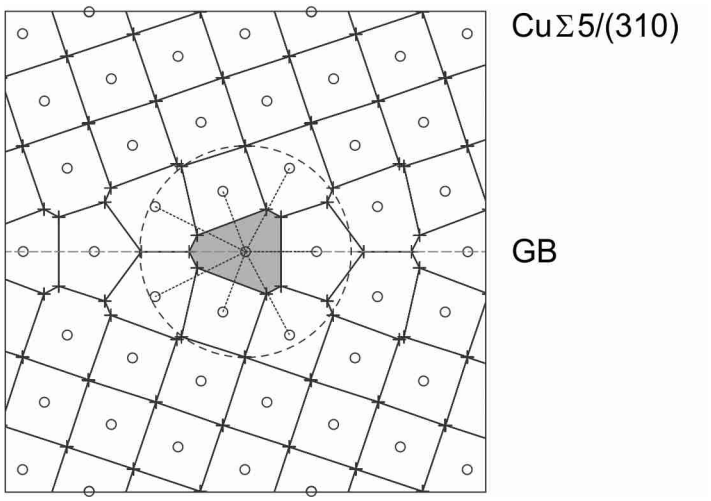

Figure 2.7 Volume domains of grain boundary atoms of Cu ∑5/(310).

requirement in the absence of far-field loading, i.e. sum of forces $= 0$. Therefore, to assess the strength and the toughness of the grain boundaries, we must have proper field representation of the grain boundary which satisfies balance laws to investigate cooperative failure processes of grain boundary separations.

As stated previously, the discrete atomic system causes inconsistencies in the definition of stress. Here, we develop an algorithm to find the best representative stress field for atomistics which satisfies the linear momentum balance law. For a static system without body forces, the linear momentum balance equation for a solid is stated as

$$\sigma_{ij,j} = 0, \tag{2.3}$$

where $\boldsymbol{\sigma}$ is tensorial stress at certain position $\mathbf{X}$ in the solid, $\sigma_{ij,j}$ denotes partial derivatives of σ_{ij} in x_j direction and the summation convention is adopted for the repeated indices. In molecular computation, the virial stress is used commonly as a generalized point of view in the virial theorem, developed by Clausius (Clausius, 1870),

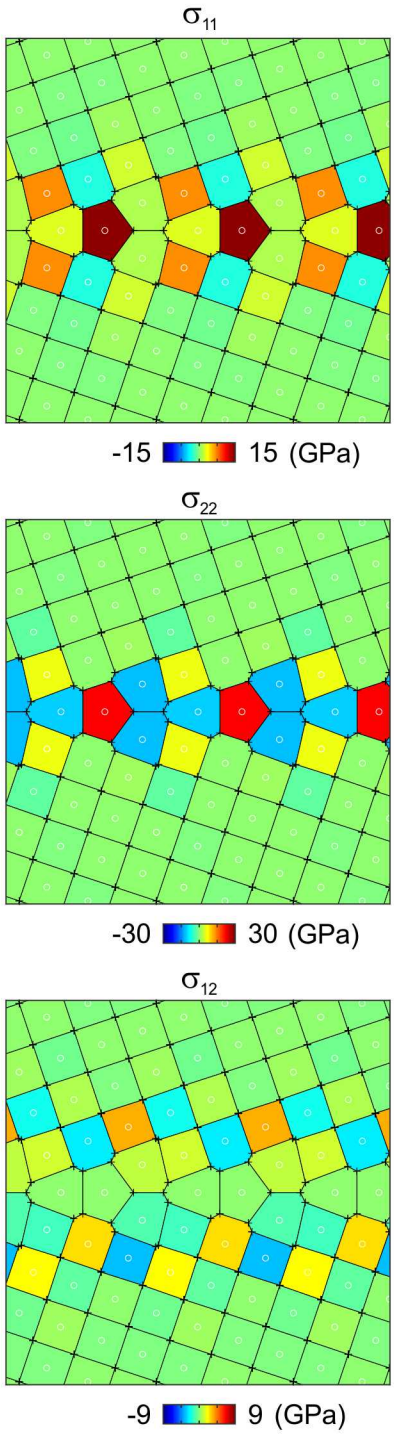

Figure 2.8 Virial stresses in discrete near grain boundaries of Cu ∑5/(310) from molecular statics calculation.

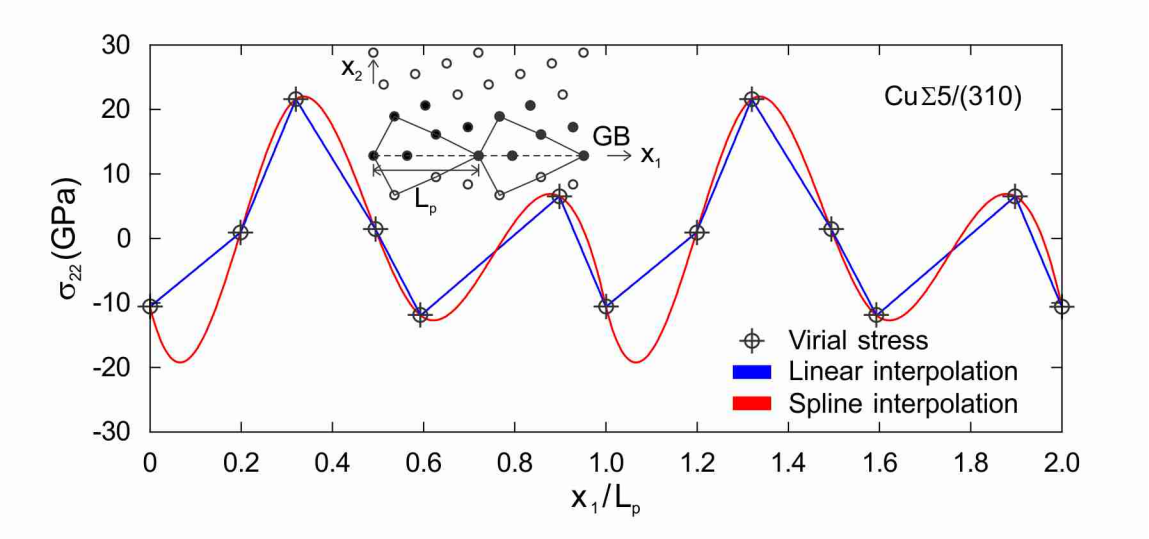

Figure 2.9 Virial stress distributions of grain boundary atoms of Cu ∑5/(310) from molecular statics calculation.

$$\sigma_{ij}^{(\alpha)} = \frac{1}{\Omega^{(\alpha)}}\left[-m^{(\alpha)}\left(v_i^{(\alpha)} - \overline{v}_i\right)\left(v_j^{(\alpha)} - \overline{v}_j\right) + \frac{1}{2}\sum_{\beta}\left(x_i^{(\beta)} - x_i^{(\alpha)}\right) f_j^{(\alpha\beta)}\right], \tag{2.4}$$

where $\Omega^{(\alpha)}$, $m^{(\alpha)}$, $v_i^{(\alpha)}$ and $x_i^{(\alpha)}$ are the atomic volume illustrated in Figure 2.7, mass, the *i*-th component of velocity and the *i*-th component of position of atom α respectively; $x_i^{(\beta)}$ is the *i*-th component of position of atom β which locates in domain $\Omega^{(\alpha)}$; $f_j^{(\alpha\beta)}$ is the *j*-th component of force on atom α applied by atom β, and $\overline{v}_i$ is the *i*-th component of average velocity over domain $\Omega^{(\alpha)}$. When a solid is considered as in a static situation or at rest in average in a macroscopic point of view, the terms contributed by velocity fields vanish in virial stress calculations. Through the virial theorem, atomic stresses can be calculated in a discrete form for the corresponding voronoi cells of atoms. Figure 2.8 shows the virial stresses of the voronoi cells of atoms near pure Cu ∑5/(310) symmetric tilt grain boundaries through molecular statics calculation. Let $\sigma_{ij}^{(a)}$ denote the stress

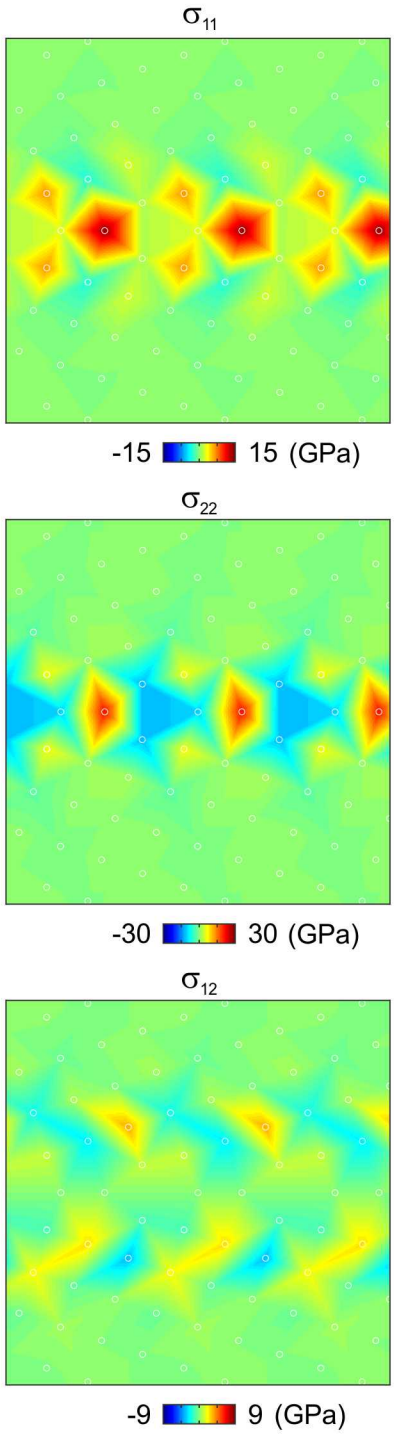

Figure 2.10 Virial stress distributions near grain boundaries of Cu ∑5/(310) through direct linear interpolations of molecular statics information.

component σ_{ij} at the atomic site $a = 1,2,\ldots,M$. The stresses at these atomic sites are then expressed as a vector $\boldsymbol{\sigma}_{ij}^{a}$ written as

$$\boldsymbol{\sigma}_{ij}^{a} = \left[\sigma_{ij}^{(1)} \quad \sigma_{ij}^{(2)} \quad \cdots \quad \sigma_{ij}^{(M)} \right]^{T}. \tag{2.5}$$

Through linear interpolation of the stress vector at the atomic sites $\boldsymbol{\sigma}_{ij}^{a}$, the stress distributions within the domain which is occupied by the atoms can be directly estimated as

$$\sigma_{ij}\left(\mathbf{x}\right) = \mathbf{N}_{a}\left(\mathbf{x}\right)^{T} \boldsymbol{\sigma}_{ij}^{a}, \tag{2.6}$$

where $\mathbf{N}_{a}\left(\mathbf{x}\right) = [N^{(1)}\left(\mathbf{x}\right) \quad N^{(2)}\left(\mathbf{x}\right) \quad \cdots \quad N^{(M)}\left(\mathbf{x}\right)]^{T}$ is the linear interpolation function vector for the M atomic sites. The linear interpolated stress fields near pure Cu ∑5/(310) grain boundaries are presented in Figure 2.10. In order to find the best representative stress field of the atoms near grain boundary, we generate a constrained minimization problem in the Euclidian error norm as follows

$$\text{minimize} \qquad E\left[\boldsymbol{\sigma}_{ij}^{a}\right] = \int_{V} \left[\left(\sigma_{1j,j}\right)^{2} + \left(\sigma_{2j,j}\right)^{2} \right] dv \tag{2.7}$$

$$\text{subjected to} \qquad \left\| \tilde{\boldsymbol{\sigma}}_{ij}^{a} - \boldsymbol{\sigma}_{ij}^{a} \right\|^{2} = 0 \qquad \text{in } V \tag{2.8}$$

where $\tilde{\boldsymbol{\sigma}}_{ij}^{a}$ is the optimized stress vector for the M atomic sites which satisfies the linear momentum balance equation the most. Then, the constraints can be incorporated into a modified error functional by using the Lagrange multiplier method (Bertsekas, 1982) as

$$\text{minimize} \qquad E\left[\boldsymbol{\sigma}_{ij}^{a}, \lambda\right] = \int_{V} \left[\left(\sigma_{1j,j}\right)^{2} + \left(\sigma_{2j,j}\right)^{2} \right] dv + \lambda \left\| \tilde{\boldsymbol{\sigma}}_{ij}^{a} - \boldsymbol{\sigma}_{ij}^{a} \right\|^{2} \tag{2.9}$$

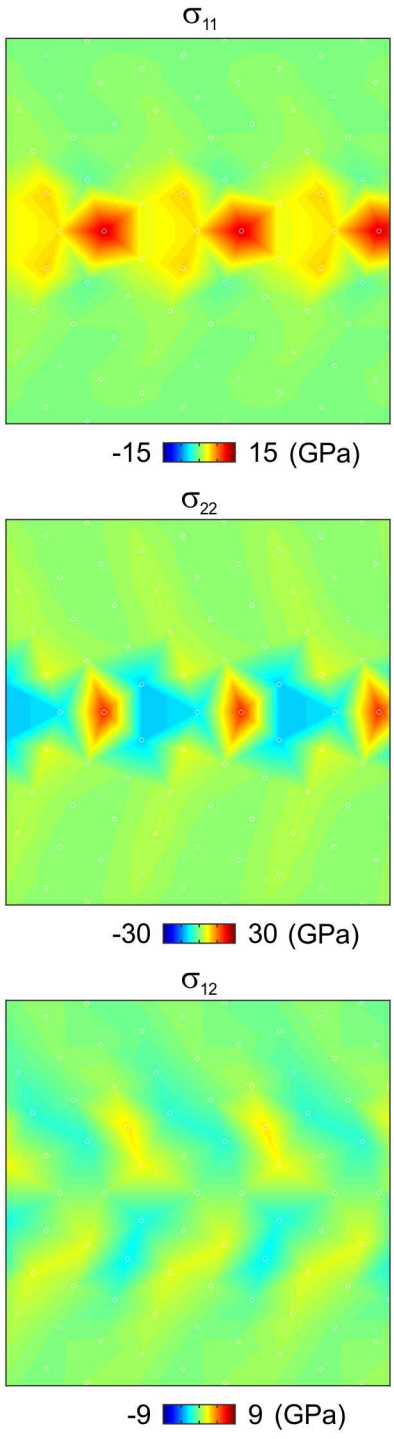

Figure 2.11 Virial stress distributions near grain boundaries of Cu ∑5/(310) through linear interpolations of molecular statics information with the adjustment for linear momentum balance.

where λ is a scalar of Lagrange multiplier. Then, the stress distribution $\tilde{\sigma}_{ij}(\mathbf{x})$ which satisfies the equilibrium equation the most within V can be evaluated using the optimized stress vector $\tilde{\boldsymbol{\sigma}}_{ij}^{a}$.

To demonstrate the capability of the above optimization method for the virial stress adjustment to satisfy the linear momentum balance the most, the proposed optimization scheme is applied to the linear interpolated stress fields near pure Cu $\sum 5/(310)$ grain boundaries shown in Figure 2.10. A 256 ×256 square sampling grid is constructed within the domain V of $0 \le x_1 \le L_P$ ($L_P = 5.716$ Å) and $0 \le x_2 \le 11.308$ Å shown in Figure 2.8 for the error functional evaluation. Through this algorithm, the best stress vector $\tilde{\boldsymbol{\sigma}}_{ij}^{a}$ of the atoms within V is obtained, and the interpolated stress fields $\tilde{\sigma}_{ij}(\mathbf{x})$ and residual errors $R(\mathbf{x}) = [(\sigma_{1j,j})^2 + (\sigma_{2j,j})^2]^{1/2}$ are then calculated using the optimized stress vector $\tilde{\boldsymbol{\sigma}}_{ij}^{a}$ respectively (Figure 2.11; Figure 2.12). Compared to the stress fields based on the original virial stresses, the stress fields interpolated by adjusted atomic stresses not only have smaller residual errors in the region near the grain boundary but also contain the positive and negative stress zones in the orientations more aligned to the possible easy-glide directions of the bicrystal. Therefore, through the adjustment for linear momentum balance on virial stresses of atomistics, the most representative discrete atomic stress fields which mostly satisfy equilibrium conditions in continuum can be found.

As stated before, to ascertain the strength and the toughness of the grain boundaries and subsequently the embrittling effects of impurities and misorientations of bicrystals, an accurate and quantitative assessment of the grain boundary field

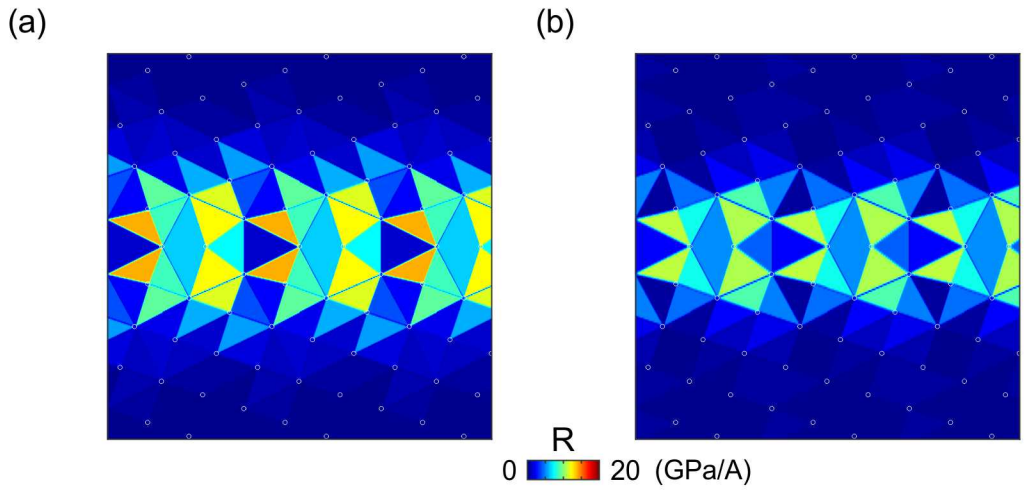

Figure 2.12 Comparison of the linear momentum balance residuals near Cu ∑5/(310) grain boundaries through direct linear interpolations (a) and the adjustment for linear momentum balance (b) of virial stresses.

descriptions with atomic size-dependence features of nanocrystalline materials are required. In this study, we develop an interior field projection method to bridge the information of molecular level to the fields in continuum scale to determine the grain boundary traction-separation characteristics. The central point of the interior field projection method is the principle of virtual work. The external virtual work equals to the internal virtual work when unrelated but kinematically admissible virtual fields of atomic position variations are applied in the real system. The internal forces are in equilibrium though nonlocal interatomic interactions such as the embedded atom method (EAM) potential interaction. Then, by the equivalence between external and internal virtual work, field-projected subatomic-resolution traction distributions on a variety of grain boundaries are determined. Consider the atom a, which occupies the volume Ω_a through the voronoi diagram in the atomic region shown in Figure 2.13, and the interatomic

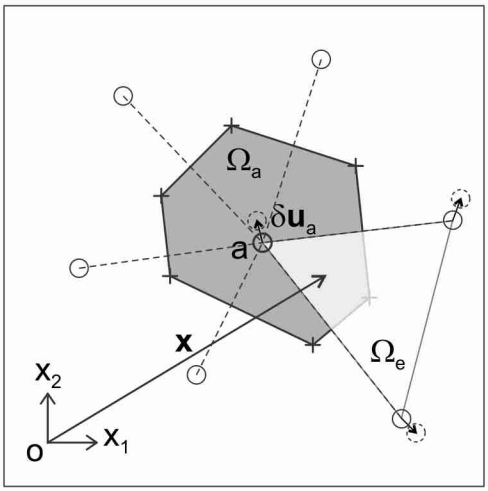

Figure 2.13 Sketch of virtual potential energy calculation domains of the voronoi cell of atom a and the element e with linear interpolation functions.

potential energy density of within Ω_a can be represented as a function of strains $\phi = \phi(\varepsilon_{11}, \varepsilon_{22}, \varepsilon_{12})$ for two-dimensional problems. As this atom is subjected the virtual strain resulted from the virtual displacement $\delta\mathbf{u}_a$ which is work-conjugate to the Cauchy stresses, the variation of interatomic potential energy density of this voronoi cell can be expanded using Taylor series, which is an infinite sum of terms that are evaluated from the exactly initial state as

$$\begin{aligned}
&\phi(\varepsilon_{11}+\delta\varepsilon_{11}, \varepsilon_{22}+\delta\varepsilon_{22}, \varepsilon_{12}+\delta\varepsilon_{12}) \\
&= \phi(\varepsilon_{11}, \varepsilon_{22}, \varepsilon_{12}) + \left(\delta\varepsilon_{11}\frac{\partial}{\partial\varepsilon_{11}} + \delta\varepsilon_{22}\frac{\partial}{\partial\varepsilon_{22}} + \delta\varepsilon_{12}\frac{\partial}{\partial\varepsilon_{12}}\right)\phi(\varepsilon_{11}, \varepsilon_{22}, \varepsilon_{12}) + \\
&\frac{1}{2!}\left(\delta\varepsilon_{11}\frac{\partial}{\partial\varepsilon_{11}} + \delta\varepsilon_{22}\frac{\partial}{\partial\varepsilon_{22}} + \delta\varepsilon_{12}\frac{\partial}{\partial\varepsilon_{12}}\right)^2 \phi(\varepsilon_{11}, \varepsilon_{22}, \varepsilon_{12}) + \cdots
\end{aligned} \tag{2.10}$$

Since the amplitudes of virtual strains are set very small, the terms equal to or higher than the second order can be ignored reasonably. Therefore, the variation of interatomic potential energy density is approximately written as

$$\delta\phi = \left(\delta\varepsilon_{11} \frac{\partial}{\partial \varepsilon_{11}} + \delta\varepsilon_{22} \frac{\partial}{\partial \varepsilon_{22}} + \delta\varepsilon_{12} \frac{\partial}{\partial \varepsilon_{12}} \right) \phi\left(\varepsilon_{11}, \varepsilon_{22}, \varepsilon_{12}\right). \tag{2.11}$$

In general, since the strain energy varies throughout a deformed solid, strain energy density is useful to depict the quantity of energy stored in a solid of infinitesimal volume. Moreover, in elastic materials, strain energy density can be represented in terms of the strain tensors of small deformations, and the derivative of the above expression of strain energy density with respect to strains equals the tensorial stress of an infinitesimal region. Hence, variation of interatomic potential energy density is further expressed as

$$\delta\phi = \sigma_{11}\delta\varepsilon_{11} + \sigma_{22}\delta\varepsilon_{22} + \sigma_{12}\delta\varepsilon_{12}. \tag{2.12}$$

To apply the principle of virtual work to atomistics, a kinematically admissible virtual displacement field $\delta u(\mathbf{x})$, which is continuous, differentiable in the domain V and satisfies $\delta u(\mathbf{x}) = 0$ on the boundary S of V has to be defined. A domain near Cu $\sum 5/(310)$ grain boundaries is shown in Figure 2.14, and the color contour represents the volumes of the atomic voronoi cells. We divide the domain V into four regions, D_1, D_2, D_3, and D_0, where D_1, D_2 and D_3 make up the volume V with bounding surface S, and D_0 is outside the volume V. The interface lies along the grain boundary $x_2 = 0$, where the tractions are to be determined. Then, the virtual displacement fields are set as

$$\delta\mathbf{u}\left(x_1, x_2\right) = \hat{u}_i \mathbf{e}_i F\left(x_1\right) G\left(x_1, x_2\right) \quad i = 1,2 \tag{2.13}$$

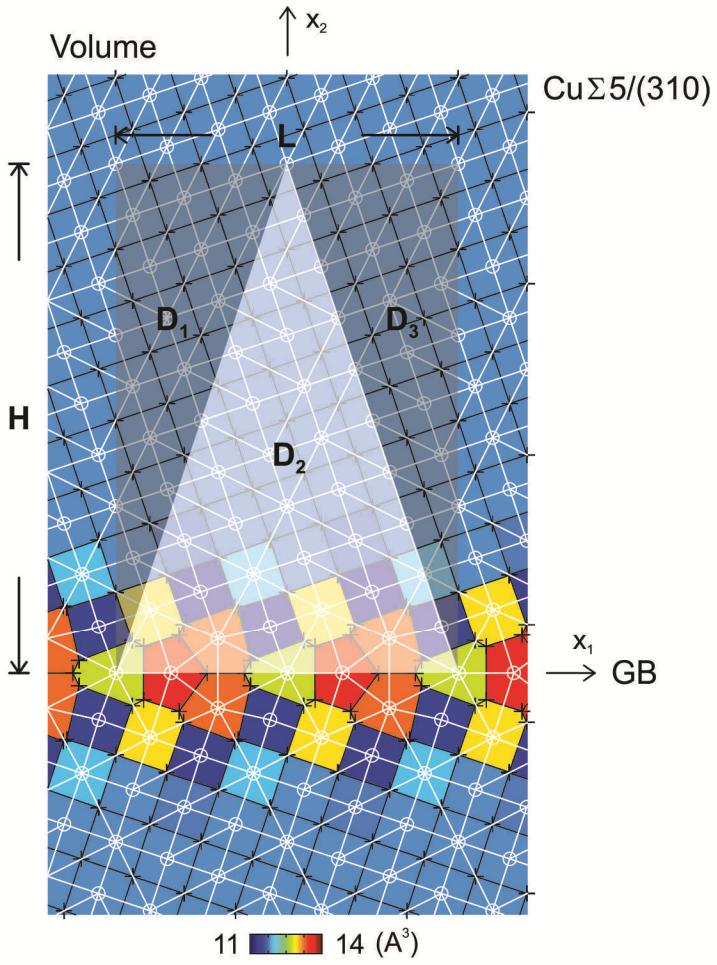

Figure 2.14 Atomic volumes of the atoms in the region nearby Cu ∑5/(310) grain boundaries and the calculation domain of the interior field projection method for extracting the grain boundary traction distributions.

where $\hat{u}_i$ is virtual displacement amplitudes in x_i direction, $F(x_1)$ cosine or sine, which is a 2π -periodic of basis function, and $G(x_1, x_2)$ the perturbation-displacement envelope function which is designed in a special way to make a kinematically admissible virtual displacement field. In this way, the virtual displacement field $\delta\mathbf{u}$ can have unit perturbation value of the virtual displacement amplitudes along interface but decay

smoothly to zero at the other boundaries. The cosine or sine basis function $F(x_1)$ and the perturbation-displacement envelope function $G(x_1, x_2)$ are defined as

$$F(x_1) = \cos\left(\frac{2m\pi x_1}{L}\right) \text{ or } \sin\left(\frac{2m\pi x_1}{L}\right) \tag{2.14}$$

and

$$G(x_1, x_2) = \begin{cases} \left(\frac{H}{x_2} - 1\right)\left(1 + \frac{2x_1}{L}\right) & \text{for } (x_1, x_2) \in D_1 \\ \left(1 - \frac{x_2}{H}\right) & \text{for } (x_1, x_2) \in D_2 \\ \left(\frac{H}{x_2} - 1\right)\left(1 - \frac{2x_1}{L}\right) & \text{for } (x_1, x_2) \in D_3 \\ 1 & \text{for } (x_1, x_2) \in D_0 \end{cases} \tag{2.15}$$

where m is the wave number, L the width and H the height of the domain V. The virtual strains due to a normal perturbation in the cosine basis function of wave number m can be written further as

$$\begin{Bmatrix} \delta\varepsilon_{22} \\ \delta\varepsilon_{12} \end{Bmatrix} = \hat{u}_2 \begin{Bmatrix} \frac{-H}{L{x_2}^2}(2x_1 + L)\cos\left(\frac{2m\pi x_1}{L}\right) \\ \frac{(-x_2 + H)}{L^2 x_2}\left[L\cos\left(\frac{2m\pi x_1}{L}\right) - m\pi(2x_1 + L)\sin\left(\frac{2m\pi x_1}{L}\right)\right] \end{Bmatrix} \tag{2.16}$$

for $(x_1, x_2) \in D_1$,

$$\begin{Bmatrix} \delta\varepsilon_{22} \\ \delta\varepsilon_{12} \end{Bmatrix} = \hat{u}_2 \begin{Bmatrix} \frac{-1}{H}\cos\left(\frac{2m\pi x_1}{L}\right) \\ \frac{m\pi(x_2 - H)}{LH}\sin\left(\frac{2m\pi x_1}{L}\right) \end{Bmatrix} \tag{2.17}$$

for $(x_1, x_2) \in D_2$,

$$\begin{Bmatrix} \delta\varepsilon_{22} \\ \delta\varepsilon_{12} \end{Bmatrix} = \hat{u}_2 \begin{Bmatrix} \dfrac{-H}{Lx_2^{\,2}}\left(-2x_1+L\right)\cos\left(\dfrac{2m\pi x_1}{L}\right) \\ \dfrac{\left(x_2-H\right)}{L^2x_2}\left[L\cos\left(\dfrac{2m\pi x_1}{L}\right)+m\pi\left(-2x_1+L\right)\sin\left(\dfrac{2m\pi x_1}{L}\right)\right] \end{Bmatrix} \tag{2.18}$$

for $(x_1, x_2) \in D_3$ and $\varepsilon_{11} = 0$ for $(x_1, x_2) \in V$. Similarly, the virtual strains due to a normal perturbation in the sine basis function of wave number m can be expressed as

$$\begin{Bmatrix} \delta\varepsilon_{22} \\ \delta\varepsilon_{12} \end{Bmatrix} = \hat{u}_2 \begin{Bmatrix} \dfrac{-H}{Lx_2^{\,2}}\left(2x_1+L\right)\sin\left(\dfrac{2m\pi x_1}{L}\right) \\ \dfrac{\left(-x_2+H\right)}{L^2x_2}\left[m\pi\left(2x_1+L\right)\cos\left(\dfrac{2m\pi x_1}{L}\right)+L\sin\left(\dfrac{2m\pi x_1}{L}\right)\right] \end{Bmatrix} \tag{2.19}$$

for $(x_1, x_2) \in D_1$,

$$\begin{Bmatrix} \delta\varepsilon_{22} \\ \delta\varepsilon_{12} \end{Bmatrix} = \hat{u}_2 \begin{Bmatrix} \dfrac{-1}{H}\sin\left(\dfrac{2m\pi x_1}{L}\right) \\ \dfrac{m\pi\left(-x_2+H\right)}{LH}\cos\left(\dfrac{2m\pi x_1}{L}\right) \end{Bmatrix} \tag{2.20}$$

for $(x_1, x_2) \in D_2$,

$$\begin{Bmatrix} \delta\varepsilon_{22} \\ \delta\varepsilon_{12} \end{Bmatrix} = \hat{u}_2 \begin{Bmatrix} \dfrac{-H}{Lx_2^{\,2}}\left(-2x_1+L\right)\sin\left(\dfrac{2m\pi x_1}{L}\right) \\ \dfrac{\left(-x_2+H\right)}{L^2x_2}\left[m\pi\left(-2x_1+L\right)\cos\left(\dfrac{2m\pi x_1}{L}\right)-L\sin\left(\dfrac{2m\pi x_1}{L}\right)\right] \end{Bmatrix} \tag{2.21}$$

for $(x_1, x_2) \in D_3$ and $\varepsilon_{11} = 0$ for $(x_1, x_2) \in V$.

Consider the triangular element e, of which one of the nodes locates at the atom a shown in Figure 2.13. The element e occupies the volume Ω_e through triangular meshing in the atomic region. The interatomic potential energy density of within Ω_e can be estimated by the two-dimensional linear interpolation of the nodal potential energy density of atoms for the domain. Then, this element can be used to determine the

interatomic potential energy density field between the values defined at the nodes, which are located at atomic sites. Therefore, based on Equation (2.12), the kinematics of the discrete atomistics in real fields related to $\sigma_{ij}^{(\alpha)}$ and the continuum perturbations in virtual fields corresponding to $\delta\varepsilon_{ij}$ are combined to be used in the further analysis of principle of virtual work for grain boundary traction-probing projection.

2.3 Field description of grain boundary tractions through equivalence between discrete and continuum energetics

In Section 2.2, the new algorithm of adjusting atomic stresses to satisfy the linear momentum balance law in continuum the most and the new scheme to combine the kinematics of the discrete atomistics in real fields and the continuum perturbations in virtual fields for calculating variation of interatomic potential energy density of domain V due to the perturbations on S are presented. Here, we apply these two techniques to develop the interior field projection method to field descriptions of grain boundary tractions. As stated before, central to this projection method is the principle of virtual work

$$\int_V \delta\boldsymbol{\varepsilon} : \boldsymbol{\sigma}\, dv = \int_S \delta\mathbf{u} \cdot \mathbf{t}\, \mathrm{d}s = \Delta\Phi \tag{2.22}$$

for a static system without body forces. Here $\delta\boldsymbol{\varepsilon}$ is the virtual strain work-conjugate to the Cauchy stress $\boldsymbol{\sigma}$, $\delta\mathbf{u}$ denotes an admissible virtual displacement field, $\mathbf{t}$ represents the boundary traction and $\Delta\Phi$ is the variation of the total interatomic potential energy. Through Equation (2.12) and Equation (2.22), we provide a unique way of formulating

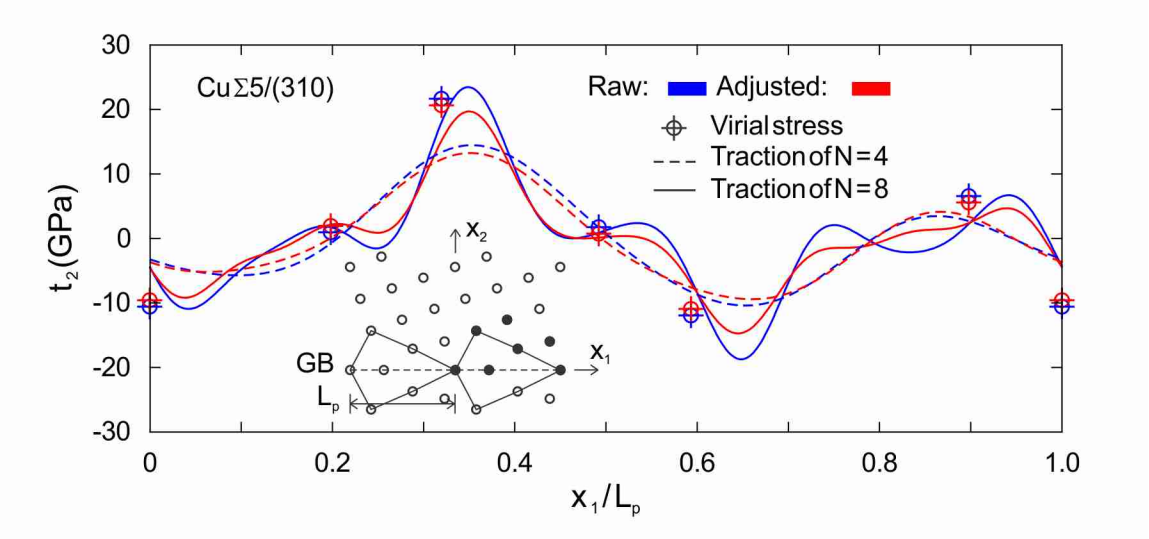

Figure 2.15 Comparison of the virial stresses and the projected normal traction distribution of Cu ∑5/(310) grain boundaries.

the equivalence between discrete and continuum energetics for atomic systems. In Figure 2.14, the configuration of Cu ∑5/(310) grain boundaries without far field loadings through molecular statics is shown. The tractions of the interface located along the grain boundary $x_2 = 0$ are going to be determined. These tractions are expressed in terms of the Fourier series

$$t(x_1,0) = \sum_{n=0}^{\infty} A_n \cos\frac{2n\pi x_1}{L_p} + \sum_{n=1}^{\infty} B_n \sin\frac{2n\pi x_1}{L_p} \tag{2.23}$$

where L_P is the periodic length of the grain boundary, n is the wave number, and A_n and B_n are the Fourier coefficients to be determined. Then, by substituting Equation (2.13) and (2.23) in Equation (2.22), we obtain

$$A_n = \frac{2\Delta\Phi_n^1}{L} \quad \text{or} \quad B_n = \frac{2\Delta\Phi_n^2}{L} \tag{2.24}$$

where $\Delta\Phi_n^{1,2}$ represent the total interatomic potential energy variation caused by $\delta\mathbf{u}(x_1, x_2)$ composed by the $F(x_1)$ of cosine and sine basis functions respectively in Equation (2.13).

The noromal tractions along the ∑5/(310) symmetric tilt grain boundary of pure copper are extracted by using the interior field projection scheme and shown in Figure 2.15. Our numerical experiments show that the projected grain boundary traction distribution is independent of the height and width of the domain *V*, and rapidly converges after about $N = 8$ Fourier terms, which demonstrates the overall stability of the numerical scheme. These projected tractions satisfy force balance, i.e. zero net vertical forces in the absence of far field loading, unlike the virial stresses through the linear and spline interpolations. Compared to the projected traction based on the original virial stresses of atoms in *V*, the projected traction through the adjusted virial stresses for satisfying linear momentum balance the most distributes more smoothly along the grain boundary. In addition, at the discrete atomic sites, the projected stresses are in good agreement with the virial stress values. However, the projected tractions along the grain boundary are oscillating, and one cannot readily infer the stress distributions between atoms by simple interpolation of the virial stresses. Within each grain boundary period, our projected stresses for Cu ∑5/(310) grain boundary show a compressive peak stress of −15 GPa compared to the virial stress prediction of −11 GPa. The periodic compressive pinching stress is responsible for crack trapping and grain boundary strengthening during intergranular fracture (Cheng *et al.*, 2010), and cannot be captured by direct evaluation of the virial stresses at the atomic sites along the grain boundary.

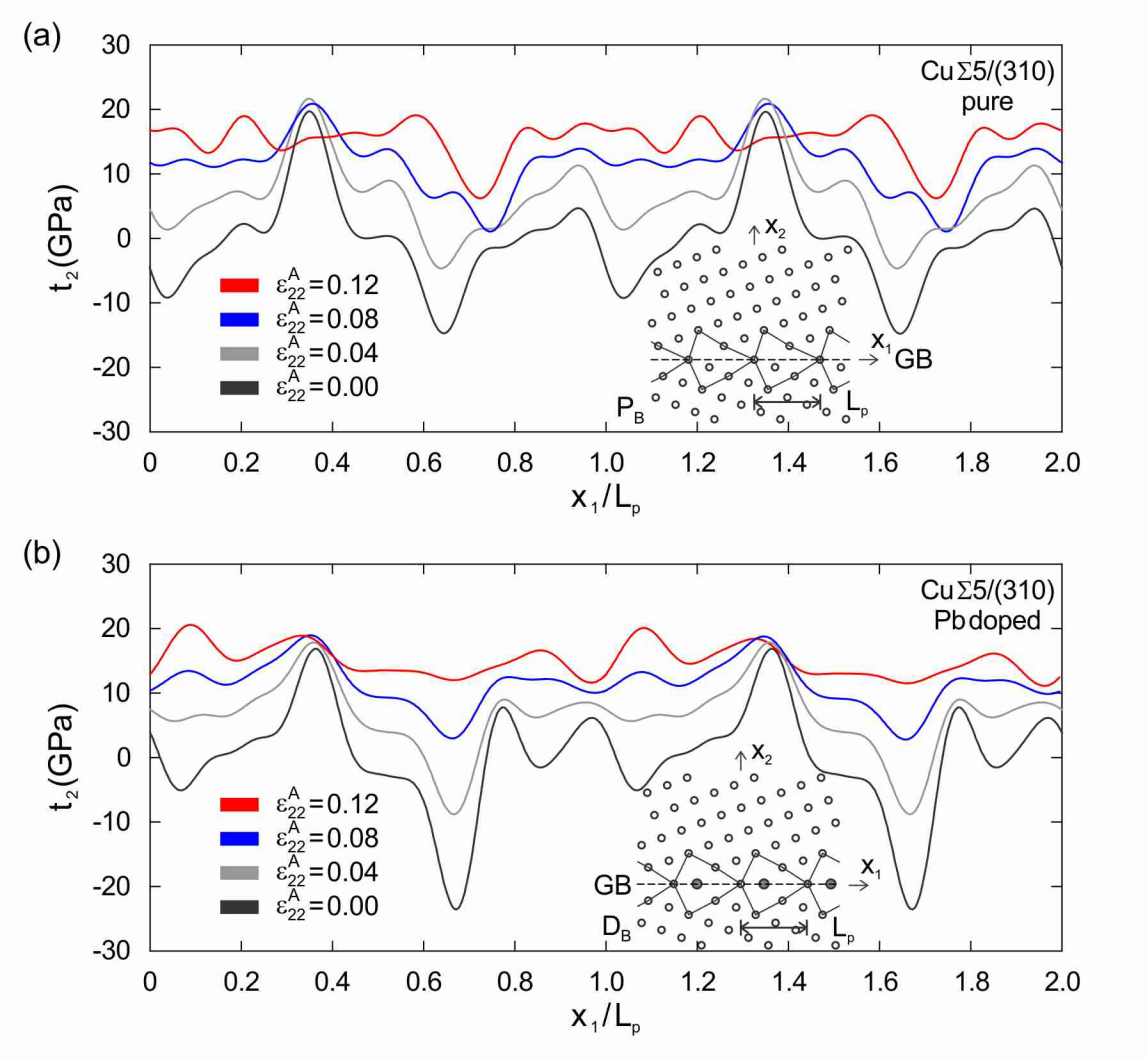

Figure 2.16 Normal traction of pure (a) and Pb doped (b) Cu ∑5/(310) grain boundaries under different uniaxial applied strains.

Now, we use the interior field projection method to investigate the phenomena of grain boundary embrittlement. In general, dopant atoms, which are much larger than the bulk atoms, segregate the grain boundary, where they substitute the host atoms at periodic boundary sites with the largest space as represented the locations of atoms drawn in gray colors in the insets of Figure 2.2 and Figure 2.3. Molecular statics simulations

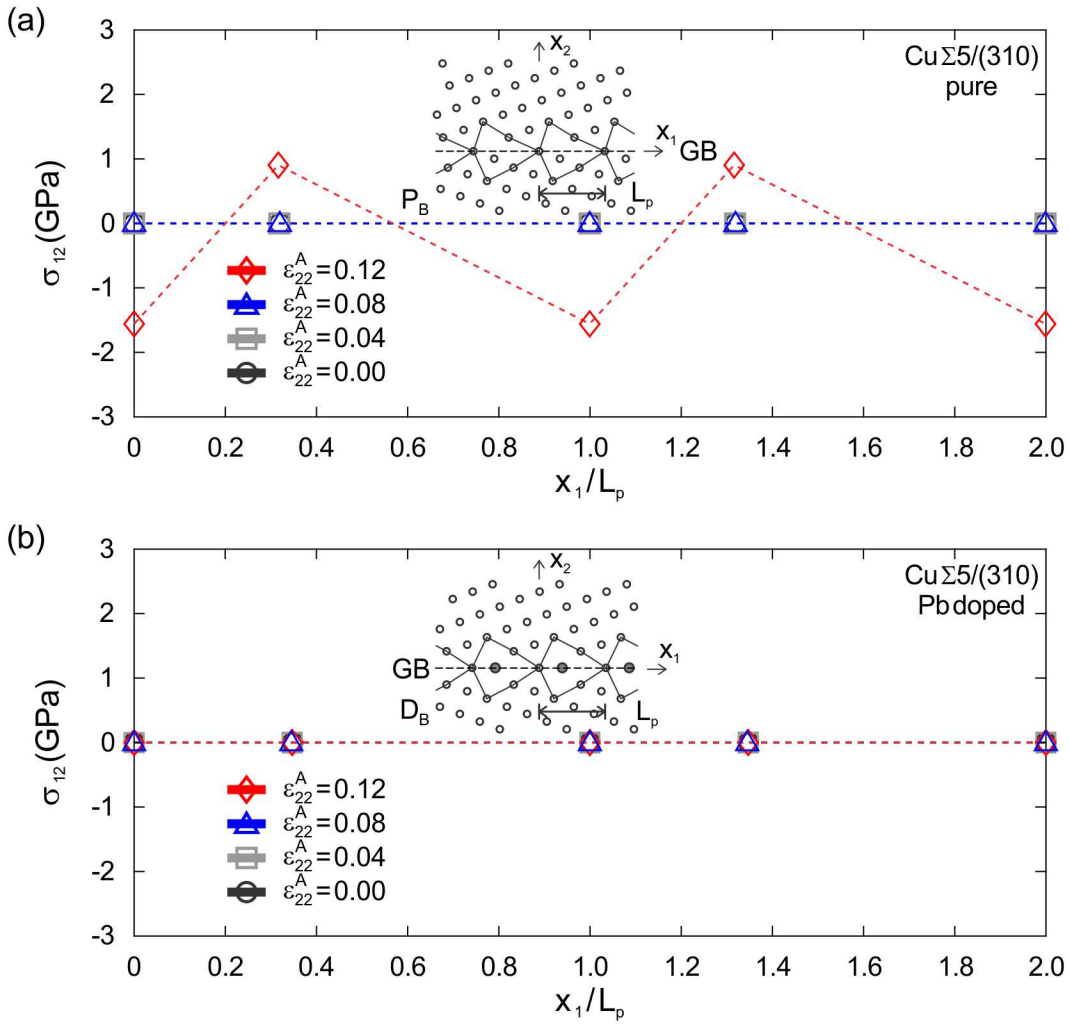

Figure 2.17 Shear stresses of pure (a) and Pb doped (b) Cu ∑5/(310) grain boundaries under different uniaxial applied strains.

based on the conjugate gradient method confirm that the minimum energy configuration consists of Pb dopant atoms which substitute pre-existing Cu atoms along the grain boundary at the high tensile stress site within each grain boundary period. These energetically preferred sites correspond to where the maximum tensile traction exists in each grain boundary period and to where the host bonds are highly strained.

Figure 2.16(a) and (b) show the evolutions of cohesive normal tractions under uniaxial straining for the pure and Pb doped Cu ∑5/(310) grain boundaries respectively. For the pure Cu ∑5/(310), it is found that under far-field uniaxial strains up to 0.08, the normal cohesive traction distribution along the grain boundary evolves in proportion to the applied load, which represents that the atomic configuration of the grain boundary is nearly unchanged. It must be noted that the normal traction magnitudes from their baselines, which are equal to the current far-field loadings, to the peaks of compressive tractions are decreased when the far-field loadings increases. The explanation for this phenomenon is that the grain boundary atomic displacement of minute amounts induced by the far-field loadings eases the incompatibility between the two adjacent grains. Moreover, as the far-field uniaxial strains are below 0.08, the grain boundary shear stresses are all zero shown in Figure 2.17(a), indicating that the atomic configurations near grain boundaries retain perfectly symmetric in the early stages of loadings.

To examine the details of atomic deformation distribution near the grain boundaries, two-dimensional atomic strains are further calculated based on molecular statics simulations. Consider two adjacent grains of perfect Cu crystals with tilt angle of 36.87 degrees and the twinning plane of {310} to form coincidence site lattices of $\sum = 5$. By taking such lattice configuration as the reference configuration of the bicrystal containing Cu ∑5/(310) grain boundaries obtained from full energy relaxation in molecular statics calculation, the discrete displacement information at atomic sites of the current configuration is determined. Then, the averages of the components of the displacement gradient tensor within the atomic voronoi cell of atom α can be calculated

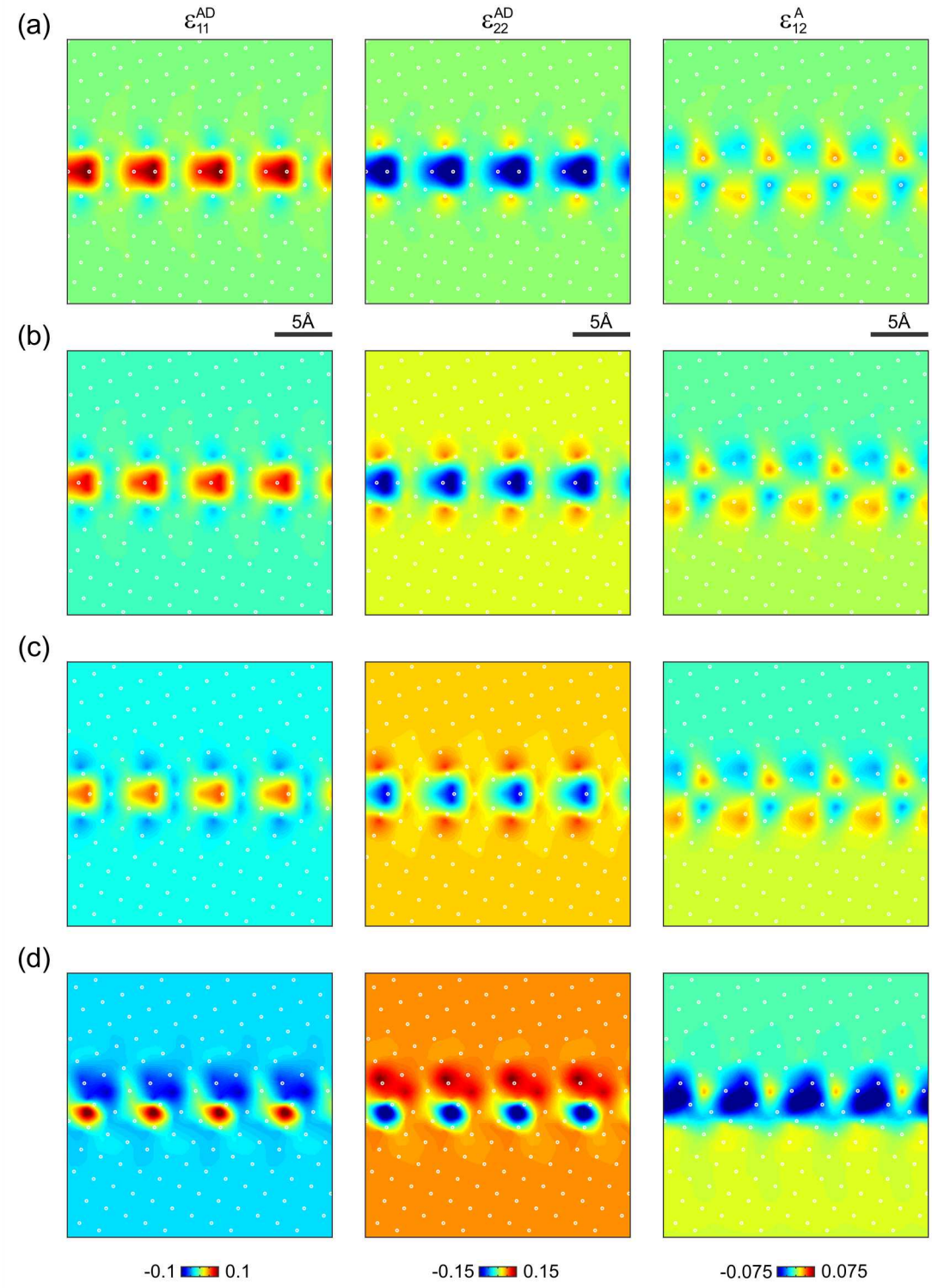

Figure 2.18 Distributions of atomic deviatoric Almansi strains of pure Cu ∑5/(310) grain boundaries under uniaxial applied strains of 0.00 (a), 0.04 (b), 0.08 (c) and 0.12 (d).

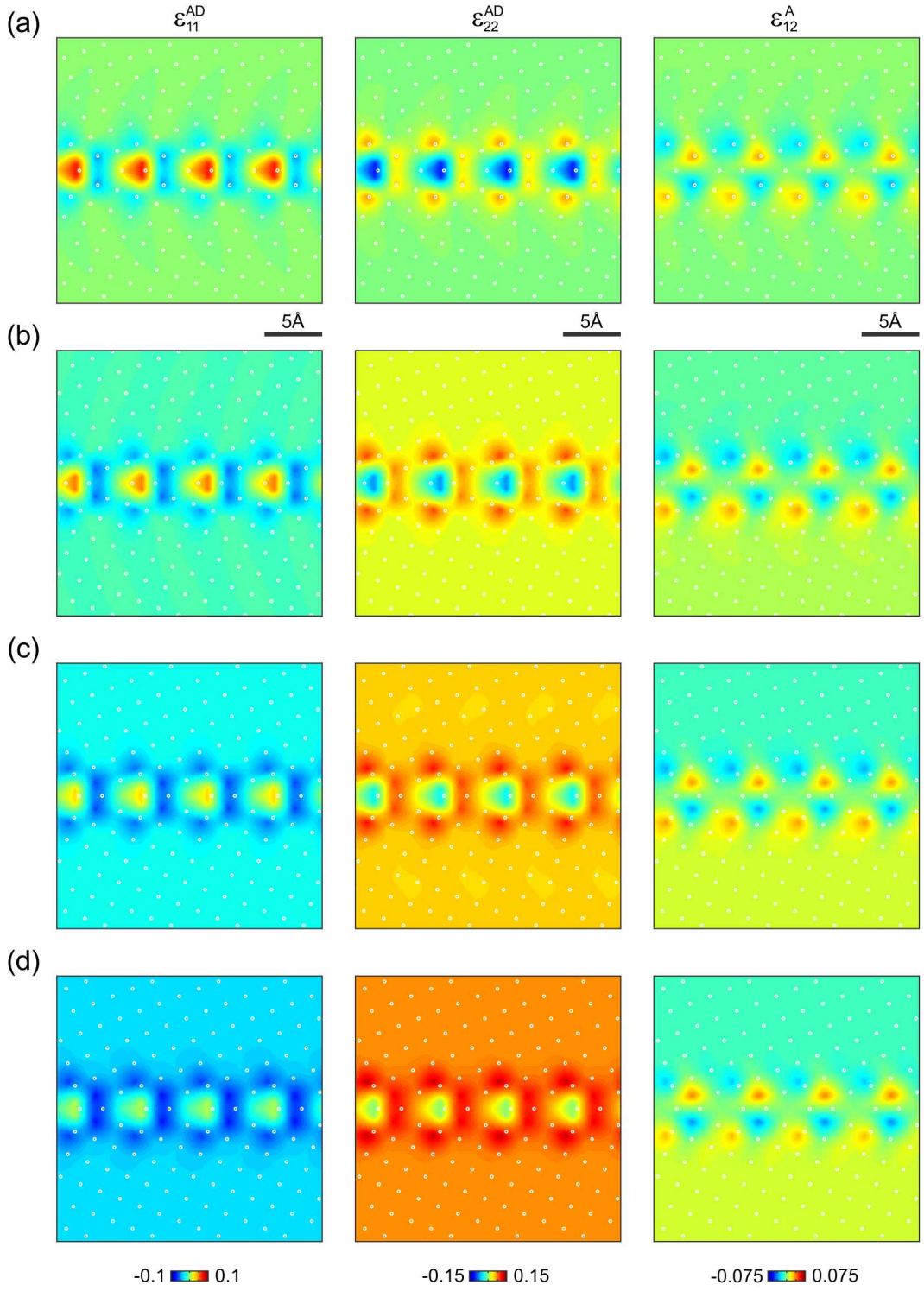

Figure 2.19 Distributions of atomic deviatoric Almansi strains of Pb doped Cu ∑5/(310) grain boundaries under uniaxial applied strains of 0.00 (a), 0.04 (b), 0.08 (c) and 0.12 (d).

as

$$\overline{u}_{i,j}^{(\alpha)} = \frac{1}{A^{(\alpha)}} \int_{\Omega^{(\alpha)}} u_{i,j}\, dA = \frac{1}{A^{(\alpha)}} \int_{\partial\Omega^{(\alpha)}} u_i n_j\, ds\,, \tag{2.25}$$

where $A^{(\alpha)}$ is the area of the voronoi cell Ω of atom α and n_j the j-th component of normal vector along the boundary of Ω. Then, the averages of Cartesian components of deformation gradient tensor at the site of atom α can be computed as

$$\overline{F}_{i,j}^{(\alpha)} = \delta_{ij} + \overline{u}_{i,j}^{(\alpha)}\,. \tag{2.26}$$

The Almansi strain tensor at atom α of the current configuration is thus estimated as

$$\overline{\mathbf{E}}^{A(\alpha)} = \frac{1}{2}\left[\mathbf{I} - \left(\overline{\mathbf{F}}\ \overline{\mathbf{F}}^{T}\right)^{-1}\right]. \tag{2.27}$$

Consequently, two-dimensional strain distributions near the grain boundaries are approximately determined through interpolation between atomic strains. To have a close look at the atomic distortion distributions induced by far-field straining, deviatoric Almansi strains related to volume-preserving deformation are presented. The distributions of atomic deviatoric Almansi strains of pure Cu ∑5/(310) grain boundaries under uniaxial applied strains are shown in Figure 2.18. These strain distributions corresponding to far-field strains below 0.08 (Figure 2.18(a), (b) and (c)) make it clear that the atomic configurations are still symmetric when sustaining external loadings. However, at higher strains such as 0.12, the shape of the normal traction profiles changes dramatically shown in Figure 2.16(a), suggesting that atomic rearrangement of the grain boundary has occurred. At this stage, the atomic instabilities of grain boundaries break the symmetry of the bicrystal observed in Figure 2.18(d). The important point to note is that grain boundary shear traction fluctuation is triggered once asymmetric atomic rearrangement happens.

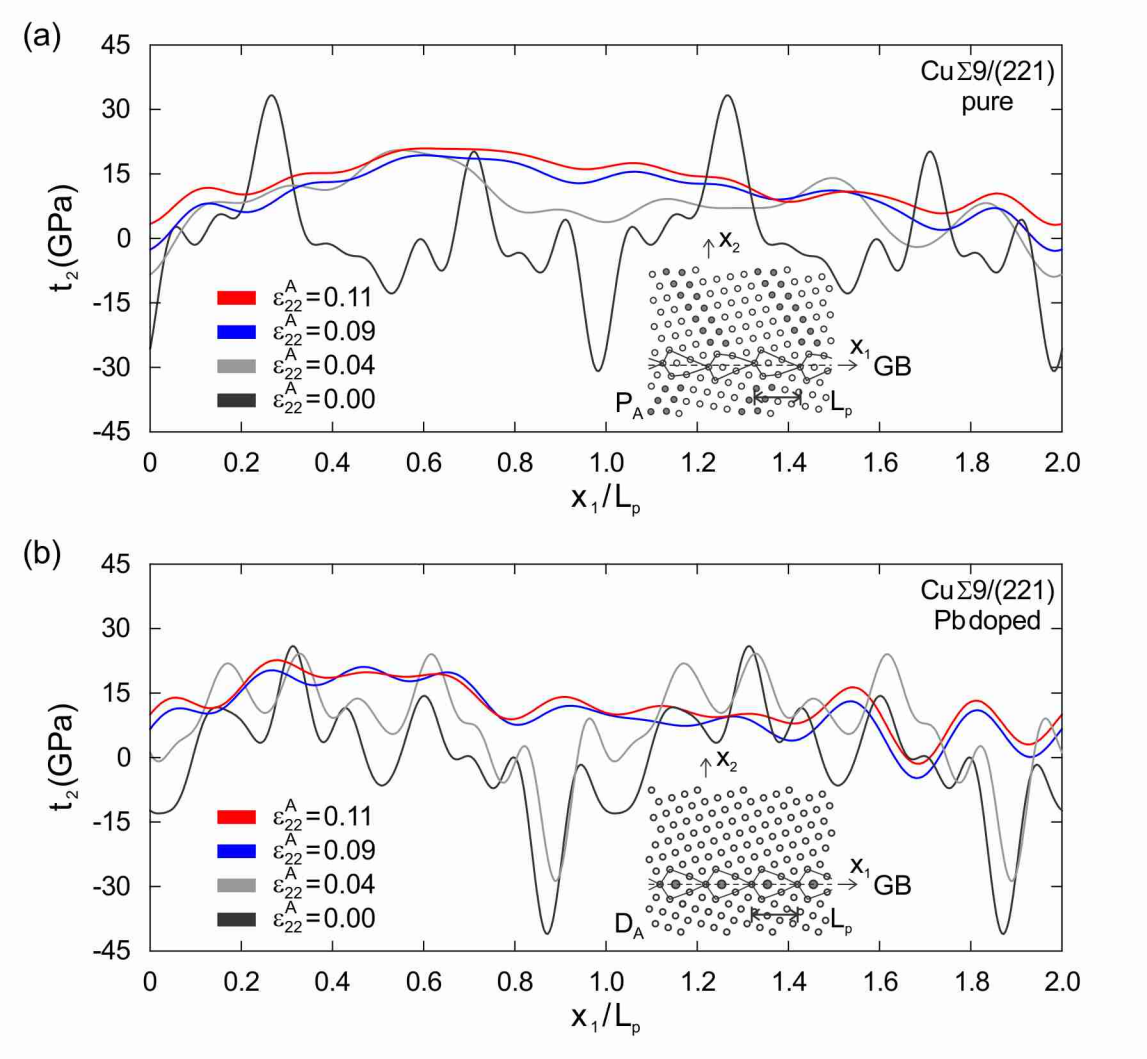

Figure 2.20 Normal tractions of pure (a) and Pb doped (b) Cu ∑9/(221) grain boundaries under different uniaxial applied strains.

For Pb doped Cu ∑5/(310) grain boundaries, unlike the pure Cu ∑5/(310), neither asymmetric atomic configuration change nor dislocation emission is observed (Figure 2.19) even at high strains as 0.12, which is close to the failure strain of the material. Consequently, there is no grain boundary shear stress (Figure 2.17(b)) during the far-field uniaxial straining. In addition, the dopants Pb maintain tension peaks of GB traction

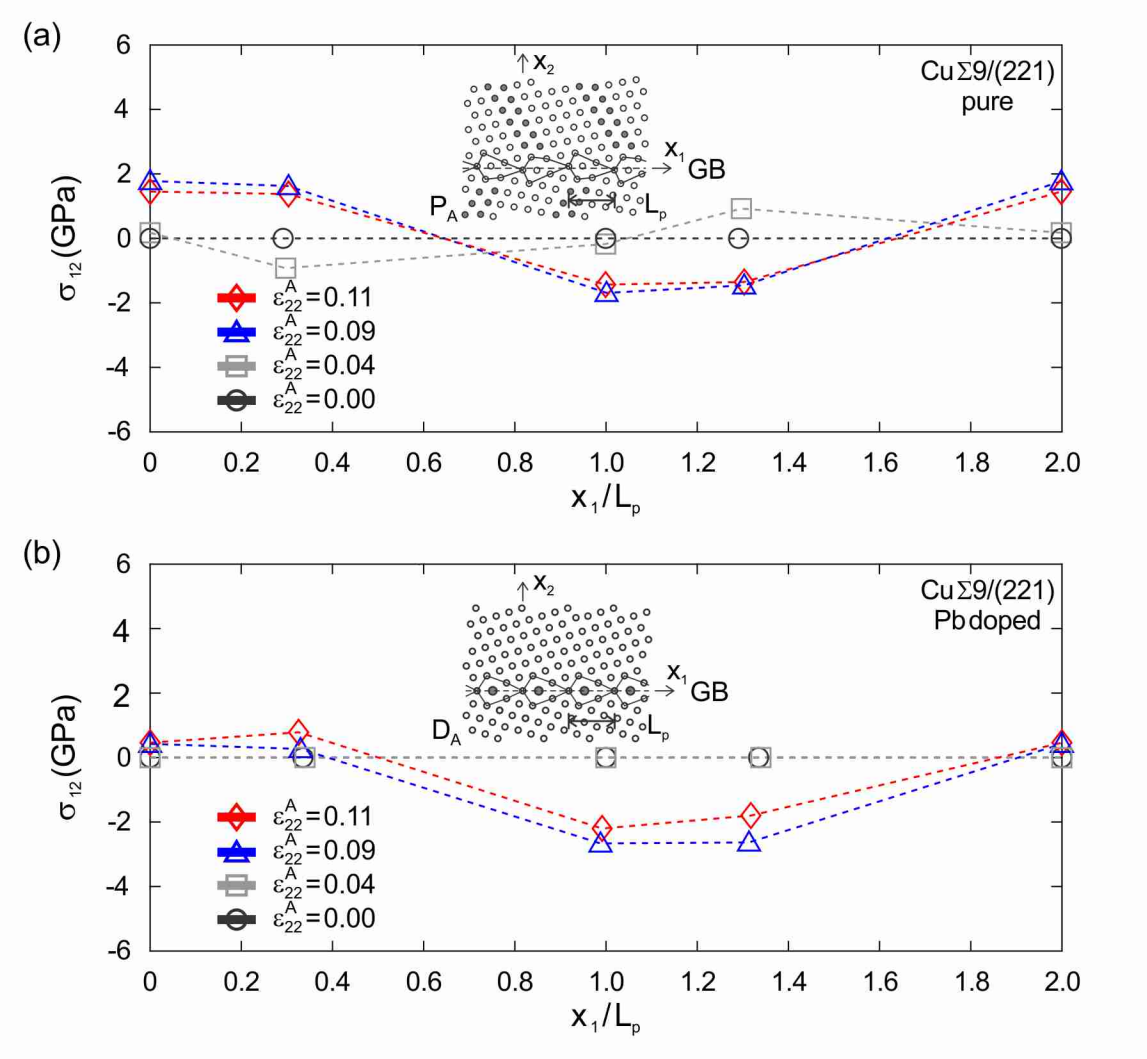

Figure 2.21 Shear stresses of pure (a) and Pb doped (b) Cu ∑9/(221) grain boundaries under different uniaxial applied strains.

fluctuation shown in Figure 2.16(b) as the loading increases. It means that such big atoms of dopants suppress cooperative processes of grain boundary layer deformation, such as atomic rearrangement activities.

Figure 2.20(a) and (b) present the variations of cohesive normal tractions under uniaxial straining for the pure and Pb doped Cu ∑9/(221) grain boundaries correspondingly. Similarly, by comparing a bicrystal containing two grains of perfect Cu

crystals with tilt angle of 38.94 degrees and the twinning plane of {221} to form coincidence site lattices of $\sum = 9$ with the atomic configuration including corresponding grain boundaries from full energy relaxation in molecular statics, the two-dimensional atomic strains distributions of pure and Pb doped Cu $\sum$9/(221) grain boundaries are obtained and shown in Figure 2.22 and Figure 2.23 respectively. Compared to the pure Cu $\sum$5/(310) grain boundaries, pure Cu $\sum$9/(221) has more ductile characteristics in which multiple dislocation emissions are observed shown in Figure 2.22. As the strain is 0.04, asymmetric dislocation emission has taken place, which causes the extremely stress reduction at the sites with high tension concentrations of the normal traction fluctuations in each grain boundary period. Therefore, the activities of asymmetric dislocation emission subdue grain boundary separations. Moreover, such asymmetric dislocation emission opens an access to a new strain energy reservoir by triggering grain boundary stress fluctuations in shear shown in Figure 2.21(a).

For Pb doped Cu $\sum$9/(221) grain boundaries, atomic rearrangement makes compression peaks of grain boundary normal traction fluctuation decreased in the early stages of loadings shown in Figure 2.20(b). The Pb dopants which lie on the grain boundaries maintain the symmetric configurations of the bicrystal under the far-field uniaxial strains up to 0.04 shown in Figure 2.23. In addition, such impurity atoms at grain boundaries also maintain tension peaks of grain boundary normal traction fluctuations. It means that the dopant atoms retard cooperative processes of GB layer deformation, such as emissivity of dislocation from grain boundaries. At the later stages of loadings, asymmetric dislocation emission occurs and triggers the grain boundary shear stress

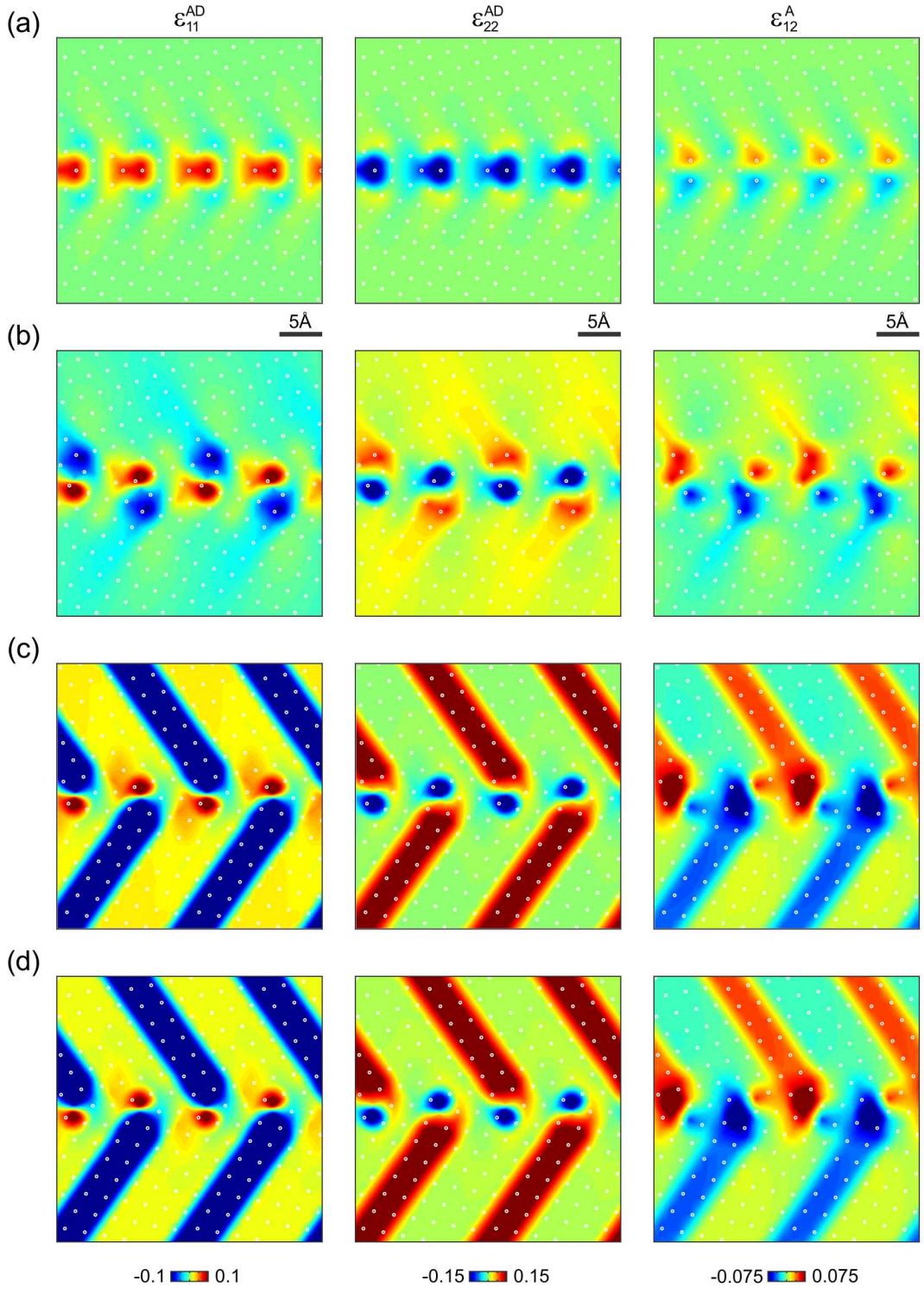

Figure 2.22 Distributions of atomic deviatoric Almansi strains of pure Cu ∑9/(221) grain boundaries under uniaxial applied strains of 0.00 (a), 0.04 (b), 0.09 (c) and 0.11 (d).

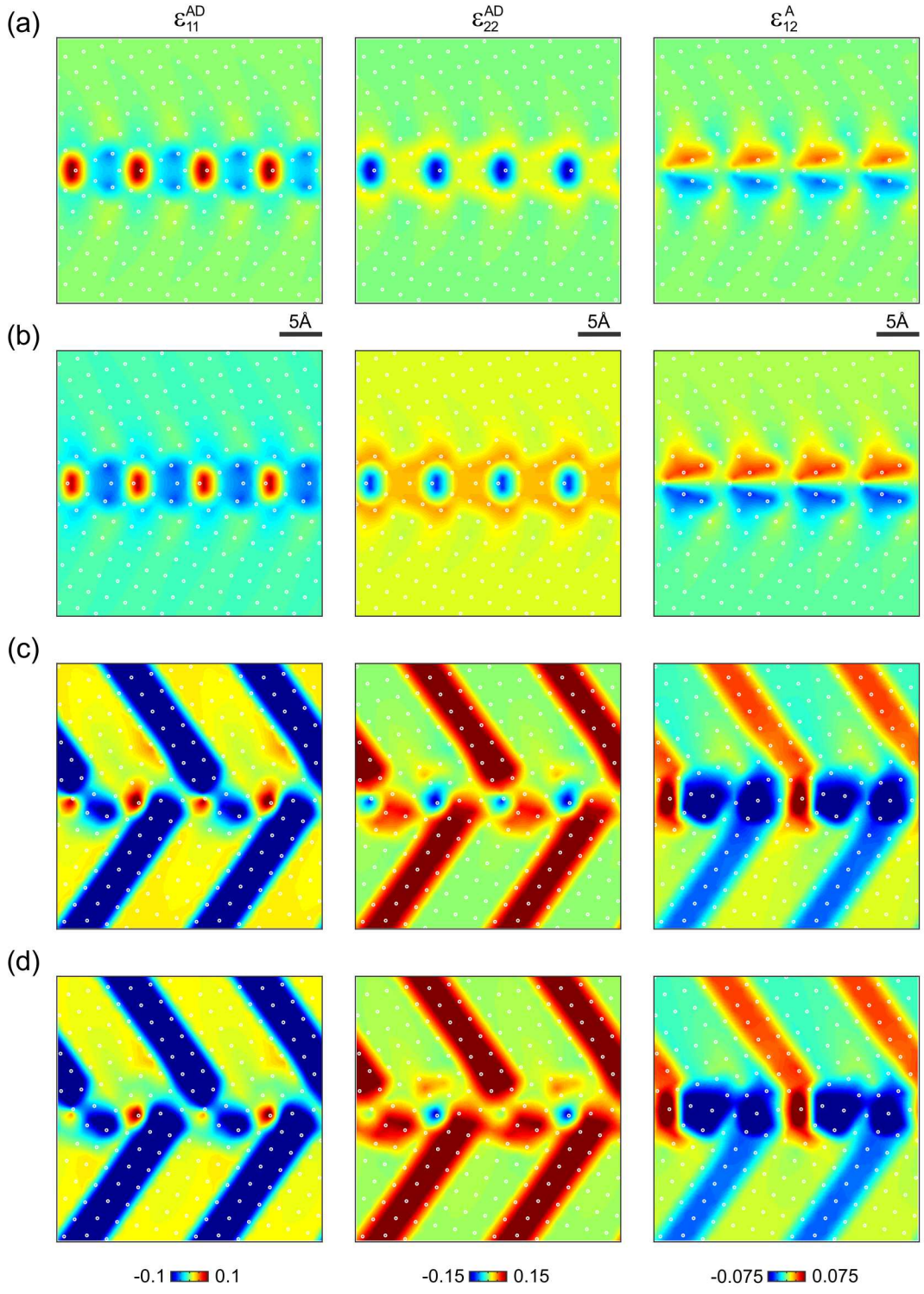

Figure 2.23 Distributions of atomic deviatoric Almansi strains of Pb doped Cu ∑9/(221) grain boundaries under uniaxial applied strains of 0.00 (a), 0.04 (b), 0.09 (c) and 0.11 (d).

fluctuations presented in Figure 2.21(b), providing a new storage source of strain energy. Compared to the pure Cu ∑9/(221) grain boundaries, the grain boundary shear stress fluctuations of Pb doped ∑9 have less oscillations, indicating that the strain energy storage capacity of pure Cu ∑9 is better and thus more ductile than Pb doped Cu ∑9 grain boundaries.

In the study, we provide a novel way of extracting grain boundary traction distributions to investigate the phenomena of grain boundary embrittlement. The evolutions of grain boundary normal tractions under far-field uniaxial straining show that the external loading cannot be directly added to the pre-existing grain boundary residual traction fluctuations. Therefore, the deformation of a grain boundary layer depends on cooperative processes, such as atomic rearrangement activities and dislocation emission from grain boundaries. In summary, from the above analyses, we can recognize that the cooperative-process dependent deformation of the grain boundary layer provides grain-boundary ductility, and that the separation toughness of grain boundaries cannot be gauged by classical Griffith cleavage energy or simply by the local bond strength. It is also found that the degree of symmetry breaking in the dislocation-emission process plays major role in setting the separation toughness of the grain boundary.

Chapter 3. Exterior Field Projection Method

3.1 Bridging between kinematics of discrete atomistics and continuum fields

In Chapter 2, the interior field projection (IFP) method extracts the grain boundary traction from the discrete atomistics information of molecular calculations with a high level of precision. However, in actual experiments, applying perturbation of individual atoms to extract field-projected traction distributions at the grain boundary seems not amenable. In the past decade, several researcher have been devoted to the experimental study of measuring distortions of the atomic configurations caused by grain boundaries by using transmission electron microscopy (TEM) imaging (Duscher *et al.*, 2004; Hytch *et al.*, 2006) and then thrown new light on determining the deformation distributions surrounding atomic defects. Based on the measured atomic displacement at the far field of grain boundaries, we propose an exterior field projection (EFP) method to inversely extract the grain boundary tractions in this chapter.

Figure 3.1 shows the minimum energy configuration of Cu near $\sum 5/(310)$ grain boundaries through molecular statics calculations. The displacement distribution in discrete depicted in Figure 3.1 can be obtained by comparing the atomic configurations in a perfect crystal of Cu to mimic experimental high-resolution measurement. Moreover, in

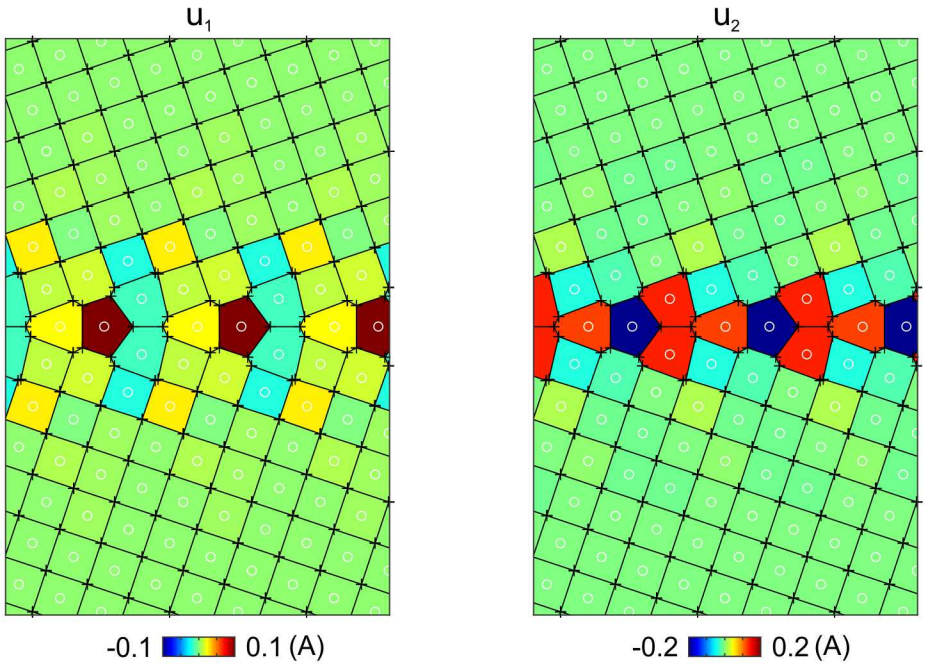

Figure 3.1 Discrete information of the atomic displacement due to the Cu ∑5/(310) grain boundary formation.

order to accurately collect the atomic distortion distribution at the far field, we need to find a smooth field which is the closet to measured data among possible equilibrium fields. In this study, we apply the equilibrium field smoothing (EFS) method, which was developed by Hong *et al.* 2009 (Hong *et al.*, 2009), to the measured information in the remote region at some distance away from the grain boundary. Through EFS, the smooth field from the measurement data not only encloses the discrete nature of atomistics but also satisfies the governing field equations in continuum with minimum measurement errors, which are essential for inverse problems in engineering mechanics. That is to say that EFS provides a way of bridging between kinematics of discrete atomistics and continuum fields. Figure 3.2 shows the displacement distribution of Cu near ∑5/(310)

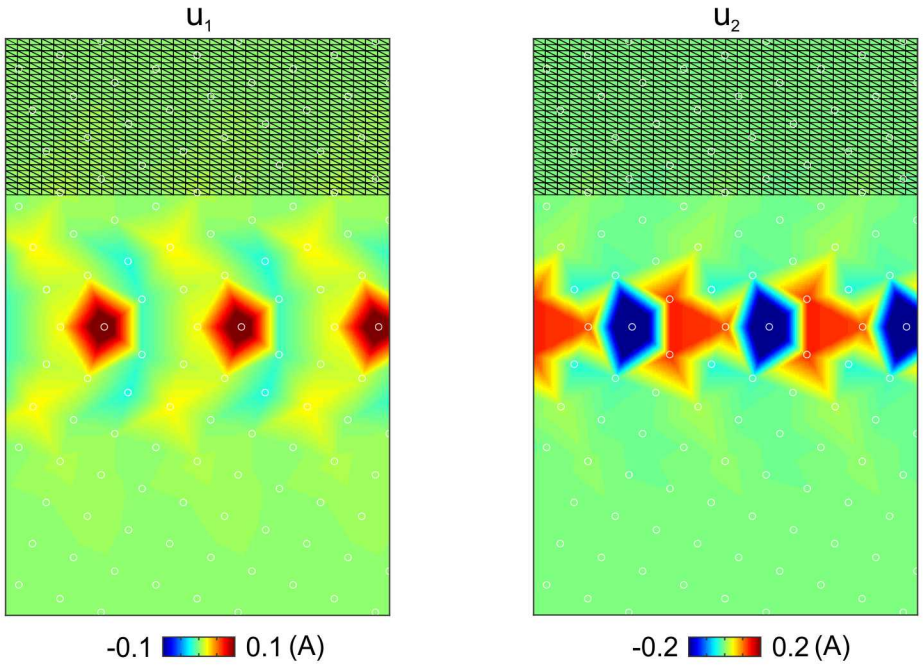

Figure 3.2 Atomic displacement of Cu ∑5/(310) grain boundaries through direct linear interpolations of molecular statics information.

grain boundaries through two-dimensional linear interpolation of the raw measurement data of atomic sites from the simulated measurement introduced above. In addition, at some distance from the grain boundaries, finite element meshes are put in the remote region with linear elastic deformation to generate the degrees of freedom for finding the equilibrium smooth field representative to the measurement information. The equilibrium field smoothing method is introduced briefly here as follows. The simplified form of the equilibrium smooth displacement is

$$\mathbf{u} = \left(\mathbf{I} - \mathbf{K}^T \left(\mathbf{K}\mathbf{K}^T \right)^{-1} \mathbf{K} \right) \tilde{\mathbf{u}} , \tag{3.1}$$

where $\mathbf{u}$ and $\tilde{\mathbf{u}}$ are the equilibrium smooth and the measured displacement vectors respectively, $\mathbf{I}$ is the identity matrix and $\mathbf{K} = \begin{bmatrix} \mathbf{K}_{12} & \mathbf{K}_{22} \end{bmatrix}$ for the global equilibrium equation for the material in the remote region as

$$\begin{bmatrix} \mathbf{K}_{11} & \mathbf{K}_{12}^T \\ \mathbf{K}_{12} & \mathbf{K}_{22} \end{bmatrix} \mathbf{u} = \mathbf{p}, \tag{3.2}$$

where $\mathbf{p}$ is the vectors of nodal forces. This equilibrium equation can be expressed further as

$$\begin{bmatrix} \mathbf{K}_{11} & \mathbf{K}_{12}^T \\ \mathbf{K}_{12} & \mathbf{K}_{22} \end{bmatrix} \begin{Bmatrix} u_b \\ u_i \end{Bmatrix} = \begin{Bmatrix} p_b \\ 0 \end{Bmatrix}, \tag{3.3}$$

where the subscripts b and i denote boundary and internal nodes respectively.

To apply EFS for the simulated measurement, triangular meshes over 150×25 sampling grid are constructed within the Cu remote domain of $-7.452\,\text{Å} \le x_1 \le 6.840\,\text{Å}$ and $5.016\,\text{Å} \le x_2 \le 11.880\,\text{Å}$ near the grain boundaries of $\sum 5/(310)$ presented in Figure 3.2 for determining the equilibrium smooth displacement fields $\mathbf{u}$ from the measurement data $\tilde{\mathbf{u}}$. In Figure 3.3, the comparisons between the measured displacement distributions and the equilibrium smooth displacement fields of horizontal and vertical components are shown respectively. Compared to the measured displacement, the equilibrium smooth displacement fields not only have smoother distributions in the far region but also contain the zones with major deformation in the orientations which are closer to the possible easy-glide directions of this bicrystal. Therefore, through the equilibrium field smoothing method, the most representative displacement fields which satisfy equilibrium equations in continuum can be revealed based on the atomic deformation information. Along the

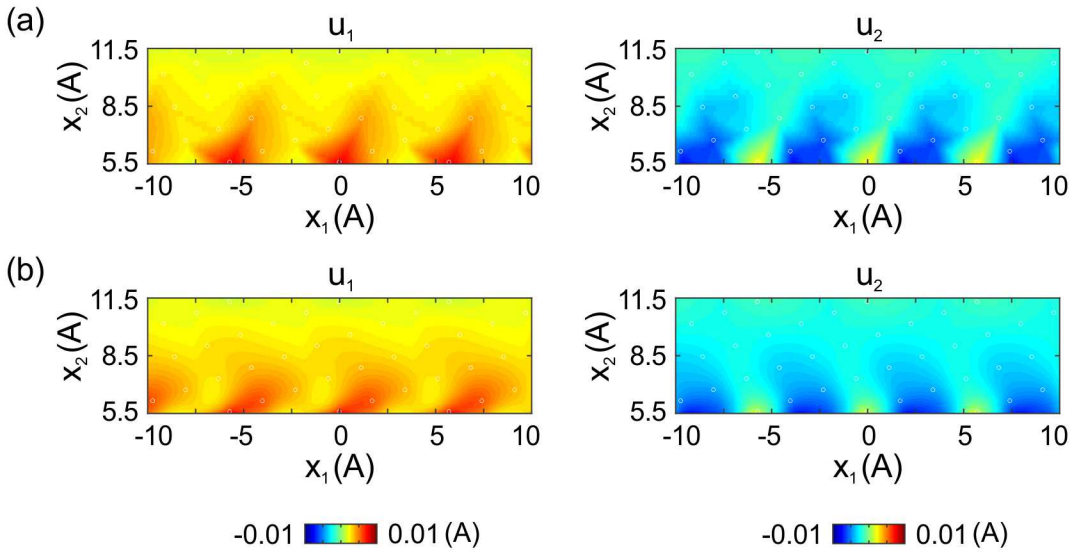

Figure 3.3 Atomic displacement of the remote region from Cu ∑5/(310) grain boundaries. (a) Measured displacement distributions from the simulated experiment through molecular statics (b) Smooth displacement fields through equilibrium field smoothing.

contour $x_2 = 6\,\mathring{\mathrm{A}}$ in the far region of linear elastic deformations, the representative displacement fields based on measured deformations through EFS are then the input information for extracting the grain boundary tractions by using the exterior field projection method introduced in the next section.

3.2 Conservation of interaction J integrals around grain boundaries

The core of the exterior field projection method is the conservation of interaction J integrals (Rice, 1968; Knowles & Sternberg, 1972; Budiansky & Rice, 1973; Chen & Shield, 1977) for solving the inverse problem of extracting grain boundary tractions from the measured displacement information in the far field. In general, the Maxwell-Betti's

reciprocal theorem is commonly applied for finding out stress and displacement fields of the region of interest in linearly elastic boundary value problems (Barber & Sturla, 1992). Furthermore, for materials of intrinsic nonlinearity in nanoscale, the reciprocal theorem needs to be extended to incorporate the material nonlinearity by including reciprocity gaps associated with the nonlinear deformations (Bonnet & Constantinescu, 2005; Chew, 2013). Therefore, the atomic slips near grain boundaries along the easy-gliding direction associated with nonlinear deformations of materials as the reciprocity gap in the Maxwell-Betti's reciprocal theorem must be considered to maintain the conservation of interaction J integrals around the interface of the solid. Next, the exterior field projection method of grain boundaries considering the slips between atomic layers near grain boundaries is derived in the following contents.

Figure 3.4 shows the atomic configuration of the domain *R* near Cu ∑5/(310) grain boundaries and the closed contour surrounding *R*. The contour includes the grain boundary Γ_1, the paths of Γ_2 and Γ_4 with periodic boundary conditions, the far field Γ_3 containing the measured displacement information and Γ_5 along atomic slip path. For the domain *R* with two independent elastic fields *S* and $\hat{S}$, the interaction J integral $J_\Gamma^{\text{int}}[S,\hat{S}]$ containing a reciprocity gap between the two elastic fields $S[\boldsymbol{\sigma},\mathbf{u}]$ and $\hat{S}[\hat{\boldsymbol{\sigma}},\hat{\mathbf{u}}]$ along the closed contour Γ is defined as

$$J_\Gamma^{\text{int}}\left[S,\hat{S}\right]=\oint_\Gamma\left[\left(\mathbf{e}_1\cdot\mathbf{n}\right)\left(\boldsymbol{\sigma}:\nabla\hat{\mathbf{u}}\right)-\left(\mathbf{e}_1\cdot\nabla\hat{\mathbf{u}}\right)\cdot\boldsymbol{\sigma}\cdot\mathbf{n}-\left(\mathbf{e}_1\cdot\nabla\mathbf{u}\right)\cdot\hat{\boldsymbol{\sigma}}\cdot\mathbf{n}\right]ds\,, \tag{3.4}$$

where $\mathbf{n}$ is the outward unit normal of the integration path, $\boldsymbol{\sigma}$ is the elastic stress field, $\mathbf{u}$ is the elastic displacement field, $\hat{\boldsymbol{\sigma}}$ is the auxiliary elastic stress field, and $\hat{\mathbf{u}}$ is the auxiliary elastic displacement field. Along the path Γ_5, the slip of atomic layers is

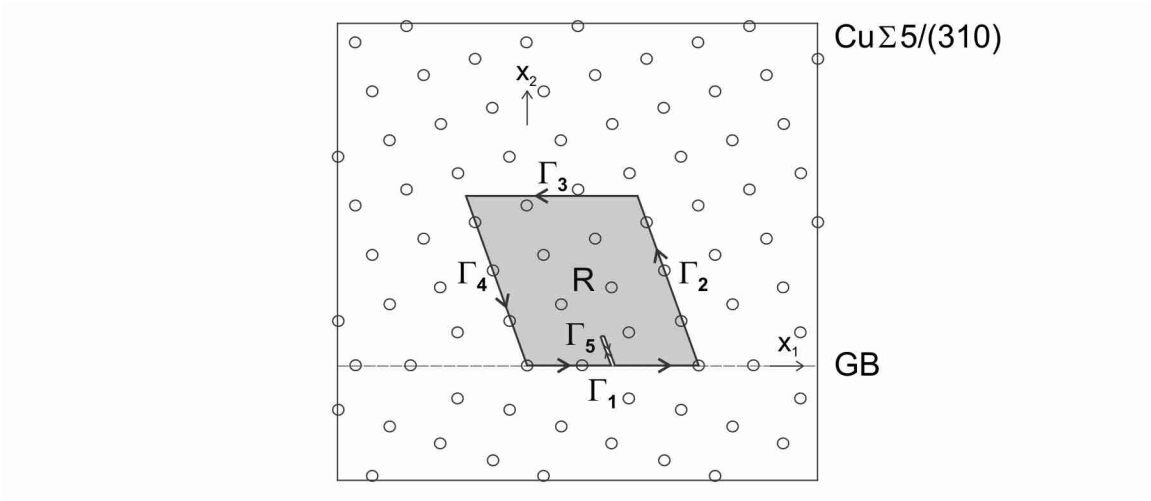

Figure 3.4 Exterior field projection scheme using the conservation of interaction J integrals to extract tractions along path Γ_1 and slip distributions along Γ_5 based on far-field displacement information along Γ_3 of the bicrystals containing the symmetric tilt Cu ∑5/(310) grain boundary.

modeled by cohesive zone laws of known traction-separation relations calibrated by the generalized stacking fault energies of Cu (Lu *et al.*, 2000; Gao & Bower, 2004). In addition, it is assumed that there is no singularity at the crack tip of the slip path. Therefore, $J_{\Gamma}^{\text{int}}\left[S,\hat{S}\right]$ can be further reduced as

$$J_{\Gamma}^{\text{int}}\left[S,\hat{S}\right]=\oint_{\Gamma}\left(\sigma_{\alpha\beta}\hat{u}_{\alpha,\beta}n_1-\sigma_{\alpha\beta}\hat{u}_{\beta,1}n_{\alpha}-\hat{\sigma}_{\alpha\beta}u_{\beta,1}n_{\alpha}\right)ds=0\,. \tag{3.5}$$

Because of the periodic structure of domain *R*,

$$J_{\Gamma_2}^{\text{int}}+J_{\Gamma_4}^{\text{int}}=0\,. \tag{3.6}$$

Along the atomic slip path Γ_5,

$$J_{\Gamma_5}^{\text{int}}=\int_{\Gamma_5}-t_s\left[\!\left[\hat{u}_{s,\xi}\right]\!\right]-\hat{t}_s\left[\!\left[u_{s,\xi}\right]\!\right]d\xi\,, \tag{3.7}$$

where t_s and $[\![u_{s,\xi}]\!]$ are the shear traction and slip gradient of the elastic fields S respectively and $\hat{t}_s$ and $[\![\hat{u}_{s,\xi}]\!]$ are the shear traction and slip gradient of the elastic fields $\hat{S}$ respectively. Along the path along the grain boundary Γ_1,

$$J_{\Gamma_1}^{\text{int}} = \int_{\Gamma_1} \left(-t_\alpha \hat{u}_{\alpha,1} - \hat{t}_\alpha u_{\alpha,1} \right) dx_1 \tag{3.8}$$

where t_α and $u_{\alpha,1}$ are the traction, which are the unknown grain boundary traction, and displacement gradient of the elastic fields S correspondingly; $\hat{t}_\alpha$ and $\hat{u}_{\alpha,1}$ are the traction and displacement gradient of the elastic fields $\hat{S}$ correspondingly. Therefore, based on the conservation of interaction J integrals written in Equation (3.5), the measured far-field deformation and the interfacial tractions can be therefore related.

3.3 Traction-probing projection and finite element modeling of grain boundaries

In Section 3.2, the grain boundary traction t_α along Γ_1 and the slip gradient $[\![u_{s,\xi}]\!]$ along Γ_5 of the physical elastic fields S are the unknowns and can be assumed as

$$t_2(x_1) = \sum_{n=0}^{\infty} A_n \cos\frac{2n\pi x_1}{L_p} + \sum_{n=1}^{\infty} B_n \sin\frac{2n\pi x_1}{L_p} \tag{3.9}$$

and

$$[\![u_s]\!] = \sum_{a=1}^{n} N^a(\xi) s^a \tag{3.10}$$

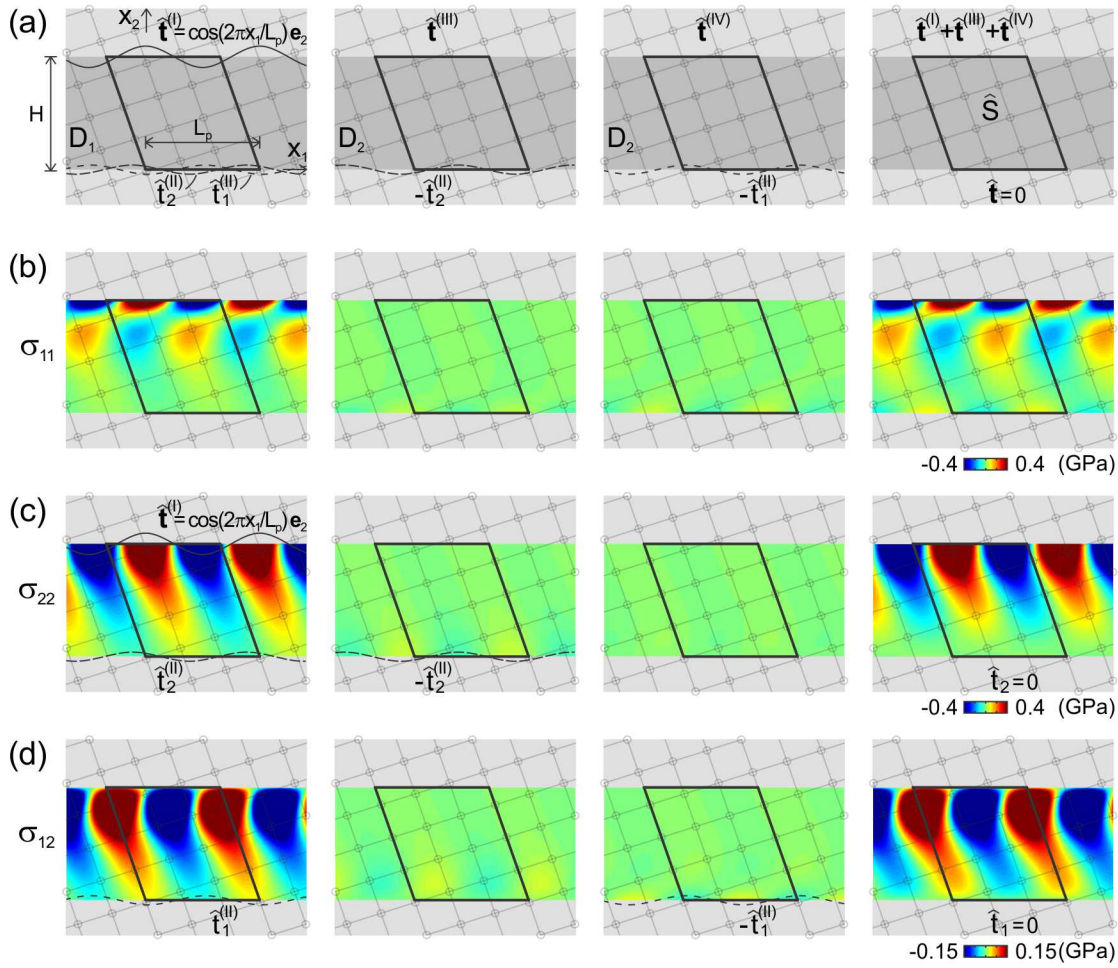

Figure 3.5 Construction of the auxiliary fields for probing the traction distributions of pure Cu ∑5/(310) grain boundaries.

where L_p is the periodic length of the grain boundary, n the wave number, and A_n and B_n the Fourier coefficients, ξ the coordinates of an arbitrary point along Γ_5, $N^a(\xi)$ the linear interpolation function over the nodal values, and s^a the slip value at node a along Γ_5. To solve these unknowns inversely by using the known measured information along Γ_3, a special linear elastic field $\hat{S}$ called auxiliary fields has to be designed to satisfy

$$\hat{\sigma}_{2\alpha} = 0 \qquad \text{along } \Gamma_1 \tag{3.11}$$

$$\hat{u}_{\alpha,1} \neq 0 \qquad \text{along } \Gamma_1 \tag{3.12}$$

and

$$[\![\hat{u}_s]\!] = 0 \qquad \text{along } \Gamma_5 \tag{3.13}$$

for probing the interface traction distribution (Willis, 1996; Hong *et al.*, 2003; Kim *et al.*, 2012). The auxiliary field $\hat{S}$ is constructed for the material of its initial linear elastic deformations in the real system as follows illustrated in Figure 3.5 (a): first, a sinusoidal traction distribution $\mathbf{t}^{(\mathrm{I})}$ of wave number $n=1$ is imposed on a half-space D_1, to determine the tractions $\mathbf{t}^{(\mathrm{II})}$ at a depth of *H*. Then we impose tractions $\text{-}\mathbf{t}^{(\mathrm{II})}(x_1)$ on another half-space D_2, and superpose the two fields of D_1 and D_2 together to obtain the auxiliary field $\hat{S}$. Figure 3.5 (b), (c) and (d) correspondingly demonstrate σ_{11}, σ_{22} and σ_{12} stress fields of D_1 subjected to surface traction $\mathbf{t}^{(\mathrm{I})}$, D_2 subjected to surface traction $\text{-}\mathbf{t}^{(\mathrm{II})}(x_1)$ and the auxiliary field $\hat{S}$. In this way of superposition, the auxiliary field $\hat{S}$ satisfies Equation (3.11), (3.12) and (3.13) presented in the fourth column set of Figure 3.5. Then, by expressing the real tractions along the grain boundary in terms of the Fourier series in Equation (3.9), and by varying the wave number *n* of the auxiliary tractions $\mathbf{t}^{(\mathrm{I})}$, we can reconstruct the grain boundary traction and the atomic slip distributions near the grain boundaries.

Figure 3.6 presents the projected tractions of pure Cu ∑5/(310) symmetric tilt grain boundaries obtained by interior and exterior field projection methods using up to eight Fourier terms and the virial stresses σ_{22} of grain boundary atoms respectively. Our numerical experiments show that the projected grain boundary traction distribution

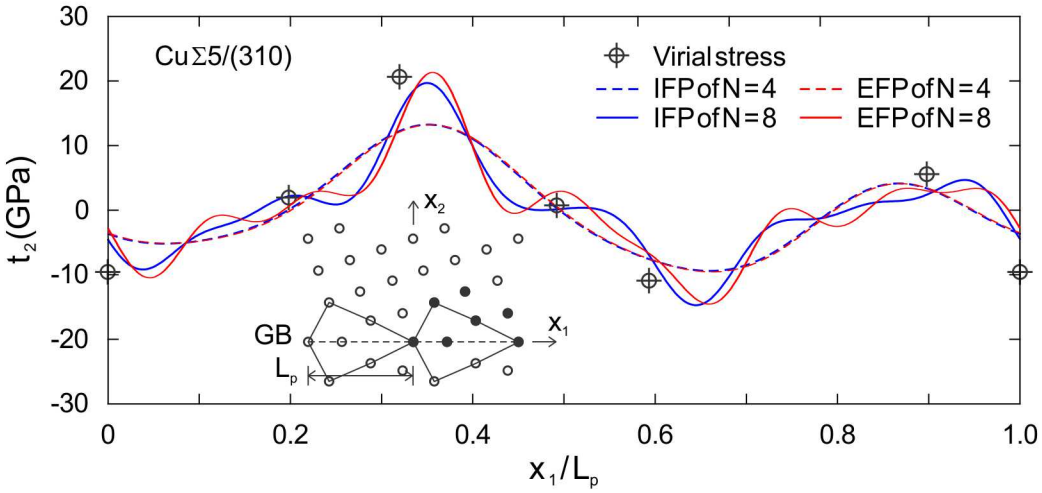

Figure 3.6 Comparison of virial stresses and the normal traction distributions of symmetric tilt Cu ∑5/ (310) grain boundaries through the interior and exterior field

through EFP is reasonable close to the one through IFP. Moreover, the projected result is independent of the integration paths and rapidly converges after eight Fourier terms, which demonstrates the overall stability of the numerical scheme. At the discrete atomic sites, the interior and exterior projected stresses both are in good agreement with the virial stress values. Furthermore, these exterior projected tractions satisfy force balance along the grain boundaries, i.e. zero net vertical forces in the absence of far field loading, unlike the virial stresses through arbitrary interpolation schemes.

Figure 3.7 depicts the atomic slip distributions along the easy-glide pathway for dislocation emission from the symmetric tilt grain boundaries of Cu ∑5/(310) obtained from the exterior field projection method. In addition, in order to verify the capability of the exterior field projection method, a finite element analysis is carried out to check the elastic fields of the bicrystal containing pure Cu ∑5/(310) boundaries. In the finite element implementation, the projected traction distribution through EFP is applied along

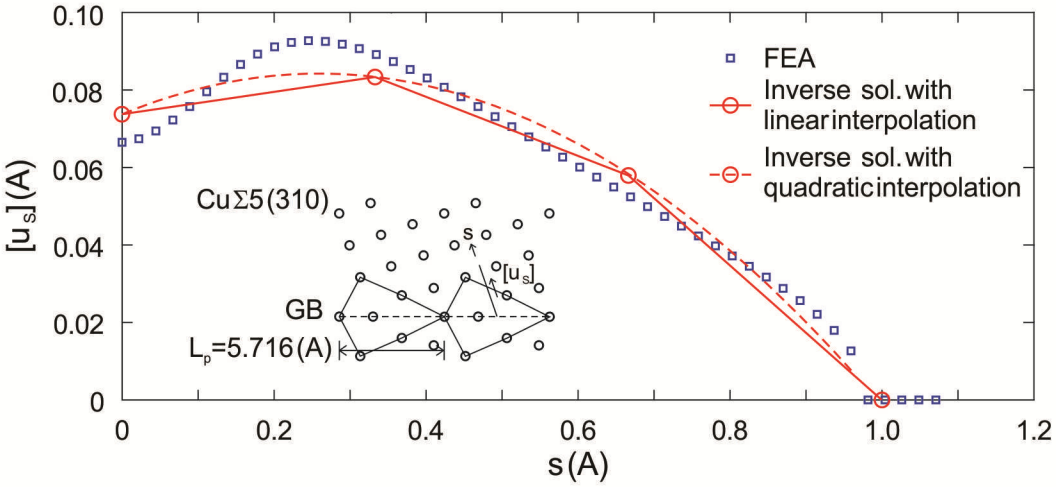

Figure 3.7 Comparison of the slip distributions near Cu ∑5/(310) grain boundary of the inverse solution from the exterior field projection and the numerical solution from the finite element analysis.

Γ_1 of domain R, periodic boundary conditions are set along Γ_2 and Γ_4 for the corresponding degrees of freedom, the atomic slips are modeled using cohesive zone laws calibrated by the generalized stacking fault energies of Cu and the infinite elements are used to define the unbounded domains for simulating the bulk regions of Cu. With above settings of boundary conditions and special-purpose elements, four-node bilinear meshes over 360 × 640 sampling grid are constructed for the upper grain of the bicrystal of Cu ∑5/(310) within $0\,\mathring{A} \le x_1 \le L_p\,\mathring{A}$ ($L_p = 5.716\,\mathring{A}$) and $0\,\mathring{A} \le x_2 \le 2.5L_p\,\mathring{A}$ for acquiring the elastic fields near the grain boundary. The elastic fields of stress and displacement through the finite element analysis are shown in Figure 3.8 and Figure 3.9

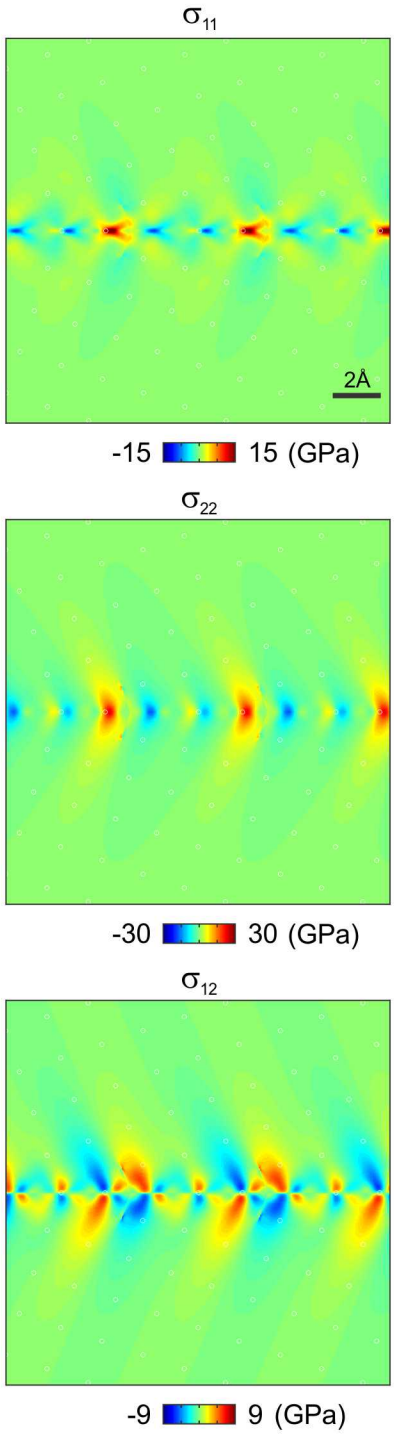

Figure 3.8 Stress distributions near symmetric tilt grain boundaries of Cu ∑5/(310) through the finite element analysis with the boundary condition of the projected grain boundary tractions.

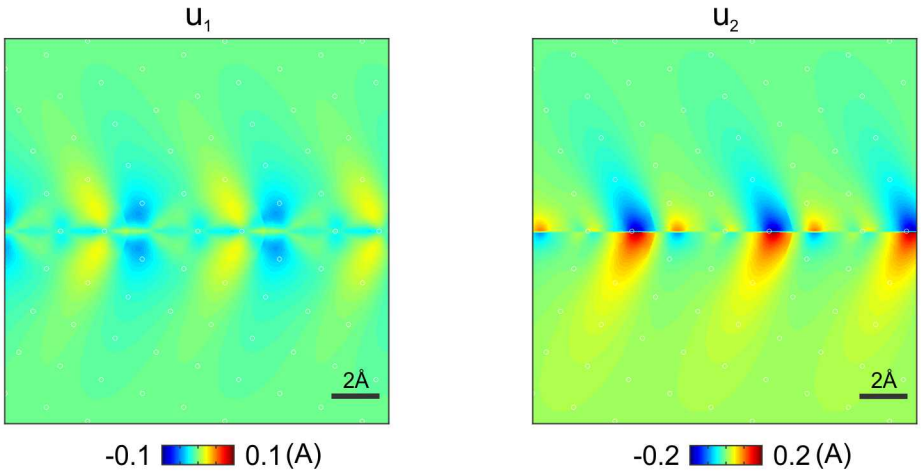

Figure 3.9 Displacement distributions near symmetric tilt grain boundaries of Cu ∑5/(310) through the finite element analysis with the boundary condition of the projected grain boundary tractions.

respectively. The slip distribution $[\![u_s]\!]$ along Γ_5 from finite element analysis is presented in Figure 3.7 and has good agreement with the projected result of nodal distribution on the sampling grid. Similarly, the elastic fields of Almansi strain near the symmetric tilt grain boundaries for far-field uniaxially strains up to 0.04 and 0.08 are also obtained through the finite element analyses with the identical arrangement mentioned above.

The distributions of deviatoric Almansi strains of the grain boundaries under uniaxial applied strains of 0.00, 0.04 and 0.08 are shown in Figure 3.10. In addition, the slip distributions near these grain boundaries under different levels of loading are presented in Figure 3.11. In the early stage of loading, as the far-field uniaxially straining increases to 0.04, the slip distance increases with similar maximum slip amount, indicating the resolved shear stresses of comparable levels spread along the easy-glide

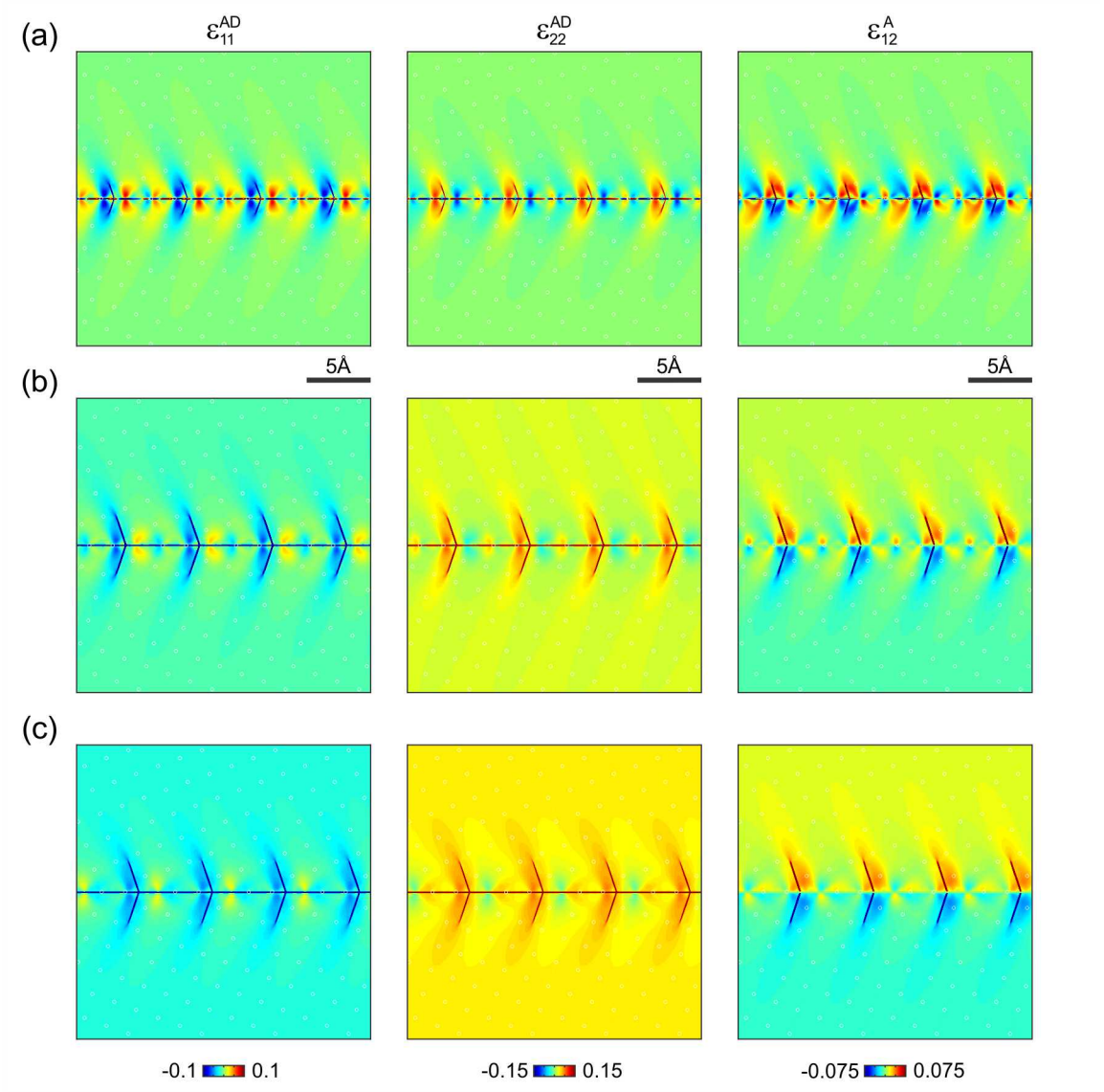

Figure 3.10 Distributions of deviatoric Almansi strains of symmetric tilt Cu ∑5/(310) grain boundaries under uniaxial applied strains of 0.00 (a), 0.04 (b) and 0.08 (c) through finite element analyses. The finite element models contain the special-purpose elements following cohesive zone laws calibrated by the generalized stacking fault energies of Cu along the easy-glide pathway for dislocation emission from the symmetric tilt grain boundaries.

pathway of the bicrystal. When the uniaxial straining increases to 0.08, compared to the stage of far-field strain 0.04, the slip distance increases slightly, but maximum slip

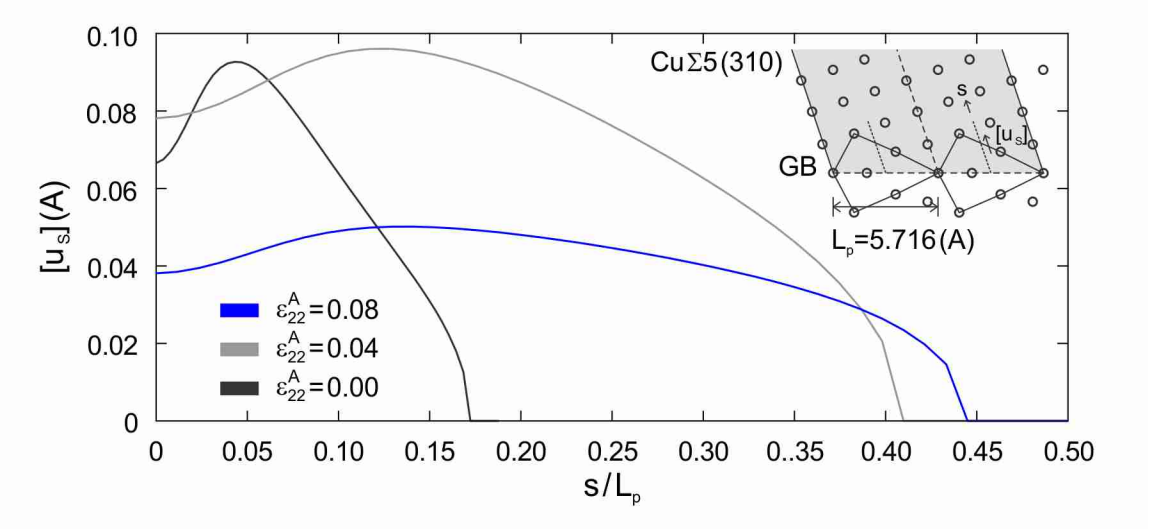

Figure 3.11 Slip distributions near symmetric tilt Cu ∑5/(310) grain boundaries under different uniaxial applied strains through finite element analyses.

amount is reduced by almost two-fold, pointing that the presence of minute atomic rearrangement near grain boundaries, which is also observable in the evolution of the grain boundary normal tractions (Figure 2.16(a)). Therefore, the slip distributions can be used to account for the atomic rearrangement and the activities of dislocations emission of grain boundaries, which are the key understandings for the subject of grain boundary embrittlement. Furthermore, the point which deserves emphasis is that the atomic slip distribution cannot be directly revealed by discrete molecular calculations.

Chapter 4. Atomic Lattice Interferometer for Nanometrology

4.1 Principles and instrumentation

In Chapter 3, the exterior field projection method is developed which can be used to analyze symmetric tilt grain boundaries with various configurations for understanding the underlying mechanism associated grain boundary toughening and embrittlement phenomena. In the exterior field projection method, the essential key to extract the information of grain boundary traction distributions and the atom slip activities near grain boundaries is the accurate deformation measurement of atomic distortions possessing high spatial resolutions in remote regions. In general, many important mechanisms in nanometer scale are related to planar deformations in the nonlocal regions; therefore, it has been in great demand to develop the novel technique of high resolution planar measurement which is capable of sensing atomic strains in full field scanning. In this study, a dual-tip atomic force microscopy interferometry (DT-AFMI) is designed and constructed for studying the energetics of interfacial characteristics between nanostructures.

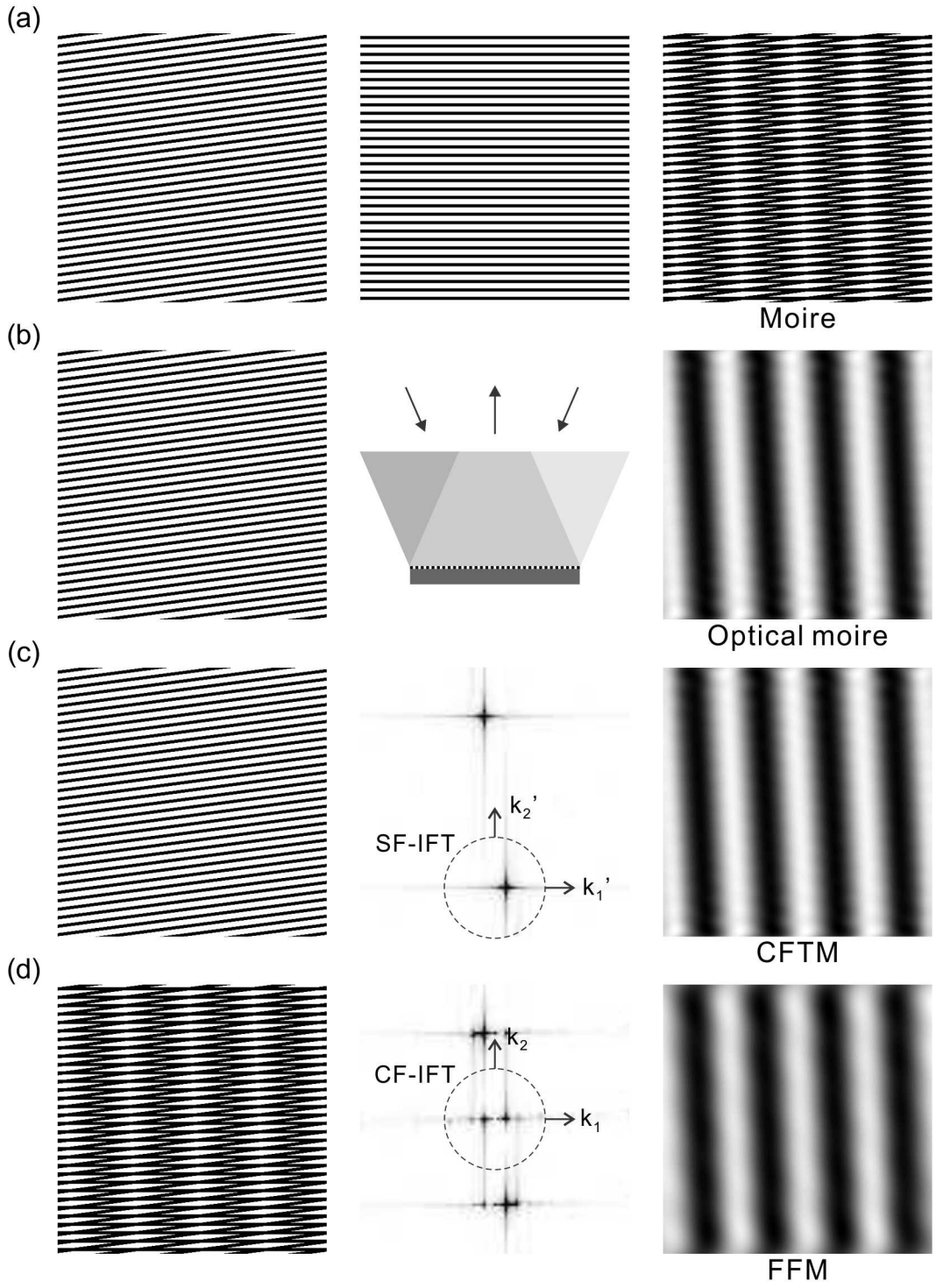

Figure 4.1 Moiré techniques for measuring displacement distributions: (a) Moiré pattern (b) Optical moiré (c) Computational Fourier transform moiré (d) Fourier filtered moiré.

The dual-tip atomic force microscopy interferometry is newly invented to utilize atomic force microscopy (AFM) (Binnig *et al.*, 1982; Binnig *et al.*, 1986; Sadewasser *et al.*, 2004; Sahin *et al.*, 2007; Espinosa *et al.*, 2011; Mohn *et al.*, 2012) with moiré means to gain high resolution of strain measurement over full fields of scan areas. Figure 4.1 demonstrates available moiré techniques for measuring displacement distributions. Since Foucault suggested three methods for testing optical systems in 1859, moiré methods have been broadly applied to deformation measurement techniques (Foucault, 1859). Rayleigh, Righi, Ronchi, Raman and Datta observed and described the phenomena by overlapping two families of gratings to form moiré fringes in the following decades, which gave the advantages of metrology (Rayleigh, 1874; Righi, 1887; Ronchi, 1925; Raman & Datta, 1926). In 1945, Tolenaar first proposed the geometrical explanation on moiré methods in strain analysis, in which one of the primary challenges is to make proper grating lines for desired resolutions of deformation measurement (Tolenaar, 1945).

The nature of geometrical interference moiré is usually used for the measurement of deformation demonstrated in Figure 4.1 (a). When one grating printed on a solid is displaced by certain deformation fields and the other with the identical spacing of grating lines, which is usually called as pitch, is fixed for representing a reference coordinate, the relative displacement between two arbitrary points on the surface of the solid is evaluated as the number of fringes in between, generated by the two gratings, multiplied by the spacing of these grating lines. Conventionally, interference fringes formed through a superposition of two beams of coherent monochromatic light have intrinsic standards for

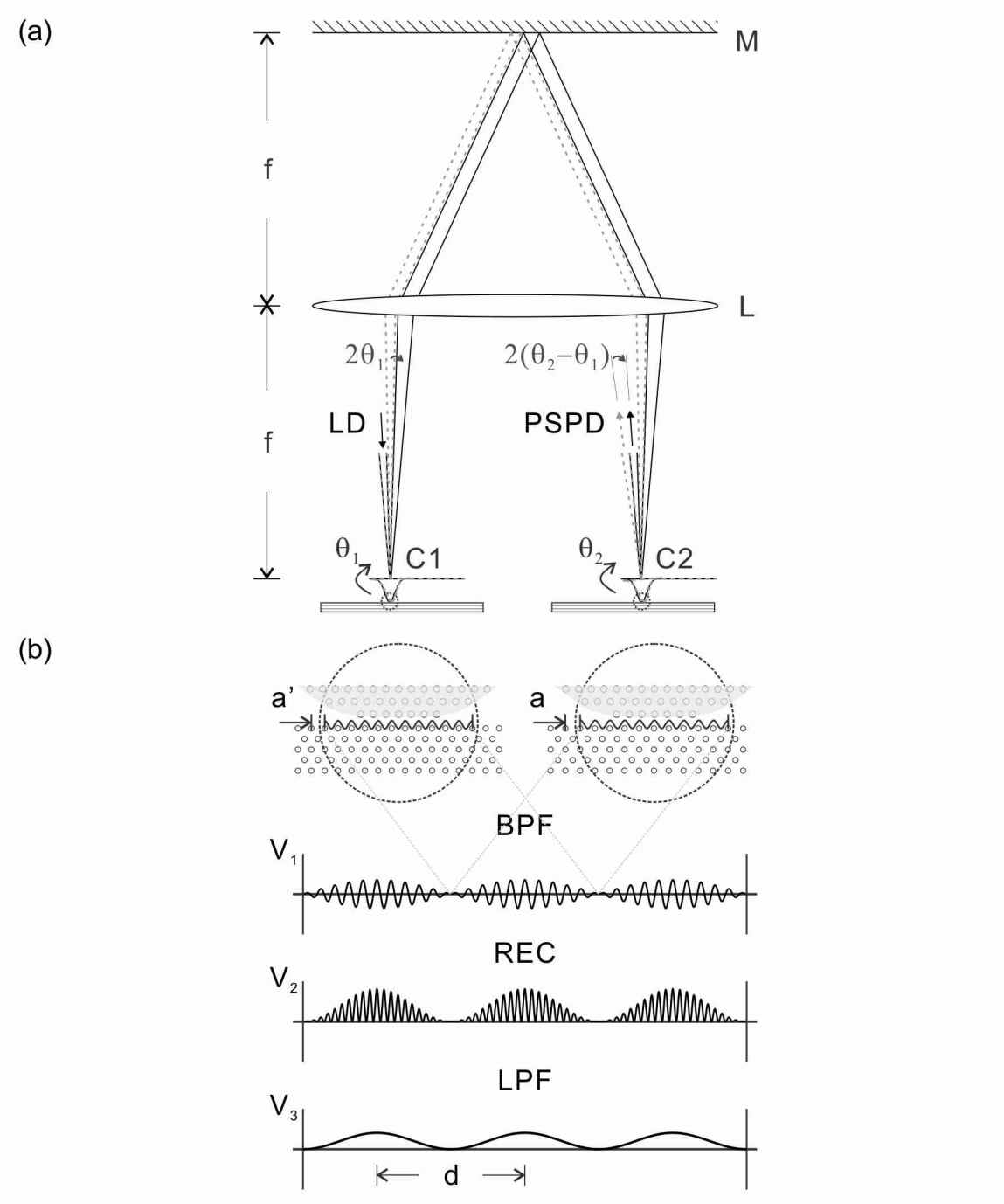

Figure 4.2 (a) Schematic of the optical coupling system of the DT-AFMI that allows PSPD to detect the difference between two scan signals from reference (R) and sample (S) lattices. (b) The filtering scheme containing a band-pass filter (BPF), a square-rectifier (REC), and a low-pass filter (LPF).

deformation measurement in the character of the light wavelength. Shield and Kim invented a moiré microscope which applies the diffraction theory of optical interference moiré as a device for production of variable virtual reference gratings schematically depicted in Figure 4.1 (b) (Shield & Kim, 1991). In the past decades, transmission electron microscopy (TEM) along with image processing techniques such as computational Fourier transform moiré (CFTM) illustrated in Figure 4.1 (c) has been developed successfully to do strain measurement for domains of nanometer scales (Choi, *et al.*, 1992; Hÿtch *et al.*, 1998). Furthermore, Fourier transform algorithm is commonly applied as a filter for processing interference images to acquire fringes as Fourier filtered moiré patterns shown in Figure 4.1 (d). However, at nanometer scales, because of diffraction limits of light, moiré methods by means of optics cannot provide sufficient resolutions of deformation measurement in practice. Moreover, transmission electron microscopy with image processing techniques provides accurate data of nanoscale strain, but only functions well in limited fields of view due to the required number of sampling points for local strain estimation.

In this study, the principle of DT-AFMI utilizing atomic force microscopy is illustrated in Figure 4.2 (a). The optical coupling system of the measurement system enables sensing of differences between the two simultaneous dual-tip scans. In this system, we set both distances from lens L to cantilevers C1/C2, and to mirror M, respectively, equal to the focal length of L. In this way, the image plane of C1 is projected onto C2. Then, the light reflected at C1 always arrives at the same point on C2 regardless of tilting of C1. Furthermore, the net tilt of the light arriving at the position-sensitive photo-diode (PSPD) is twice the relative tilt of C2 with respect to C1. With the

help of this optical coupling system, the two scan signals of sample S and reference R lattices can interfere and are recorded line by line through PSPD. Each interferometric line signal collected by PSPD is shifted to have the intensity average of the interference signal equal to the previous line to remove any possible offset. Then, the interference signals are sent to a set of signal processing moduli including a band-pass filter (BPF), a square-rectifier (REC), and a low-pass filter (LPF) to form atomic moiré fringes with spacing d illustrated in Figure 4.2 (b).

The principle of DT-AFMI technique is presented in the following contents. Consider an AFM scan signal of a reference sample, which is composed of a low frequency envelope roughness $h_0^R(x)$ and high frequency atomic lattices in a sine waveform $e\sin k_0 x$ with a small amplitude e and the wave number k_0 associated with the lattice constant a' presented in Figure 4.2 (b). Then, the signal is represented as

$$h^R(x) = h_0^R(x) + e\sin k_0 x\,. \tag{4.1}$$

Similarly, an AFM signal of a sample of interest is also considered as the combination of a low frequency profile $h_0^S(x)$ and lattices with high frequency $e\sin kx$ with a small amplitude e and the wave number k corresponding to the lattice constant a illustrated in Figure 4.2 (b). The signal is written as

$$h^S(x) = h_0^S(x) + e\sin kx\,. \tag{4.2}$$

For simplicity, it is assumed that the signals of sample and reference lattices have the same amplitude e and zero phases for the following derivations without loss of generality. In DT-AFMI experiment, two scan signals of sample and reference lattices

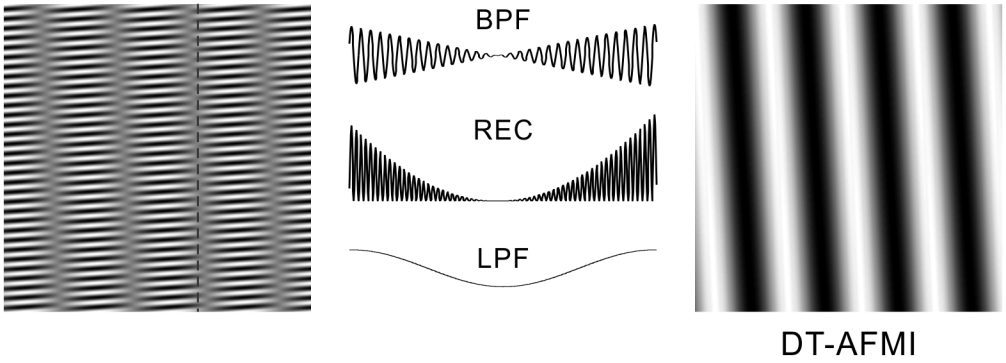

Figure 4.3 Filtering scheme containing a band-pass filter (BPF), a square-rectifier (REC), and a low-pass filter (LPF) to form DT-AFMI images.

can interfere via the novel optical coupling system introduced above and be recorded through PSPD as

$$\begin{aligned} h^I(x) &= h^S(x) - h^R(x) \\ &= \Delta h_0(x) + 2e\cos\frac{(k+k_0)x}{2}\sin\frac{(k-k_0)x}{2}, \end{aligned} \tag{4.3}$$

where $\Delta h_0(x) = h_0^S(x) - h_0^R(x)$. Afterward, consider the processes of square-rectification REC and the subsequently low-pass filter LPF for the interference signal $h^I(x)$. Finally, the harmonic of the lowest frequency which forms atomic moiré fringes are

$$\left\langle \left[h^I(x)\right]^2 \right\rangle = \left\langle \left[\Delta h_0(x)\right]^2 \right\rangle + e^2 + e^2\cos(k_0 - k)x, \tag{4.4}$$

with fringe spacing *d* shown in Figure 4.2 (b) and Figure 4.3.

For example, DT-AFMI scanning of two hexagonal lattices misaligned by 4º would yield a typical moiré pattern presented in Figure 4.4. In addition, since the dual-tip and sample/reference pairs are mounted together respectively, much of the vibrational noise is self-cancelled. Figure 4.4 displays an actual image of the two end cantilevers

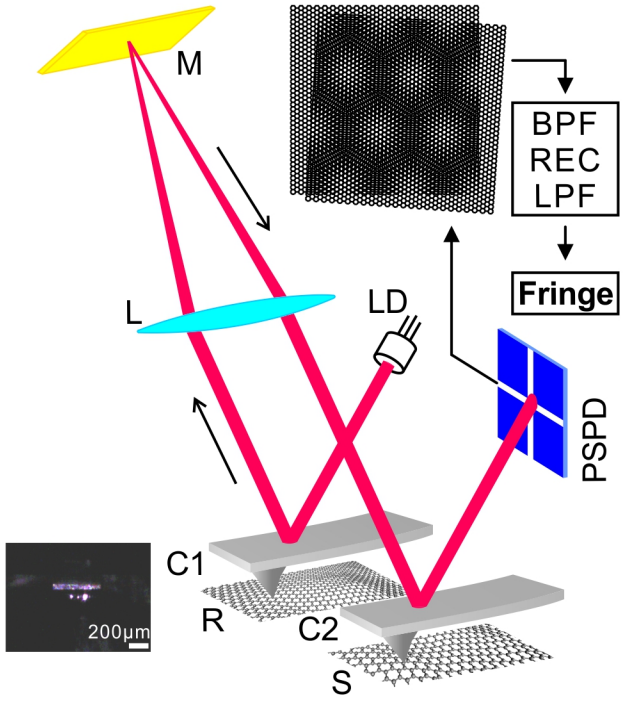

Figure 4.4 Schematic of the optical coupling system of the DT-AFMI including the actual image of the two end cantilevers employed in DT-AFMI for atomic lattice interferometry (ALI) and the sketch of a typical moiré pattern of two hexagonal lattices with 4° relative rotation mismatch.

C1/C2 140 μm apart in the XE-BIO AFM (Park Systems), a sample lattice (S) under C2 and a reference lattice (R) under C1 using atomic lattices, employed in DT-AFMI for atomic lattice interferometry (ALI).

4.2 Experimental procedures

A schematic diagram of DT-AFMI developed in this study is shown Figure 4.5 (a). The DT-AFMI experiments for ALI were carried out in ambient conditions. The DT-AFMI

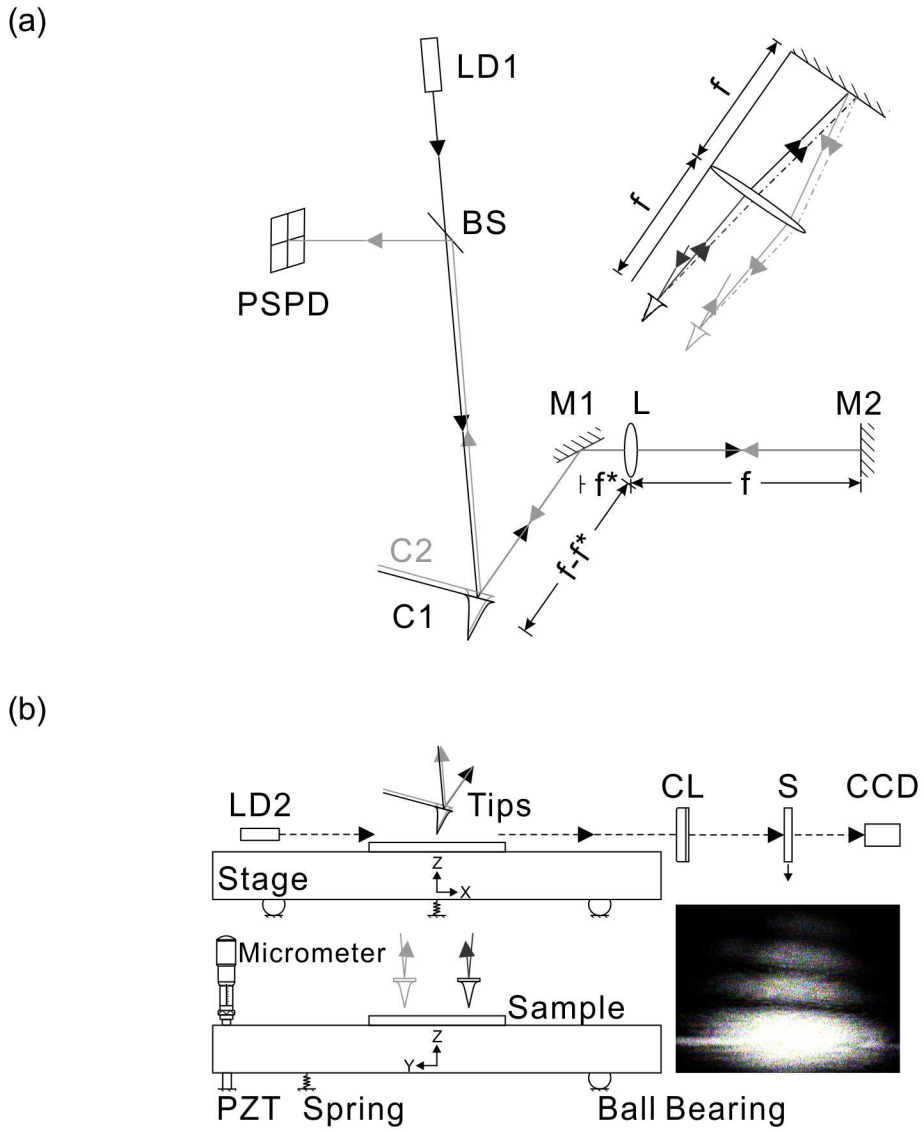

Figure 4.5 Schematic diagram of DT-AFMI instrumentation: (a) the optical coupling system of DT-AFMI and (b) the alignment for the balance between the two tip-to-sample contacts.

scanning was made in contact mode without feedback control, using the AFM cantilevers of Nanosensors, SD-PNP-array2. For maximum moiré interference, balancing between the two tip-to-sample contacts was made in two steps: one by pre-contact alignment of

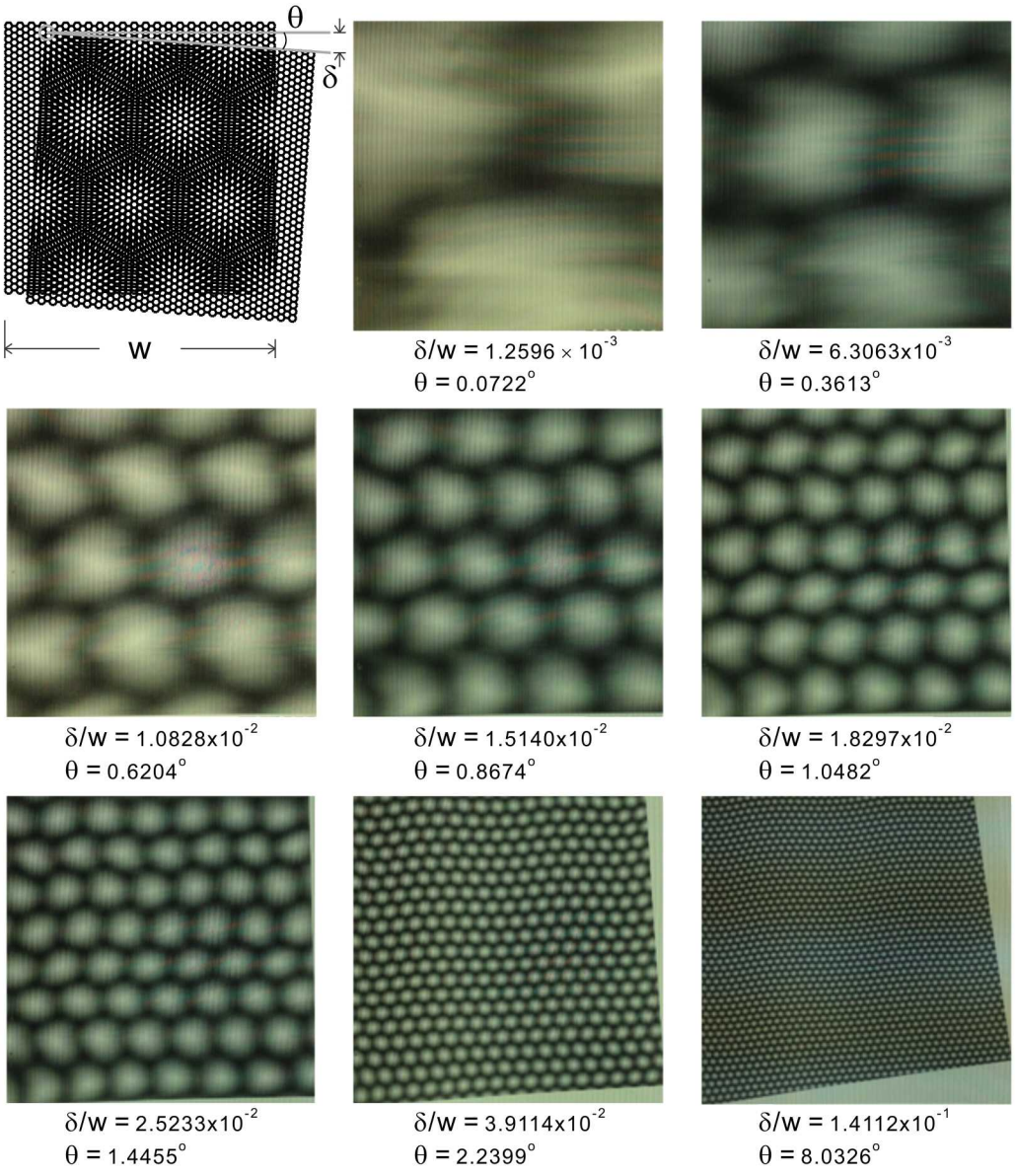

Figure 4.6 The interference patterns of two layers of hexagonal grids with different planar mismatch angles in a simulated experiment.

sample tilt, the other by post-contact alignment with fine adjustment. The pre-contact alignment was guided by Young's fringes (Young, 1804) produced by the gaps between the two tips and the sample surface illustrated in Figure 4.5 (b). The post-contact tilt

alignment was made by making the forward and backward scan profiles identical and stable. Then, the dual-tip scan PSPD signals formed the first-stage DT-AFMI images.

Before going on to the atomic lattice interferometry experiment, interference patterns of two layers of hexagonal structures with a planar mismatch angle are discussed in the following contents. In this simulated experiment, two plain copier transparencies printed with hexagonal grids along with a light box were used. Each of the hexagonal grid layers was simulated as a 70 nm by 70 nm sheet ($w = 70$ nm) with hexagonal unit cells of 0.246 nm lattice spacing. By adjusting the planar mismatch angle θ, different interference patterns were observed. Figure 4.6 indicated that as the larger planar mismatch angle increases, the smaller unit of interference pattern was observed. Therefore, based on the size of the unit of interference pattern, one can identify the in-planar rotation mismatch between these two sheets. The important point to note is that the interferometry acts as a magnifier to amplify minute mismatches to interference patterns, which is observable in the planar domain. In addition, the discrete Fourier transform was applied to check the frequency spectrum of the interference pattern. Figure 4.7 (a) shows the spectrum of the signal with a rotation mismatch of $\theta = 1.4455°$ in Figure 4.6, and the peaks occurs at $(s_1, s_2) = (\pm 2.29, \pm 4.05)$ 1/nm and $(s_1, s_2) = (\pm 4.61, 0)$ 1/nm , which are corresponding frequencies for the original hexagonal grids printed on the two sheets. For the interference patterns, which are amplified signals from the original lattices, one should check the low frequency band in the spectrum of the interference image. Figure 4.7 (b) represents a center region of Figure 4.7 (a) and indicates the peaks at $(s_1, s_2) = (\pm 0.09, \pm 0.05)$ 1/nm and $(s_1, s_2) = (0, \pm 0.12)$ 1/nm . The corresponding frequencies of those peaks shown in Figure 4.7 (b) tell us that the unit of interference

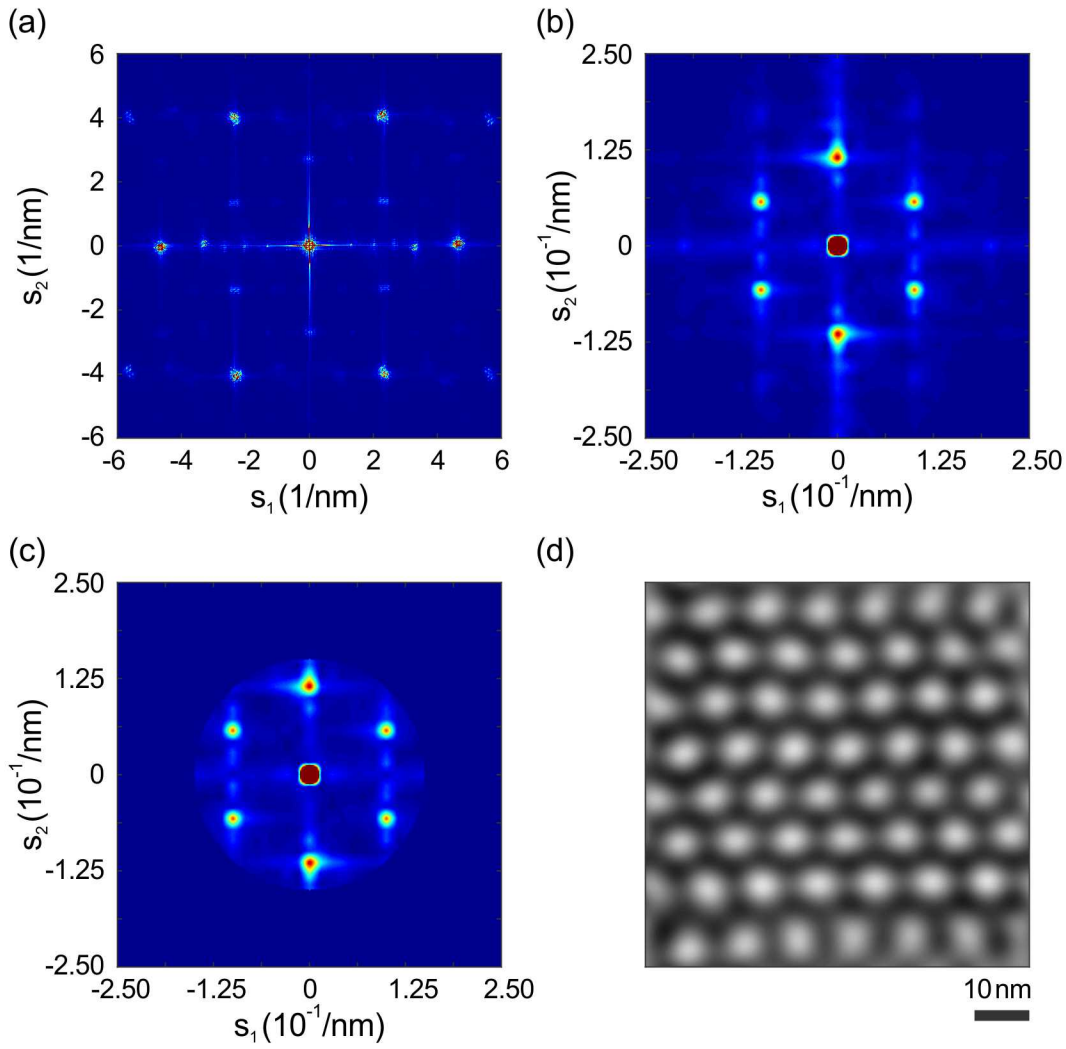

Figure 4.7 (a) Discrete Fourier transform of the interference patterns of the signal of $\theta = 1.4455°$ shown in Figure 4.6 (b) the center region of (a), (c) the filtered spectrum from (b), (d) the recovered interference pattern from (c).

patterns appears per $1/0.12 = 8.33$ nm approximately, and in other words, there is a mismatch of one lattice every 8.33 nm in average. Therefore, the planar strain can be estimated as $0.246\text{ nm}/8.33\text{ nm} = 2.95\%$. In addition, to remove the nonphysical signals of high frequencies, a filter with a cutoff window in the frequency spectrum was used to get rid of any possible noise signals. In this demonstration, the cutoff frequency is

specified as 0.15 /nm to clean those noisy signals and maintain the important peaks corresponding to the interference patterns. Then, the Fourier inversion is applied on the filtered spectrum to recover the interference signals in the space domain. As Figure 4.7 (d) shows, compared to the original signal of $\theta = 1.4455°$ in Figure 4.5, the recovered signal has cleaner interference patterns for identifying planar deformations.

4.3 Signal processing and measurement results

In this section, we applied the high-precision DT-AFMI for ALI to uncover atomic-scale crinkle (Pipkin, 1986) configurations in highly oriented pyrolytic graphite (HOPG), a layered structure with a high stiffness ratio of layer-stretching to interlayer-shearing (Novoselov *et al.*, 2004; Liu *et al.*, 2013). Bending of such a structure segregates zones of two easy deformation modes – interlayer shear and individual-layer bending. When the structure is buckled under compression, this segregation produces a sharp strain jump from one interlayer shear to another across a concentrated zone of individual-layer bending. Periodic appearance of such strain jumps sets up a crinkle. The crinkle forms mosaic (Xu *et al.*, 2006) patterns of sloped flat regions (pqq'p' and qrr'q') separated by ridges (qq') on the surface (Figure 4.8(a)). Crinkles can stably maintain their shape by vertical series of subsurface interlayer dislocation loop spinned by carbon interstitials (Kan *et al.*, 1987) without external compression as depicted in Figure 4.8 (b) of the non-contact AFM scanning image over 250 μm × 250 μm on grade III HOPG.

We consider the measurement of the crinkle strain jump across an atomic-scale width as the ultimate test of our DT-AFMI for ALI. In our experiment, we used grade III

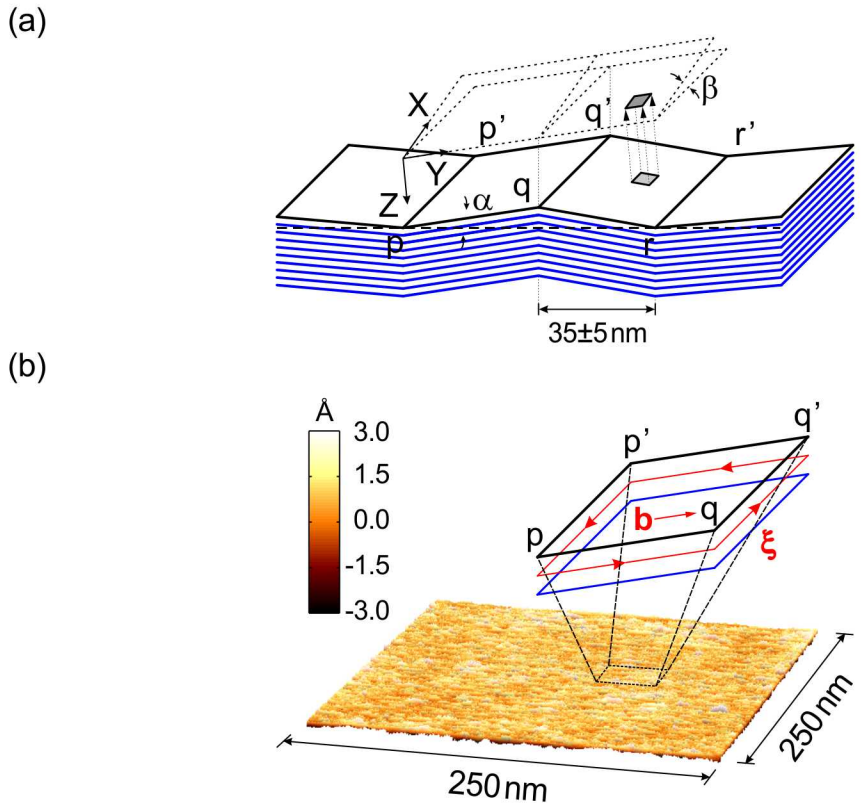

Figure 4.8 (a) Sketch of a crinkle in HOPG of 35 nm nominal mosaic size. The scanning plane (X-Y) is displayed with (α, β) tilt angles. (b) AFM non-contact scanning image of HOPG grade III and a schematic of a mosaic block containing an interlayer dislocation loop ξ with Burgers vector $\mathbf{b}$.

HOPG of 35 nm nominal mosaic size and $3.5° \pm 1.5°$ mosaic angle. Figure 4.9 (a) shows a DT-AFMI scan image of a 22×22 nm^2 area, constructed by the unfiltered PSPD data. For this ALI of DT-AFMI scans, the image shows clear surface atomic-layer steps presented in the profile plotting (Figure 4.9 (b)), signifying substantial self-cancelation of noise, and the unfiltered DT-AFMI interference patterns. Then, the interference image was digitally Fourier-transformed presented in the right of Figure 4.10 (a). Only the

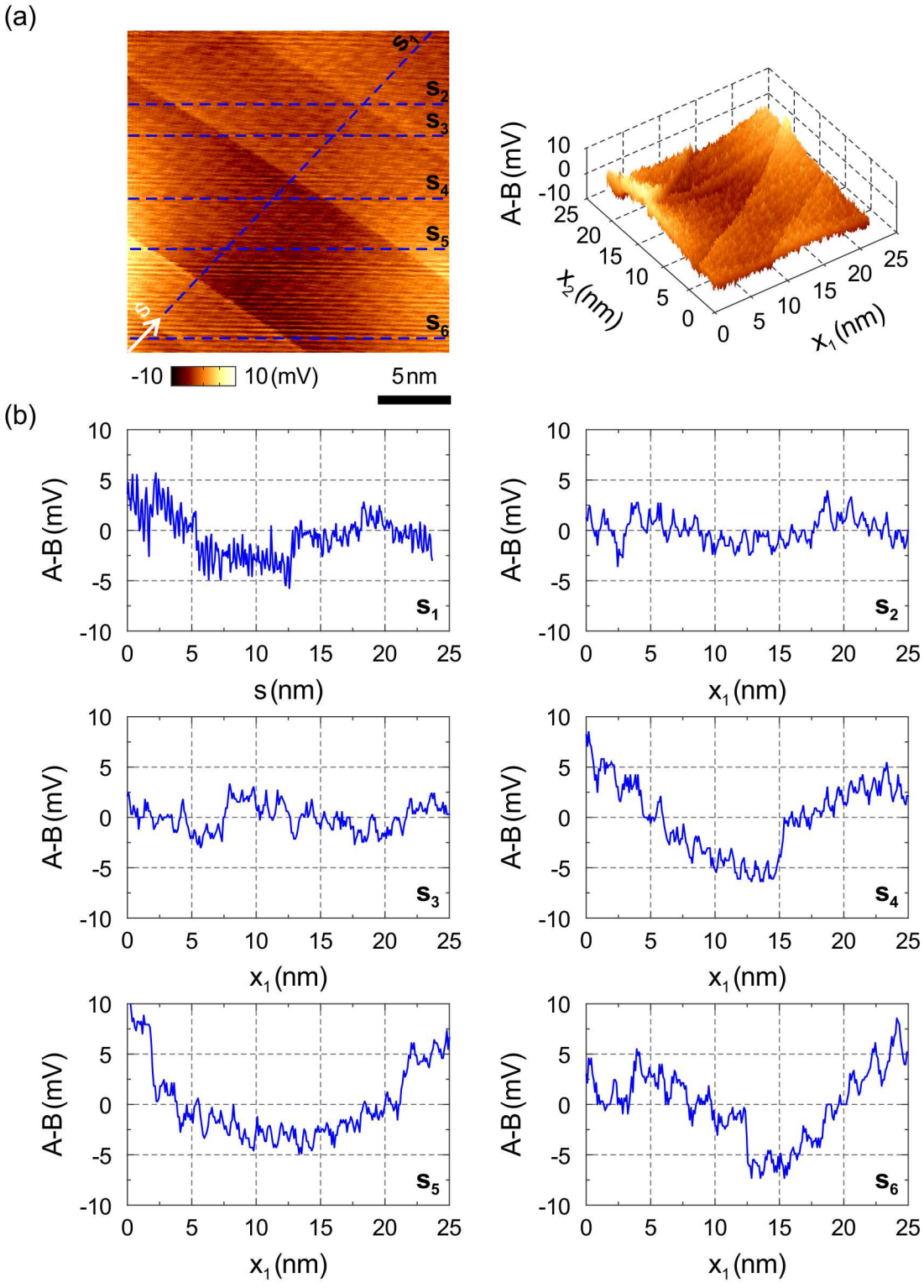

Figure 4.9 Unfiltered dual-tip AFM scanning image of HOPG grade III and the raw data of line scans.

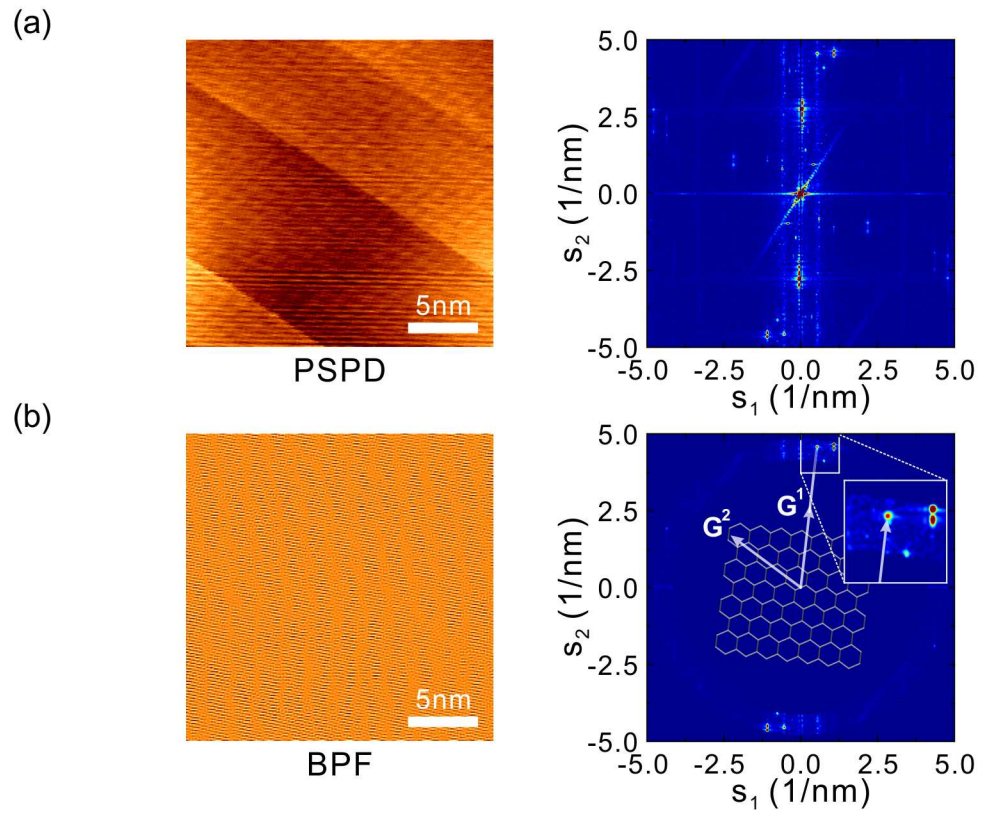

Figure 4.10 (a) Unfiltered interference image of 22 × 22 nm^2 area of HOPG grade III sample and the corresponding Fourier spectrum. (b) Right: The reciprocal of unfiltered image collected by PSPD, showing reciprocal lattices $\mathbf{G}^1$ and $\mathbf{G}^2$ in two arm-chair directions. Only the frequency in a radial band was inverse-transformed through a band-pass filter. Left: The Fourier inversion of the band-pass filtered reciprocal of interference image.

frequency in a radial band was inverse-transformed (BPF in Figure 4.4). The right of Figure 4.10 (b) displays the reciprocals of the reference (single red-dot) and sample (two red-dots) lattices denoted as $\mathbf{G}^1$ and $\mathbf{G}^2$ in arm-chair directions, and the center frequency of the band was then chosen to be the frequency of the reference lattice. The inverse-transformed image in Figure 4.10 (b) was rectified (REC) (Figure 4.11 (a)) and subsequently passed through a low-pass filter (LPF) shown in the right of Figure 4.11 (a)

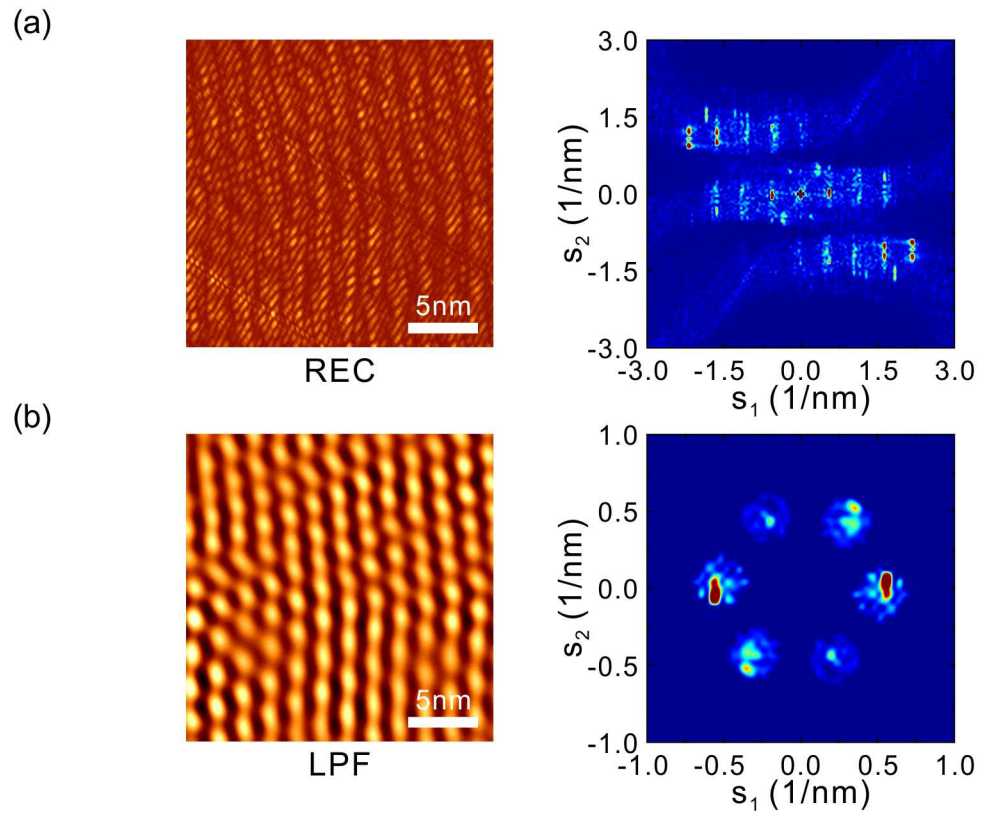

Figure 4.11 (a) The square-rectified image of the left of Figure 4.10 (b) and the corresponding Fourier spectrum. (b) Right: Three pairs of symmetric partial-filters are applied for the Fourier spectrum in (a). Left: The Fourier inversion of the partial-filtered spectrum shows the fringe image of the fundamental-mode.

and Figure 4.11 (b) to form moiré fringes shown in the left of Figure 4.11 (b). The right of Figure 4.11 (b) is the reciprocal of the moiré fringes, of which Fourier inversion through a pair of symmetric partial-filters gives moiré fringes presented in Figure 4.12 (a) corresponding to the displacements in the relative direction of the pair. The filter size determines the resolution of the fringe location.

In ensuing fringe analysis, the isodensitracing method, which is an efficient way of obtaining fractional moire fringes and retrieving important information of fractional

displacement distributions from moire patterns along the principal directions of the gratings, was applied (Theocaris, 1967). The isodensitracing method is briefly introduced as follows. The exact position of each intermediate fractional order in the displacement-position curve is determined by evaluating the ratio of the distance width measured by an isodensitogram using a ruler with equal intensity divisions. One advantage of this method is that the fractional moiré map traced by the isodensitogram can yield a complete detailed view of the two-dimensional fringe distribution field which is independent of the changes in the intensity amplitudes between fringes. Then, the fringe distribution function is used to obtain the strain fields from the relationship between the fringe and deformation gradients. In this study, the mathematical relationship between the fringe distribution and the surface deformation for geometrical moiré method derived by Shield and Kim (Shield & Kim, 1991) was applied to determine the surface Almansi strains of the current configuration, which are insensitive to rigid body movement from the derivatives of the fringe distributions. The deformation analysis for the atomic fringes collected by DT-AFMI is addressed in brief in the following contents. The surface-deformation gradient tensor is expressed as

$$\mathbf{F} = \mathbf{H}^{-T} \cdot \mathbf{\Gamma}^{T}, \tag{4.5}$$

where $\mathbf{\Gamma}$ is the second-order specimen-grating tensor written as

$$\mathbf{\Gamma} = \sum_{\alpha=1}^{2} \mathbf{G}^{\alpha} \otimes \mathbf{G}^{\alpha} \tag{4.6}$$

for the specimen grating $\mathbf{G}^{\alpha}$, $\alpha = 1$ or 2 for two-dimensional problems, and $\mathbf{H}$ is defined as

$$\mathbf{H} = \sum_{\alpha=1}^{2} \left(\mathbf{G}^{\alpha} - \nabla f^{\alpha} \right) \otimes \mathbf{G}^{\alpha}, \tag{4.7}$$

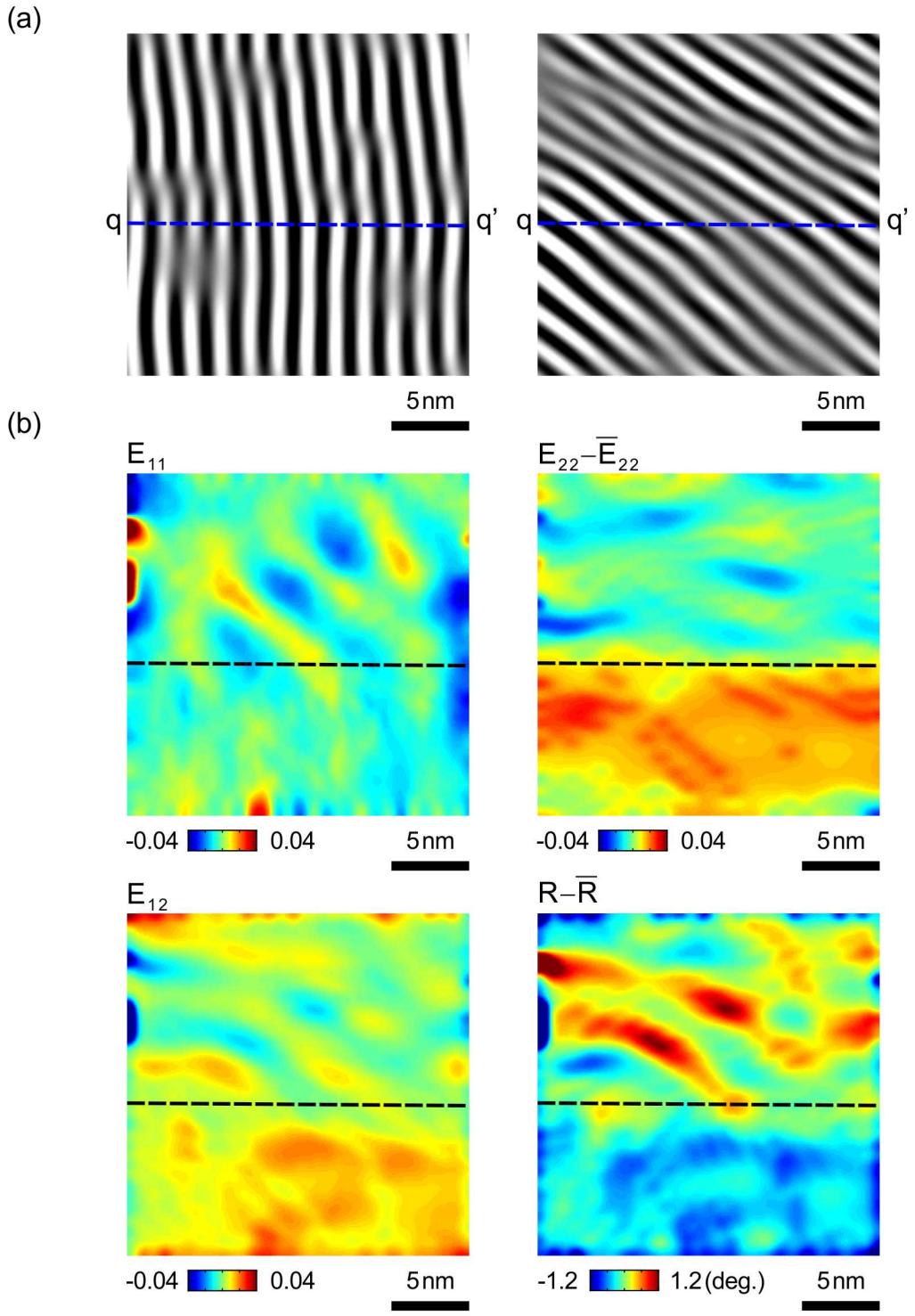

Figure 4.12 (a) Two sets of filtered fringes in two different directions. (b) Contours of Almansi strain E_{11}, $E_{22}-\bar{E}_{22}$ ($\bar{E}_{22}=-0.026$), E_{12} and rotation $R-\bar{R}$ ($\bar{R}=6.5^{\circ}$).

where f^{α} is the fringe number function which is produced by the specimen grating $\mathbf{G}^{\alpha}$. Now, we have the complete information of the displacement fields to determine the surface Almansi strain

$$\mathbf{E}^{A} = \frac{1}{2}\left[\mathbf{I} - \left(\mathbf{F}\cdot\mathbf{F}^{T}\right)^{-1}\right], \tag{4.8}$$

which is a useful measure in the deformed configuration observable in experiments and the local rotation

$$\mathbf{R} = \mathbf{F}\cdot\mathbf{U}^{-1}, \tag{4.9}$$

where $\mathbf{U}$ is the right stretch tensor and written as $\mathbf{U} = \left(\mathbf{F}^{T}\cdot\mathbf{F}\right)^{1/2}$.

In the strain analysis for the DT-AFMI image shown in the left of Figure 4.11 (b), the atomic lattice grating $\mathbf{G}^{1}$ and $\mathbf{G}^{2}$ of HOPG were $\left[0.1133 \quad -0.9936\right]^{T}/\Delta$ and $\left[-0.8038 \quad -0.5949\right]^{T}/\Delta$, which produce the fringes shown in the left and the right of Figure 4.12 (a) respectively, where Δ denotes the grating spacing which is the spacing of the atom arrays in the zig-zag orientation of graphite surface and is confirmed as 0.213 nm by theoretical studies and experimental measurements. In Figure 4.12 (a), the dashed line qq' denotes a crinkle ridge which is revealed by the fringe analysis of the interference patterns. These fundamental-mode fringes of the interference patterns are constructed by the filtering processes introduced above. The fringes are distinctly kinked along qq'. The fringe analysis then provides material rotations projected on the X-Y scan plane with tilt angles α and β (Figure 4.8 (a)). The global in-plane rotation with respect to the reference lattice is measured as $6.5° \pm 0.3°$ with a 0.5° jump across the crinkle ridge caused by the β tilt shown in Figure 4.12 (b). Figure 4.12 (b) also displays the

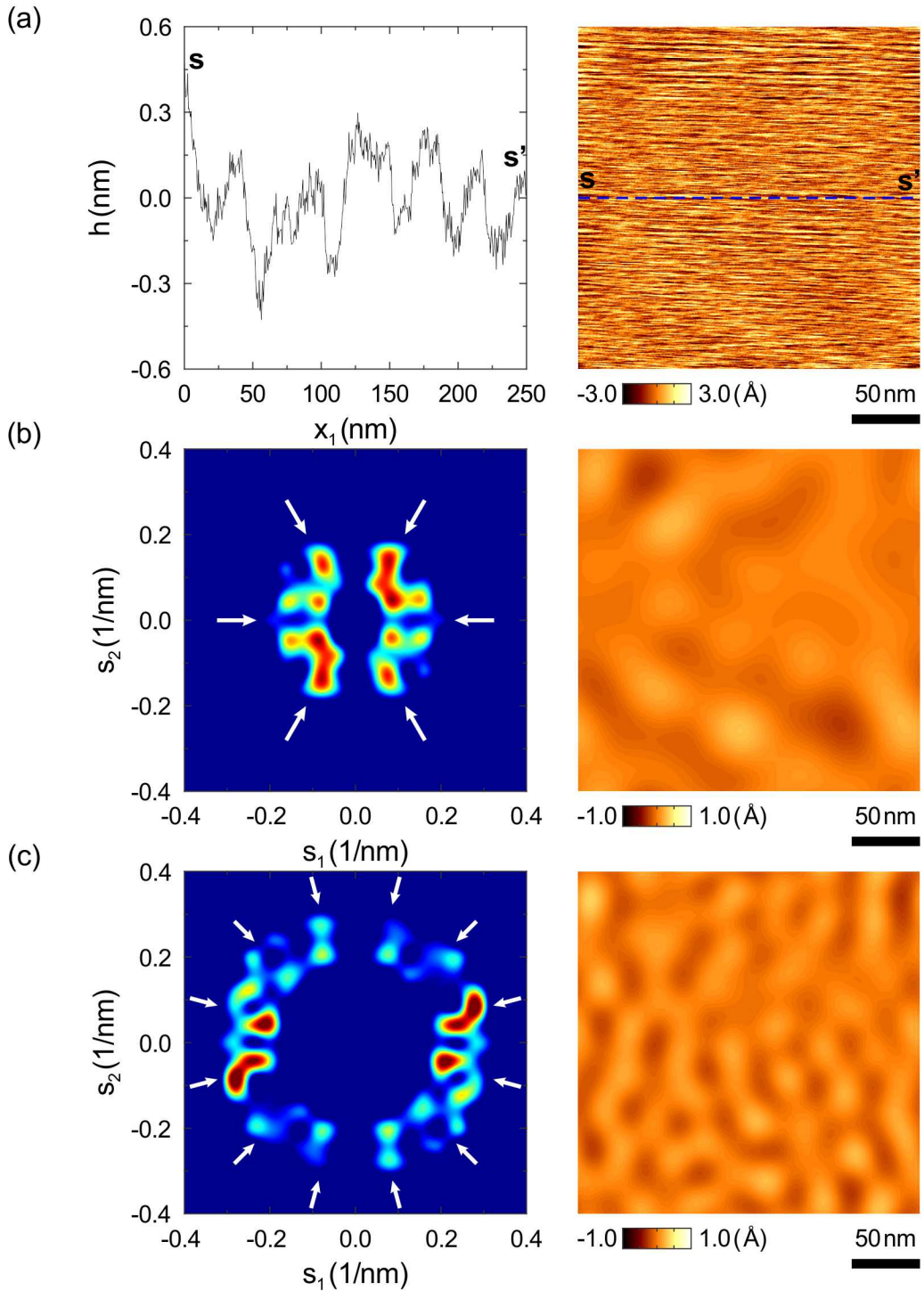

Figure 4.13 (a) Non-contact AFM analysis of HOPG III mosaic patterns. (b) The first-mode frequency band in k-space indicating three-fold symmetry in the mosaic patterns. (c) The second-mode frequency band implying the six-fold symmetry in the mosaic patterns.

distributions of in-plane Almansi strains for projection-mapping of the relative lattice-displacements to the scan plane. The two strain components $E_{11}\left(-0.004 \pm 0.007\right)$ and $E_{12}\left(0.005 \pm 0.007\right)$ are negligible. The stretch strain in the direction perpendicular to the ridge E_{22} is binarized and jumps significantly from -0.035 ± 0.005 to -0.016 ± 0.006, implying a jump in crinkle slope from 14.9° to 8.7° with measurement accuracy of $\pm 0.1°$. This ALI study shows that DT-AFMI can detect strains and surface tilts with three-digit accuracy in an atomic-scale window, with strong self-canceling of vibrational noise.

In Figure 4.13, it is presented that multi-directional crinkles produce disoriented tilts of mosaic blocks through AFM analysis of HOPG mosaic patterns. Distribution of the tilts gives mosaic spread – a measure of non-uniformity in atomic-layer parallelism – represented by crystallographic X-ray peak spreading of the **Cu-K_a** rocking curve (Ohler *et al.*, 1995). However, detailed atomic-scale structures of the mosaics are not well understood yet, despite its importance in a broad range of applications (Gott *et al.*, 2003). Figure 4.13 (a) reveals approximately seven crinkle-ridge bumps and $2° - 5°$ mosaic slopes in a conventional noncontact-mode AFM line-scan over 250 nm × 250 nm. AFM-tip bluntness makes the crinkle-ridge peak profiles dull and the mosaic patterns vague in the right of Figure 4.13 (a). Three-fold symmetry in the first mode of the mosaic patterns is revealed in a set of low-frequency k-space (the left of Figure 4.13 (b)) and real-space (the right of Figure 4.13 (b)) plots, while the second mode has six-fold symmetry shown in Figure 4.13 (c). Ridges along arm-chair directions have lower energy than ridges along other directions, and low-energy stacking of the ridges in the three arm-chair directions would likely form kagome patterns of the ridge network, giving such diffraction-pattern

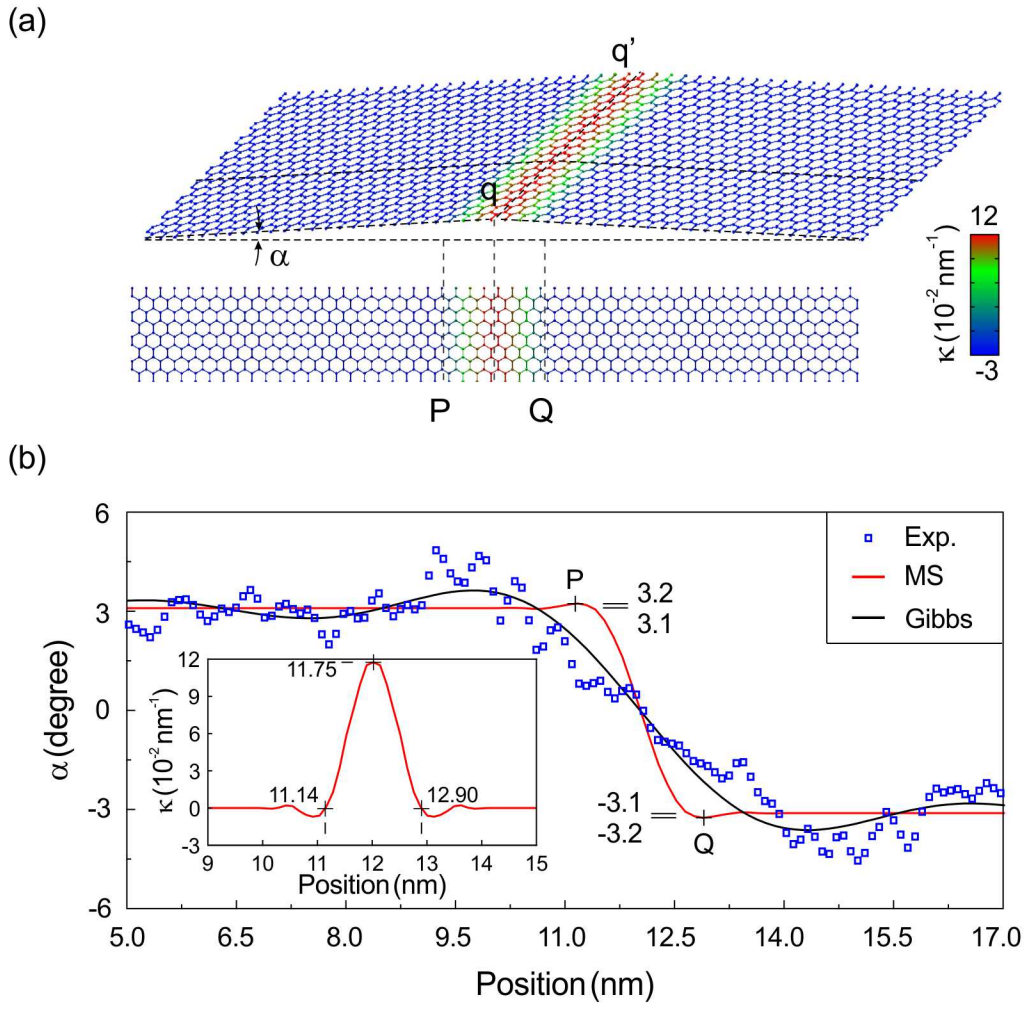

Figure 4.14 (a) Modeled surface crinkle of graphite configuration via molecular statics (MS). The contour shows curvature distribution which highly concentrates within PQ region. (b) DT-AFMI analysis of a crinkle-ridge structure. The slope-angle distributions across qq' from DT-AFMI experiment and MS simulation. The Gibbs curve is from Fourier imaging analysis of the crinkle configuration produced by MS. Inset: The corresponding curvature distribution across the ridge (PQ).

symmetries. While conventional AFM can give information on the distributions of mosaic sizes and shapes, DT-AFMI can accurately measure individual mosaic slopes, transition-zone characteristics of the crinkle ridge at the mosaic boundary, and the surface-curvature focusing behavior of the ridge.

One highlight of atomic-scale deformation measurements with DT-AFMI is the characterization of the slope transition across a crinkle ridge shown in Figure 4.14. The slopes α denoted as blue markers in Figure 4.14, directly converted from E_{22} shown in Figure 4.12 (b) with a simple tilt-projection relationship

$$\cos\alpha = \left(1 - 2E_{22}\right)^{-\frac{1}{2}} \tag{4.10}$$

closely match those of simulation denoted as black solid-line. Here, simulation stands for Fourier imaging of the crinkle configuration predicted by molecular statics (MS, red solid-line). MS simulations for the crinkle configurations were carried out employing LAMMPS (Plimpton, 1995) (AIREBO potential (Brenner *et al.*, 2002)). Fourteen-layer graphene was modeled with a supercell of 70 nm × 0.78 nm in MS simulations. All structures were fully relaxed under periodic boundary conditions, which can accommodate the crinkle geometry, with a force-stopping criterion of 10^{-8} eV/Å for calculations. The simulations show overshooting of the slope in the transition, caused by both a quantum-mechanical effect and the Gibbs phenomenon of imaging (Gibbs, 1898). Our simulation-assisted data analyses evaluate the width, the kink angle and the minimum radius of the ridge as 1.76 nm, 6.2° and 8.51 nm, respectively.

In Figure 4.15 and Figure 4.16, other two different DT-AFMI scanning images taken on the specimen of HOPG grade III and the corresponding fringe images and strain fields are presented. Figure 4.15 (a) and Figure 4.16 (a) are the unfiltered PSPD images. Figure 4.15 (b) and Figure 4.16 (b) are the atomic moiré fringes through the filtering processing as introduced before. The moiré fringes shown in Figure 4.15 (c,d) and Figure 4.16 (c,d) were subsequently obtained through pairs of Fourier symmetric partial-filters

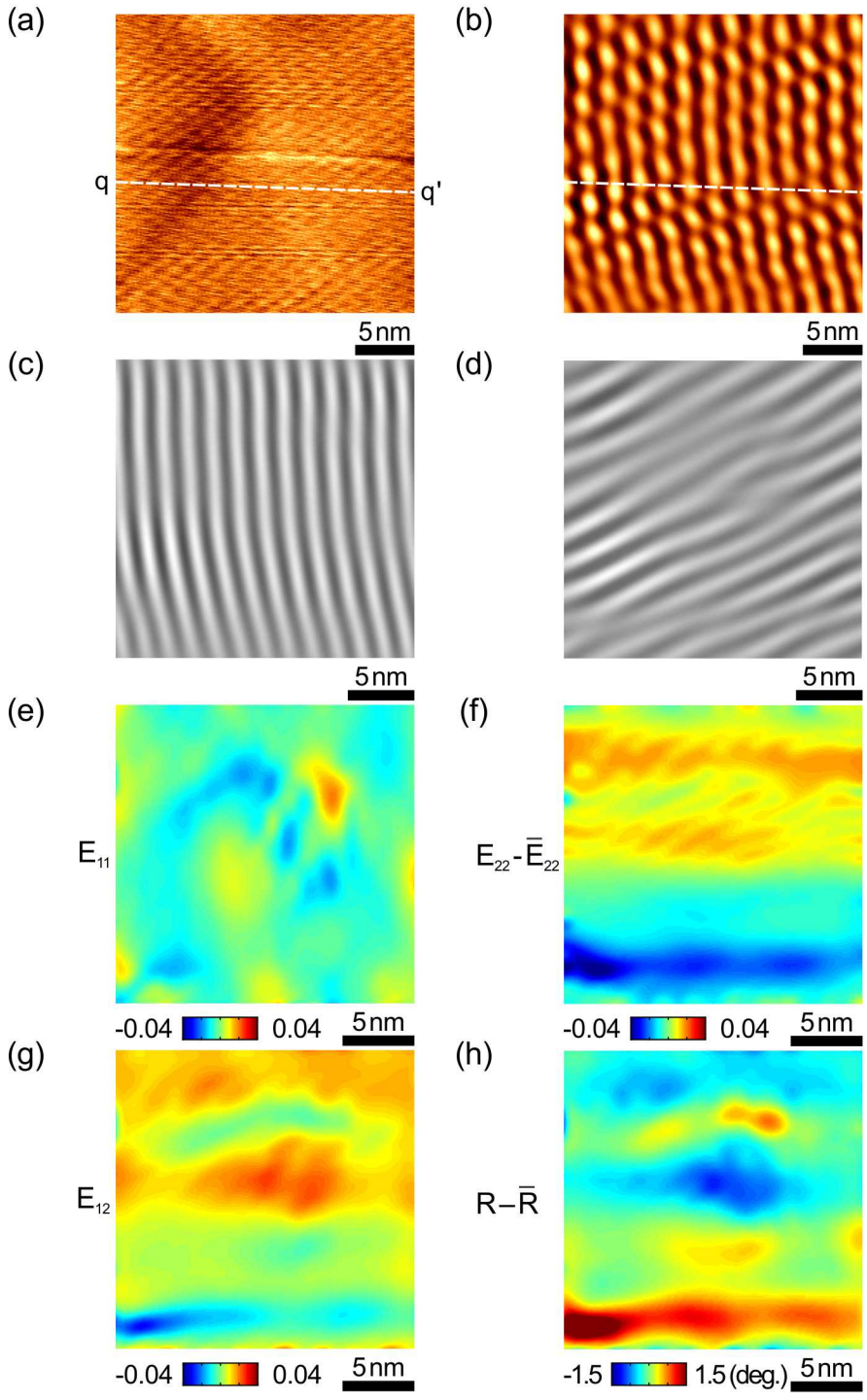

Figure 4.15 (a) The unfiltered interference image of HOPG grade III sample. (b) LPF of the image. (c,d) Two sets of filtered fringes in two different directions. (e-h) Contours of Almansi strain E_{11}, $E_{22}-\bar{E}_{22}$ ($\bar{E}_{22}=-0.033$), E_{12} and rotation $R-\bar{R}$ ($\bar{R}=6.5°$).

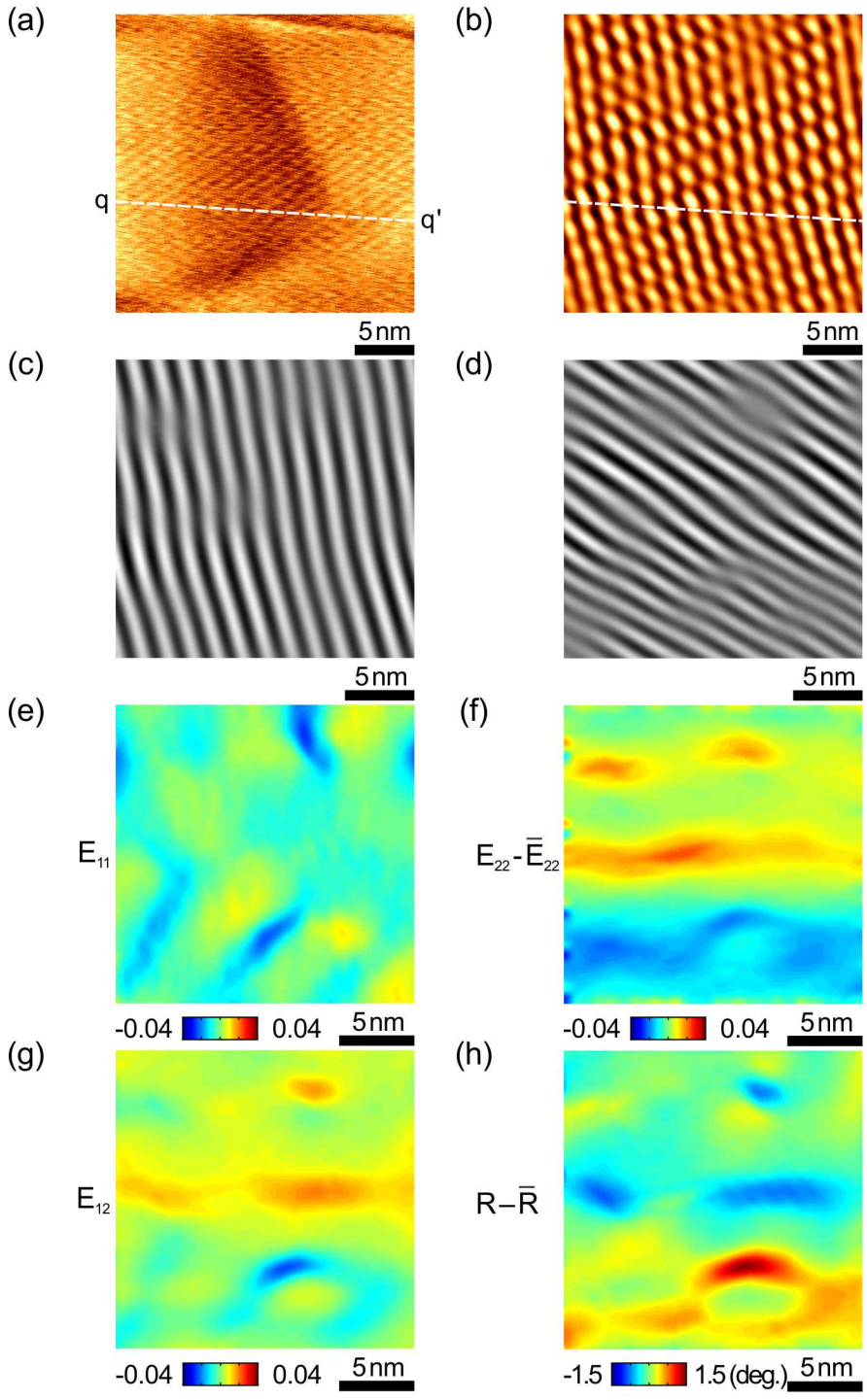

Figure 4.16 (a) The unfiltered interference image of HOPG grade III sample. (b) LPF of the image. (c,d) Two sets of filtered fringes in two different directions. (e-h) Contours of Almansi strain E_{11}, $E_{22}-\bar{E}_{22}$ ($\bar{E}_{22}=-0.045$), E_{12} and rotation $R-\bar{R}$ ($\bar{R}=6.6^{o}$).

corresponding to the displacement distributions in the relative directions of the pairs. Consequently, the distributions of Almansi strains E_{11}, $E_{22}-\overline{E}_{22}$ and E_{12} shown in Figure 4.15 (e-g) and Figure 4.16 (e-g) and rotations $R-\overline{R}$ (Figure 4.15 (h) and Figure 4.16 (h)) were obtained by using the moiré fringes of atomic lattices, where $\overline{E}_{22}=-0.033,\ -0.045$ and $\overline{R}=6.5°,\ 6.6°$ in the experiments presented in Figure 4.15 and Figure 4.16 respectively. In these two independent measurements, binarized Almansi strain distributions of E_{22} implying crinkle slope jumps across the ridges were also observed. Using Equation (4.10), the distributions of Almansi strain E_{22} were directly converted to the slope profiles of the mosaic blocks. From the slope distributions of the crinkle structures of HOPG grade III from the three measurements presented above shown in Figure 4.17, it is clear that the technique of DT-AFMI utilizing atomic lattices as reference gratings has good reproducibility in atomic strain measurements.

Other than the experimental reproducibility of DT-AFMI, the strain resolution as a function of window size is discussed in the following contents. How DT-AFMI measurements with fine strain resolution in a small measurement window enables us to study atomic-scale deformation, such as a slope jump of a fraction of a degree across a crinkle ridge, in unprecedented detail has been shown above. The study of crinkles in HOPG has revealed that an atomically layered structure like HOPG can focus surface curvature on the atomic scale, with a crinkle kink of a few degrees. Figure 4.18 shows the strain resolution, δE, of DT-AFMI for ALI as a function of window size x,

$$\delta E=\frac{\delta u}{\left(x-\delta x\right)} \tag{4.11}$$

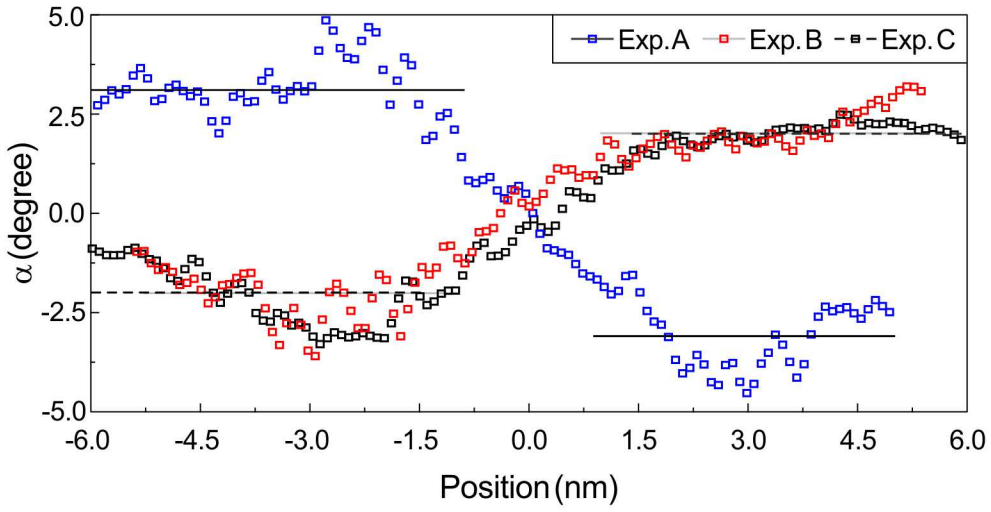

Figure 4.17 The slope-angle distributions across crinkle-ridge structures of HOPG grade III from DT-AFMI experiments.

where δu is the displacement resolution and δx denotes the fringe-location uncertainty respectively. Current resolutions of ALI denoted as the circle in blue solid line in the Figure 4.18 could be further refined by recording only fringe-image, not lattice-image scans of DT-AFMI in two different directions in a wide-field window. The resolution limit of digital image correlation (DIC) in a red dashed line is drawn for comparison (Espinosa *et al.*, 2011).

Similar to other historical interferometers (Michelson & Morley, 1887; Zehnder, 1891; Mach, 1892; Gabor, 1948; Kim *et al.*, 1977; Hÿtch *et al.*, 2008), DT-AFMI will enable us to probe unexplored physical phenomena involving localized atomic-scale deformation. In particular, DT-AFMI with its diverse selectivity of reference-lattice sizes has extensive applicability in nano and micro metrology. In turn, it will be useful in studying hierarchical physical processes at broad length scales. As an example, we have

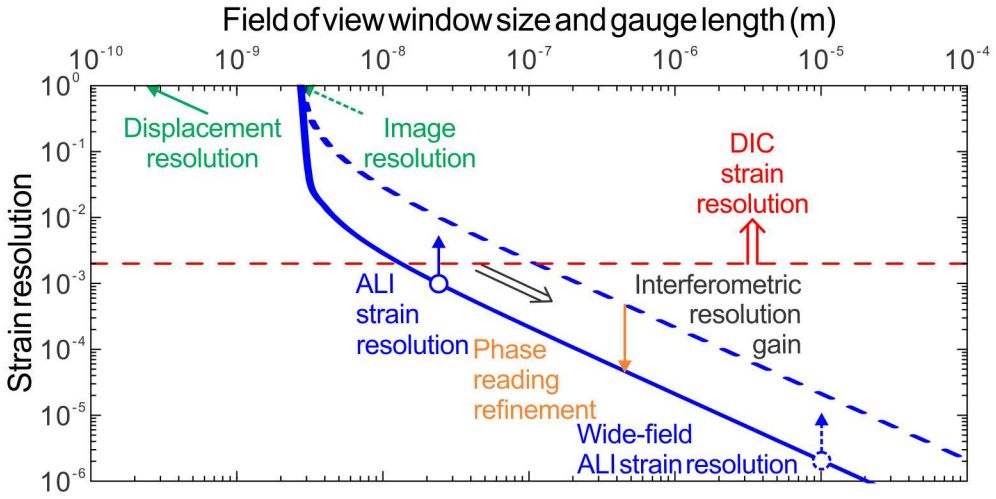

Figure 4.18 The strain resolution of ALI is represented by the circle in solid line. Dashed curves indicate the intrinsic strain resolutions of ALI as functions of the gauging window size. The solid curves correspond to the strain resolutions improved by an order (orange arrow) with phase-reading refinement. Further resolution enhancement can be achieved by recording only fringe intensities of DT-AFMI in a wide-field window (black double arrows). The resolution limit of digital image correlation in a red dashed line is for comparison.

successfully measured the atomic-scale strain field of a crinkle in HOPG, showing that the crinkle ridge has a highly concentrated surface curvature which could often provide sites of molecular adsorption, especially when electrically biased (Cullen & Lowe, 1994; Oliveira Brett & Chiorcea, 2003; Jay *et al.*, 2007).

Chapter 5. Conclusions and Future Directions

Nanocrystalline materials exhibit significantly different mechanical properties compared with their counterparts of coarse grains. There is fairly general agreement that mechanical strength and toughness of nanocrystalline materials are structurally characterized by large volume fraction of grain boundaries. Intrinsic relationship between nanometer scale mechanical characteristics of grain boundaries and macroscopic failure behavior of materials is the central idea in defining the nanocrystalline material strength. Such nanoscale materials are highly nonlinear and thus have different energy profiles in different atomic configurations. Therefore, the failure of grain boundaries under mechanical loading is highly cooperative and process-dependent at nanometer scales. For the deformation of grain boundary layers, the correlation length of symmetry breaking in atomic configurations and bifurcation instabilities in failure processes cannot be simply identified by classical Griffith cleavage energy or local properties of grain boundaries such as the misfit size of impurities and the bond strength variations.

To ascertain the strength and toughness of grain boundaries at the nanometer scale, which depend on cooperative separation processes, accurate and quantitative assessments of the grain boundary field descriptions with atomic features are required. In this study, the interior and exterior field projection methods of the grain boundary are developed through an inside-out approach for computation and an outside-in approach for

experiment respectively to establish connections between global loadings to nanoscale traction distributions of grain boundaries. The grain boundary field projection methods were used to access the projected cohesive tractions of Cu grain boundaries which show periodic concentrated compression and tension sites along the grain boundaries. The first point to notice is that at early stages of loadings, symmetric atomic rearrangement reduces the concentrated compression due to the ease of atomic incompatibility between the adjacent grains. At later stages of loadings, asymmetric atomic rearrangement or dislocation emission from the grain boundaries take place and decrease the concentrated tension because of the regularization of the incompatibility leading grain boundary opening. In addition, such asymmetric atomic rearrangement and dislocation emission, which could reduce the concentrated tension of grain boundary normal traction fluctuations, trigger the shear traction fluctuations along the grain boundaries. This transformation of grain boundary traction fluctuations opens an access to the new strain energy reservoir and thus enhances the separation toughness of the grain boundaries. For the presence of impurities of large atomic volume at the grain boundaries, theses dopants suppress the emission of asymmetric dislocation from the grain boundaries and therefore maintain the tension peaks of grain boundary normal traction fluctuations. Hence, the doped grain boundaries are retarded to have such transformation from normal to shear traction fluctuations and thus become brittle.

In this thesis, the development of a new experimental technique was motivated by EFP to provide the essential information of atomic deformation for exploring unclear characteristics of nanomaterials, such as localized atomic-scale deformation associated with molecular binding, dislocation or phase boundary motion, or surface pattern

formation. These minute atomic strains are expected as a signature of solid properties at small length scales (Jorio & Dresselhaus, 2007; Hÿtch *et al.*, 2008; Xue *et al.*, 2011). We therefore invent an AFM-based off-axis interferometer − DT-AFMI, which can measure surface strains in diverse samples under ambient conditions (i.e., room temperature and atmospheric pressure), and can make use of different reference lattices for variable resolution/window-sizes. An atomic lattice was employed as the reference lattice of DT-AFMI for the measurement technique − ALI, which can give us sub-angstrom scale resolution. The corresponding calibration experiments were implemented on HOPG specimen, and the atomic-scale strain fields of a crinkle structure in HOPG were successfully measured. The measurement results show that the crinkle ridge line has a highly concentrated surface curvature involving localized atomic-scale deformations. With the help of simulation-assisted data analyses, the experimental data reveal that the typical width, the kink angle and the minimum radius of the ridge as 1.76 nm, 6.2° and 8.51 nm, respectively.

In summary, the study in this thesis develops novel scientific computational projection methods and experimental metrology instrument for investigating unexplored physical phenomena of materials associated with minute and localized atomic deformation at nanometer scales. We believe that this is an important step towards establishing nanomechanics of materials and brings in several new directions in this new field of computational and experimental study. For the grain boundary separation toughness, the fracture direction dependent toughness in cooperative failure processes of grain boundaries is not clear yet. This question could be answered through analyses of grain boundary separation processes under various strain gradients, with the grain

boundary field projection method to see the variation of grain boundary traction transformation for different fracture directions along the grain boundaries. Furthermore, the grain-size dependent toughness of grain boundaries at nanometer scales is still unclear. A systematic molecular dynamics calculation could be helpful for examining this issue. However, molecular dynamics simulations for large scale problems are not feasible due to limitations in computational capacity. To solve these problems, we suggest that finite element analysis with proper boundary conditions of the elastic fields embracing the atomistic characteristics provided by the grain boundary field projection method could handle these large scale problems without much computation cost. Similarly, through finite element formulation which utilizes grain-boundary cohesive-zone elements, deformation analyses of polycrystalline materials at macroscopic scales can be achieved. For the measurement of atomic-scale deformation, nanostructural properties involving atomic distortions are still elusive in experimental study. Here, to resolve this problem, we propose the atomic lattice interferometry, which has the capability of measuring interesting properties of nanostructures with high strain resolutions in a small window of observation. Therefore, the deformation measurement of grain boundaries with this newly invented instrument should be thoroughly carried out for validating the computational analyses and theoretical predictions of grain boundary characteristics.

References

Barber, J.R. & Sturla, F.A. (1992). Application of the Reciprocal Theorem to Some Problems for the Elastic Half-Space. J. Mech. Phys. Solids, 40(1), 17–25.

Beltz, G.E. & Rice, J.R. (1991). Dislocation Nucleation versus Cleavage Decohesion at Crack Tips. Modeling the Deformation of Crystalline Solids: Physical Theory, Application, and Experimental Comparisons (ed. Lowe, T.C., Rollett, A.D., Follansree, P.S. & Daehn, G.S.), TMS Minerals, Metals and Materials Society, Warrendale, PA, 457-480.

Bertsekas, D.P. (1982). Constrained Optimization and Lagrange Multiplier Methods. Academic Press, New York.

Binnig, G., Quate, C.F. & Gerber, Ch. (1986). Atomic Force Microscope. Phys. Rev. Lett., 56, 930-933.

Binnig, G., Rohrer, H., Gerber, Ch. & Weibel, E. (1982). Surface Studies by Scanning Tunneling Microscopy. Phys. Rev. Lett., 49, 57-61.

Bonnet, M. & Constantinescu, A. (2005). Inverse Problems in Elasticity. Inverse Prob. 21(2), R1-R50.

Brenner, D.W., Shenderova, O.A., Harrison, J.A., Stuart, S.J., Ni, B. & Sinnott, S.B. (2002). A Second-Generation Reactive Empirical Bond Order (REBO) Potential Energy Expression for Hydrocarbons. J. Phys. Condens. Matter, 14, 783-802.

Budiansky, B. & Rice, J.R. (1973). Conservation Laws and Energy-Release Rates. J. Appl. Mech. Trans. ASME, 40, 201-203.

Chen, F.H.K. & Shield, R.T. (1977). Conservation Laws in Elasticity of the J-Integral Type. ZAMP, 28(1), 1-22.

Chen, H.-P., Kalia, R.K., Kaxiras, E., Lu, G., Nakano, A., Nomura, K-I., Van Duin, A.C.T., Vashishta, P. & Yuan, Z. (2010). Embrittlement of Metal by Solute Segregation-Induced Amorphization. Phys. Rev. Lett., 104, 155502.

Cheng, Y., Jin, Z.-H., Zhang, Y.W. & Gao, H. (2010). On Intrinsic Brittleness and Ductility of Intergranular Fracture along Symmetrical Tilt Grain Boundaries in Copper. Acta Mater., 58, 2293-2299.

Chew, H.B. (2013). Inverse Extraction of Interfacial Tractions from Elastic and Elasto-Plastic Far-Fields by Nonlinear Field Projection. J. Mech. Phys. Solids, 61(1), 131-144.

Choi, H.C., Schwartzman, A.F. & Kim, K.-S. (1992). Experimental Deformation Mechanics of Materials from Their Near-Atomic-Resolution Defect Images. Mater. Res. Soc. Symp. Proc., 239, 419-424.

Choi, S.T. & Kim, K.-S. (2007). Nano-Scale Planar Field Projection of Atomic Decohesion and Slip in Crystalline Solids. Part I: A Crack-Tip Cohesive Zone. Philos. Mag., 87(12), 1889-1919.

Chokshi, A.H., Rosen, A., Karch, J. & Gleiter, H. (1989). On the Validity of the Hall-Petch Relationship in Nanocrystalline Materials. Scr. Metall., 23, 1679-1684.

Clausius, R. (1870). On a Mechanical Theorem Applicable to Heat. Philos. Mag., 40(265), 122-127.

Cullen, D.C. & Lowe, C.R. (1994). AFM Studies of Protein Adsorption: 1. Time-Resolved Protein Adsorption to Highly Oriented Pyrolytic Graphite. J. Colloid Interface Sci., 166, 102-108.

Daw, M.S. & Baskes, M.I. (1984). Embedded-Atom Method: Derivation and Application to Impurities, Surfaces, and Other Defects in Metals. Phys. Rev. B, 29(12), 6443-6453.

Donald, A.M. & Brown, L.M. (1979). Grain Boundary Faceting in Cu-Bi Alloys. Acta Metall., 27, 59-66.

Duscher, G., Chisholm, M.F., Alber, U. & Ruhle, M. (2004). Bismuth-Induced Embrittlement of Copper Grain Boundaries. Nat. Mater., 3, 621-626.

Eckert, R., Laird, C. & Bassani, J.L. (1987). Fracture Mechanisms in Cu-O and Cu-Pb Alloys Fatigued with a Positive Mean Stress. Mater. Sci. Eng., 91, 19-28.

Espinosa, H.D., Juster, A.L., Latourte, F.J., Loh, O.Y., Gregoire, D. & Zavattieri, P.D. (2011). Tablet-Level Origin of Toughening in Abalone Shells and Translation to Synthetic Composite Materials. Nat. Commun., 2, 173.

Foucault, L.M. (1859). Mémoiresur la construction des télescopes en verreargenté. Annls. Obs. Paris, 5, 197-237.

Gabor, D. (1948). A New Microscopic Principle. Nature, 161, 777-778.

Gao, Y.F. & Bower, A.F. (2004). A Simple Technique for Avoiding Convergence Problems in Finite Element Simulations of Crack Nucleation and Growth on Cohesive Interfaces. Modell. Simul. Mater. Sci. Eng., 12(3), 453-463.

Gibbs, J.W. (1898). Fourier's Series. Nature, 59, 200.

Goodwin, L., Needs, R.J. & Heine, V. (1988). Effect of Impurity Bonding on Grain-Boundary Embrittlement. Phys. Rev. Lett., 60(20), 2050-2053.

Gott, V.L., Alejo, D.E. & Cameron, D.E. (2003). Mechanical Heart Valves: 50 Years of Evolution. Ann. Thorac. Surg., 76, S2230-S2239.

Hall, E.O. (1951). The Deformation and Ageing of Mild Steel: III Discussion of Results. Proc. Phys. Soc. London, Sect. B, 64, 747-753.

Hampe, W. (1874). Beiträge zu der Metallurgie des Kupfers. Berg-. Hütten- u. Salinenwesen, 23, 93-137.

Haydock, R. (1981). The Mobility of Bonds at Metal Surfaces. J. Phys. C: Solid State Phys., 14, 3807-3816.

Hong, S., Chew, H.B. & Kim, K.-S. (2009). Cohesive Zone Laws for Void Growth – I. Experimental Field Projection of Crack-Tip Crazing in Glassy Polymers. J. Mech. Phys. Solids, 57, 1357-1373.

Hong, S. & Kim, K.-S. (2003). Extraction of Cohesive Zone Laws from Elastic Far Fields of a Cohesive Crack Tip: A Field Projection Method. J. Mech. Phys. Solids, 51, 1267-1286.

Hÿtch, M., Houdellier, F., Hüe, F. & Snoeck, E. (2008). Nanoscale Holographic Interferometry for Strain Measurements in Electronic Devices. Nature, 453, 1086-1089.

Hÿtch, M.J., Putaux, J.-L. & Thibault, J. (2006). Stress and Strain around Grain-Boundary Dislocations Measured by High-Resolution Electron Microscopy. Philos. Mag., 86, 4641-4656.

Hÿtch, M.J., Snoeck, E. & Kilaas, R. (1998). Quantitative Measurement of Displacement and Strain Fields from HREM Micrographs. Ultramicroscopy, 74, 131-146.

Jay, G.D., Torres, J.R., Rhee, D.K., Helminen, H.J., Hytinnen, M.M., Cha, C.-J., Elsaid, K., Kim, K.-S., Cui, Y. & Warman, M.L. (2007). Association between Friction and Wear in Diarthrodial Joints Lacking Lubricin. Arthritis Rheum., 56(11), 3662-3669.

Jorio, A. & Dresselhaus, M.S. (2007). Nanometrology Links State-of-the-Art Academic Research and Ultimate Industry Needs for Technological Innovation. MRS Bull., 32, 988-993.

Kan, X.B., Misenheimer, M.E., Forster, K. & Moss, S.C. (1987). X-ray Study of Planar Defects in Highly Oriented Pyrolytic Graphite (HOPG). Acta Crystallogr. Sect. A, A43, 418-425.

Kim, H.-G., Chew, H.B. & Kim, K.-S. (2012). Inverse Extraction of Cohesive Zone Laws by Field Projection Method using Numerical Auxiliary Fields. Int. J. Numer. Methods Eng., 91(5), 516-530.

Kim, K.-S., Clifton, R.J. & Kumar, P. (1977). A Combined Normal- and Transverse-Displacement Interferometer with An Application to Impact of Y-cut Quartz. J. Appl. Phys., 48, 4132-4139.

Knowles, J.K. & Sternberg, E. (1972). On a Class of Conservation Laws in Linearized and Finite Elastostatics. Arch. Ration. Mech. Anal., 44(3), 187-211.

Kumar, K.S., Suresh, S., Chisholm, M.F., Horton, J.A. & Wang, P. (2003a). Deformation of Electrodeposited Nanocrystalline Nickel. Acta Mater., 51, 387-405.

Kumar, K.S., Van Swygenhoven, H. & Suresh, S. (2003b). Mechanical Behavior of Nanocrystalline Metals and Alloys. Acta Mater., 51, 5743-5774.

Laporte, V. & Mortensen, A. (2009). Intermediate Temperature Embrittlement of Copper Alloys. Int. Mater. Rev., 54(2), 94-116.

Li, G.H. & Zhang, L.D. (1995). Relationship between Misorientation and Bismuth Induced Embrittlement of [001] Tilt Boundary in Copper Bicrystal. Scr. Metall. Mater., 32, 1335-1340.

Li, Q. & Kim, K.-S. (2009). Micromechanics of Rough Surface Adhesion: A Homogenized Projection Method. Acta Mech. Solida Sin., 22, 377-390.

Li, X., Wei, Y., Lu, L., Lu, K. & Gao, H. (2010). Dislocation Nucleation Governed Softening and Maximum Strength in Nano-Twinned Metals. Nature, 464, 877-880.

Liu, Z., Gong, Y., Zhou, W., Ma, L., Yu, J., Idrobo, J.C., Jung, J., MacDonald, A.H., Vajtai, R., Lou, J. & Ajayan, P.M. (2013). Ultrathin High-Temperature Oxidation-Resistant Coatings of Hexagonal Boron Nitride. Nat. Commun., 4, 2541.

Lozovoi, A.Y., Paxton, A. T. & Finnis, M.W. (2006). Structural and Chemical Embrittlement of Grain Boundaries by Impurities: A General Theory and First-Principles Calculations for Copper. Phys. Rev. B, 74, 155416.

Lu, G., Kioussis, N., Bulatov, V.V. & Kaxiras, E. (2000). Generalized-Stacking-Fault Energy Surface and Dislocation Properties of Aluminum. Phys. Rev. B, 62(5), 3099-3108.

Lu, K., Lu, L. & Suresh, S. (2009). Strengthening Materials by Engineering Coherent Internal Boundaries at the Nanoscale. Science, 324, 349-352.

Mach, L. (1892). Über einen Interferenzrefraktor. Zeitschrift für Instrumentenkunde, 12, 89-93.

Messmer, R.P. & Briant, C.L. (1982). The Role of Chemical Bonding in Grain Boundary Embrittlement. Acta Metall., 30, 457-467.

Michelson, A.A. & Morley, E.W. (1887). On the Relative Motion of the Earth and the Luminiferous Ether. Am. J. Sci., 34, 333-345.

Mohn, F., Gross, L., Moll, N. & Meyer, G. (2012). Imaging the Charge Distribution within A Single Molecule. Nat. Nanotechnol., 7, 227-231.

Novoselov, K.S., Geim, A.K., Morozov, S.V., Jiang, D., Zhang, Y., Dubonos, S.V., Grigorieva, I.V. & Firsov, A.A. (2004). Electric Field Effect in Atomically Thin Carbon Films. Science, 22, 666-669.

Ohler, M., Baruchel, J. & Galez, P. (1995). An X-ray Diffraction Topographic Study of Highly Oriented Pyrolytic Graphite. J. Phys. D: Appl. Phys., 28, A78−A83.

Oliveira Brett, A.M. & Chiorcea, A.-M. (2003). Atomic Force Microscopy of DNA Immobilized onto A Highly Oriented Pyrolytic Graphite Electrode Surface. Langmuir, 19, 3830-3839.

Petch, N.J. (1953). The Cleavage Strength of Polycrystals. J. Iron Steel Inst., 174, 25-28.

Pipkin, A.C. (1986). Some Examples of Crinkles. IMA Volumes in Math.Appl., 1, 182-195.

Plimpton, S.J. (1995). Fast Parallel Algorithms for Short-Range Molecular Dynamics. J. Comput. Phys., 117, 1-19.

Raman, C.V. & Datta, S.K. (1925). On Brewster's Bands. Part I. Trans. Opt. Soc. London, 27(7), 51-55.

Rayleigh, Lord (Strutt, J.W.) (1874). On the Manufacture and Theory of Diffraction Gratings. Philos. Mag., 47, 193-205.

Rice, J.R. (1968). A Path Independent Integral and the Approximate Analysis of Strain Concentration by Notches and Cracks. J. Appl. Mech. Trans. ASME, 35, 379-386.

Rice, J.R. & Wang, J.-S. (1989). Embrittlement of Interfaces by Solute Segregation. Mater. Sci. Eng. A, 107, 23-40.

Righi, A. (1887). Sui fenomeni che si producono colla sovrapposizione di due peticoli e sopra alcune loro applicazioni. Il Nuovo Cim. Ser. 3, 21(1), 203-228.

Ronchi, V. (1925). La prova dei sistemi ottici. Attual. Scient., 37, Chapt. 9.

Sadewasser, S., Carl, P., Glatzel, T. & Lux-Steiner, M.C. (2004). Influence of Uncompensated Electrostatic Force on Height Measurements in Non-Contact Atomic Force Microscopy. Nanotechnol., 15, S14-S18.

Sahin, O., Magonov, S., Su, C., Quate, C.F. & Solgaard, O. (2007). An Atomic Force Microscope Tip Designed to Measure Time-Varying Nanomechanical Forces. Nat. Nanotechnol., 2, 507-514.

Schiøtz, J., Di Tolla, F.D & Jacobsen, K.W. (1998). Softening of Nanocrystalline Metals at Very Small Grain Sizes. Nature, 391, 561-563.

Schweinfest, R., Paxton, A.T. & Finnis, M.W. (2004). Bismuth Embrittlement of Copper is An Atomic Size Effect. Nature, 432, 1008-1011.

Shield, T.W. & Kim, K.-S. (1991). Diffraction Theory of Optical Interference Moiré and A Device for Production of Variable Virtual Reference Gratings: A Moiré Microscope. Exp. Mech., 31, 126-134.

Sigle, W., Chang, L.-S. & Gust, W. (2002). On the Correlation between Grain-Boundary Segregation, Faceting and Embrittlement in Bi-Doped Cu. Philos. Mag. A, 82, 1595-1608.

Sutton, A.P. & Vitek, V. (1982). An Atomistic Study of Tilt Grain Boundaries with Substitutional Impurities. Acta Metall., 30, 2011-2033.

Theocaris, P.S. (1969). Moiré Fringes in Strain Analysis. Pergamon Press, London, Chapt. 2.

Tolenaar, D. (1945). Moiré Interferentieverschijnselen Bij Rasterdruck. Institutvoor Graphische Technik, Amsterdam.

Van der Giessen, E. & Needleman, A. (1995). Discrete dislocation plasticity: a simple planar model. Modell. Simul. Mater. Sci. Eng., 3(5), 689-735.

Van Swygenhoven, H., Derlet, P.M. & Hasnaoui, A. (2002). Atomic Mechanism for Dislocation Emission from Nanosized Grain Boundaries. Phys. Rev. B, 66, 024101.

Wang, C.-K., Chew, H.B. & Kim, K.-S. (2011). Nanometer Scale Mechanical Behavior of Grain Boundaries. Mater. Res. Soc. Symp. Proc., 1297, 1-9.

Weertman, J.R., Farkas, D., Hemker, K., Kung, H., Mayo, M., Mitra, R. & Van Swygenhoven, H. (1999). Structure and Mechanical Behavior of Bulk Nanocrystalline Materials. MRS Bull., 24, 44-50.

Willis, J.R. (1966). Hertzian Contact of Anisotropic Bodies. J. Mech. Phys. Solids, 14(3), 163-176.

Xue, J., Sanchez-Yamagishi, J., Bulmash, D., Jacquod, P., Deshpande, A., Watanabe, K., Taniguchi, T., Jarillo-Herrero, P. & LeRoy, B.J. (2011). Scanning Tunnelling Microscopy and Spectroscopy of Ultra-Flat Graphene on Hexagonal Boron Nitride. Nat. Mater., 10, 282-285.

Yin, J. (1998). Observation on Emitting Dislocation from Grain Boundary by TEM. J. Mater. Sci. Technol., 14, 75-76.

Young, T. (1804). Bakerian Lecture: Experiments and Calculations Relative to Physical Optics. Philos. T. R. Soc. Lond., 94, 1−16.

Zehnder, L. (1891). EinneuerInterferenzrefraktor. Zeitschrift für Instrumentenkunde, 11, 275-285.